Passive and Active Component Design and Analysis for Millimeter Wave Front Ends

by

Shane A. Verploegh

B.S., University of Notre Dame, 2014

M.S., University of Colorado Boulder, 2018

A thesis submitted to the

Faculty of the Graduate School of the

University of Colorado in partial fulfillment

of the requirements for the degree of

Doctor of Philosophy

Department of Electrical Computer and Energy Engineering

2021

Committee Members:

Zoya Popovic, Chair

Prof. Gregor Lasser

Prof. Dejan Filipovic

Prof. Taylor Barton

Dr. Michael Roberg

Dr. Erich Grossman

Verploegh, Shane A. (Ph.D., Electromagnetics)

Passive and Active Component Design and Analysis for Millimeter Wave Front Ends

Thesis directed by Prof. Zoya Popovic

Growing applications at millimeter-wave frequencies up to the 75-110 GHz W-band require sufficient power levels generated from solid state devices in order to achieve enough range in communication and radar systems. In this thesis, an advanced 40-nm gate Gallium Nitride (GaN) on Silicon Carbide (SiC) integrated circuit process was used to design multi-stage and power-combined power amplifiers that can achieve 0.5 W power levels across the entire WR-10 waveguide band. Two 3-stage reactively combined unit amplifiers are combined in a balanced topology and three such amplifiers in a serial cascaded topology. The fabricated MMICs are characterized in a small-signal and large-signal measurement setup and compared to simulations. A study of power-combining efficiencies at the device, staging, and circuit levels is performed and fabricated components show good agreement with theory. Additionally, due to large process variations across and between GaN wafers, a statistical analysis for W-band MMICs designed in an experimental 90-nm GaN-on-SiC process is introduced. This analysis starts from measured on-wafer S-parameters for about 80 power-combined amplifier chips. The demonstrated MMICs can be packaged and interfaced to rectangular waveguide for broadband and low-loss front-ends with good heat-sinking. An investigation of metal 3D-printing for fabrication of such waveguide components is presented, including a statistical analysis of the surface roughness for various materials and an analysis for feature resolution through complex internal features. Finally, the statistical analysis developed for the MMIC variations is extended to cascaded statistics of MMIC PAs, waveguide transitions, and a waveguide-fed antenna array for spatial output power-combining.

Dedication

To my youth, friends, climbing, skiing, and coffee.

To Jim and Diane, my parents.

To Blake Graham, my best friend.

...

Gratitude towards innumerable people, actions, and abstract concepts, often too difficult to condense in a penetrating manner, is hopefully captured with the above.

Acknowledgments

I am proud to have Prof. Zoya Popovic as my graduate advisor. She has been nothing but generous with her time and dedication and seemingly endless supply of energy. There are no thanks that would measure up to the opportunity and education that has been afforded me within her laboratory. I cannot imagine going through this graduate experience without her at the helm.

I would like to especially thank Prof. Gregor Lasser as he has been an invaluable role model and friend while in this program. Discussions with him have been only enlightening and delightful.

I am eternally grateful to my fellow graduate students and friends that have been alongside this path from the beginning: Philip Zurek, Mike Grayson, Aman Samaiyar, Guillermo Nevett, Jose Estrada, Eric Kwiatkowski, Kshitij Sadasivan, Eric Berry, Mauricio Pinto, Maxwell Duffy, Tim Sonnenberg, Megan Robinson, Akim Babenko, Prathamesh Pednekar, Kimon Vivien, Laila Marzall, Nina Basta-Popovic, Billy Raseman, Luke Prohaske, Allison Duh, Charlie Rackson, Polly Murray, Jan Bartos, Steve Guard, and Johnny Hergert. To the RF Coffee Club, the Lunch Bunch, the Ducking Clymbing crew, and the Meme Shop Bois: many thanks for killing hours of time and stress. And to those that helped physically and emotionally after my ACL tear and long recovery, specifically Phil, Mike, Aman, Guillermo, Becca Walsh, and Ryan Richardson, my sincerest thanks.

Particular thank yous to Dr. Scott Schafer for the code ecosytem that you left behind so I could make this thesis and the particularly gorgeous layout images contained within and to Dr. Maurico Pinto for beginning to setup the millimeter-wave infrastructure in the microwave lab so that I could progress it further.

Contents

List of Tables

List of Figures

Chapter 1

Introduction and Motivation

Contents

1.1 Millimeter-Wave Applications

The V-band, 50-75 gigahertz (GHz), and W-band, 75-110 GHz, is occupied with backhaul communication links for earth and space systems, millimeter-wave (mm-wave) imaging, spectroscopy, radioastronomy, and automotive radar. This frequency range is characterized by high-data throughput (from high bandwidth space), high imaging resolution (from small wavelengths), and penetrability through certain environmental conditions (e.g. atmospheric absorption windows and penetration through dust, smoke, and fog [1,2]). Fig. 1.1 shows frequency allocations in V- and W-band with applications ranging from space research to mobile communications.

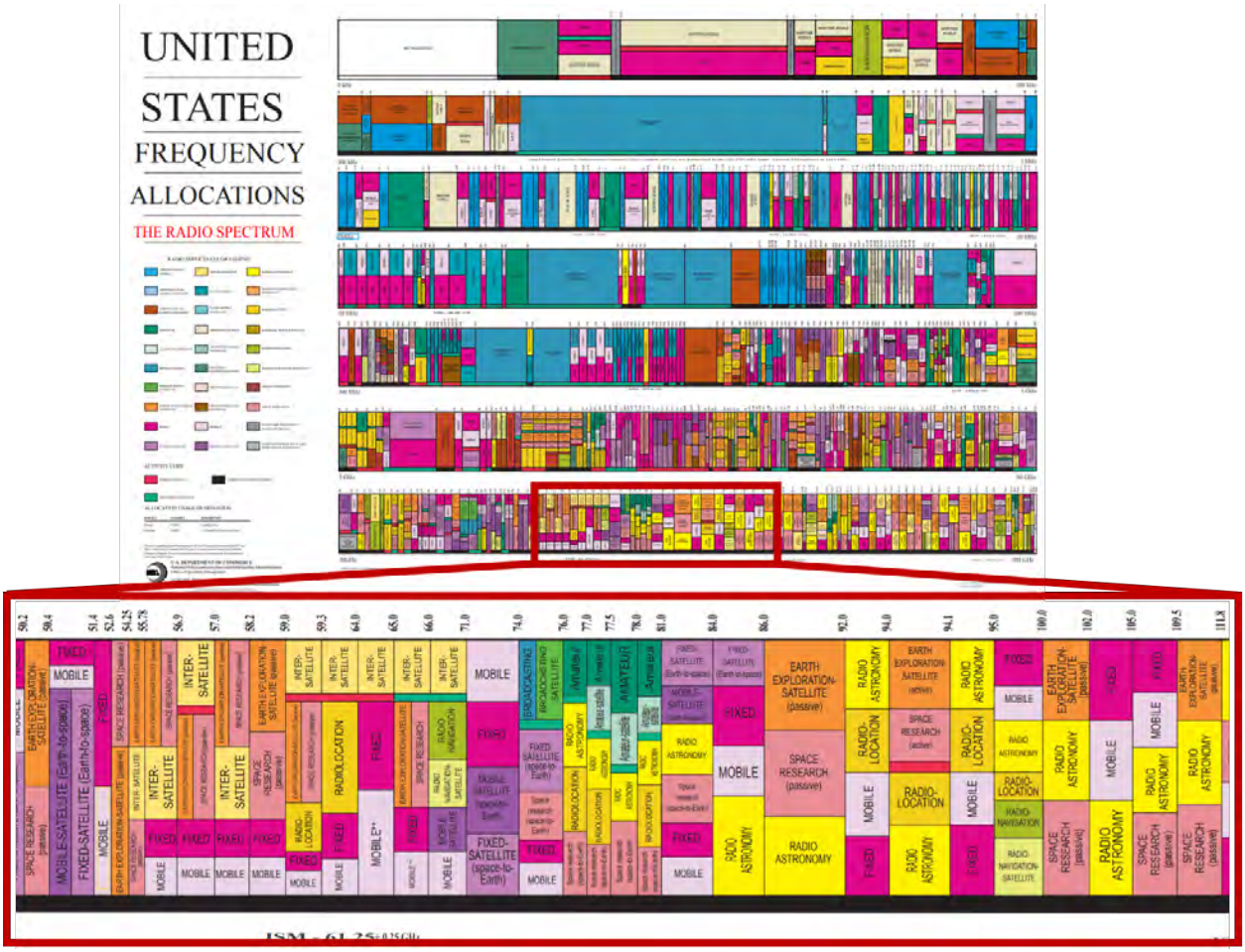

Figure 1.1: A detail of the 2016 United States Frequency Allocation chart for the V- and W-band sourced from [3]. The usage of the W-band is still being subdivided as new application ideas are proposed.

With growing user demand for extensive multimedia content with large storage and transfer needs, communication links are under development for current telecommunication systems in 5G lower mm-wave bands (roughly around 30 GHz). There is a desire to push to higher frequencies in the future such as the new 5G unlicensed allocations at V-band in the 57-64 GHz and 64-71 GHz bands [4, 5], the 60 GHz WiFi IEEE allocated bands [6], and the FCC allocations for private sector development of point-to-point links from 71-76, 81-86, and 92-95 GHz [7]. Demonstrated high data rate communication systems operating at 92 GHz and achieving 6.5 Gbps with quadrature ampli-

tude modulation (QAM)-128, are shown with GaN front-ends [8], and data rates up to 80 Gbps with 16-QAM signals are shown in a 6 m range at 75 GHz wireless link using 100-nm InGaAs mHEMT technology for the LNA and mixer [9]. Additionally, mm-wave communications are attractive for fixed satellite services and space exploration missions [10,11]. In already developed high throughput geostationary multimedia services at K-band, W-band carrier frequencies could reduce the number of pathways for data transmission allowing allocated resources to reroute during failures. In deep space, the high directivity of high-element number compact antenna arrays in W-band is of interest.

High resolution imaging with W-band phased array systems is accomplished as a result of the small wavelengths at mm-wave [12–14]. Developed imaging systems function as radars where the point scatterers can be resolved within 1-2 cm accuracy. Security screening for weapon detection has been shown at 30 GHz [15], 70 GHz [16], and 92 GHz [17]. Imaging and gesture detection has been shown commercially from a Google Soli device at 60 GHz [18, 19] and is being developed at 94 GHz [20]. Various radar platforms have been demonstrated such as a 3-D imaging 100-GHz multiple-input multiple-output (MIMO) frequency-modulated continuous-wave (FMCW) radar in [21], 93.5-94.5 GHz MIMO FMCW radar in [22], and a 94 GHz airborne synthetic aperature radar for urban site monitoring. Hidden object detection and identification has been demonstrated through walls and various materials in [23–25]. In automotive radar, the 76-77 GHz and the more recently added 77-81 GHz bands satistfy the imaging resolution and data speed requirements for automated driving [26]. Multiple low-power W-band phased arrays and estimation techniques using silicon technology were demonstrated for automotive radar [27–32].

There are a number of new applications under development for a W-band applications e.g. industrial vibrometry [33, 34]. Here, the small wavelength of the upper W-band allows for highly accurate readings of displacement versus time. In a similar vein, there has even been medical research using CW radar for measuring human respiration and heartbeat [35]. Other medical applications exist such as irradiating cancer cells with frequency sweeps covering the entire band [36]. Scientific fields that can benefit from W-band radar systems as well such as using radar to detect insect wing-beat frequency for observing insect migration without perturbation [37] and

classification of production faults in imperfect fabrication of materials [38].

The drawbacks of using the frequencies in the mm-wave bands is high attenuation due to the tropospheric events and atmospheric phenomena. Due to high propagation loss, these applications can benefit from higher transmitted power levels (>1 W); however, solid-state power amplifiers (PAs) are limited in total output power, bandwidth, and efficiency at mm-wave frequencies, requiring power combining and increased number of RF components in the analog front-end.

1.2 III-V Semiconductors and Devices for mm-wave Front Ends

High electron mobility transistors (HEMT) are nonlinear devices formed by a junction between materials with different band gaps and are attractive for RF design due to high-frequency performance and lower noise values than other transistor technology. HEMTs are commonly fabricated using III-V semiconductors, of which Gallium Arsenide (GaAs), Gallium Nitride (GaN), and Indium Phosphate (InP) are the currently common process technologies.

Figs. 1.2 and 1.3 show the overlapping spaces where measured RF performance for the III-V semiconductors has been shown. InP heterogenous electron mobility transistors (HEMTs) and InP heterojunction bipolar transistors (HBT) are more prevalent in terahertz (THz) ranges with GaAs HEMTs also showing low noise and comparable power output in the mm-wave ranges [39, 40]. The transition frequency and maximum frequency for GaN devices has been reported up to 454 f_t/444 f_{max} GHz with much higher breakdown in the mm-wave range than InP and GaAs. As such, GaN presents an opportunity for high output powers at mm-wave frequencies. This thesis presents research in wideband power-combined mm-wave PAs in GaN-on-SiC process technologies for this goal.

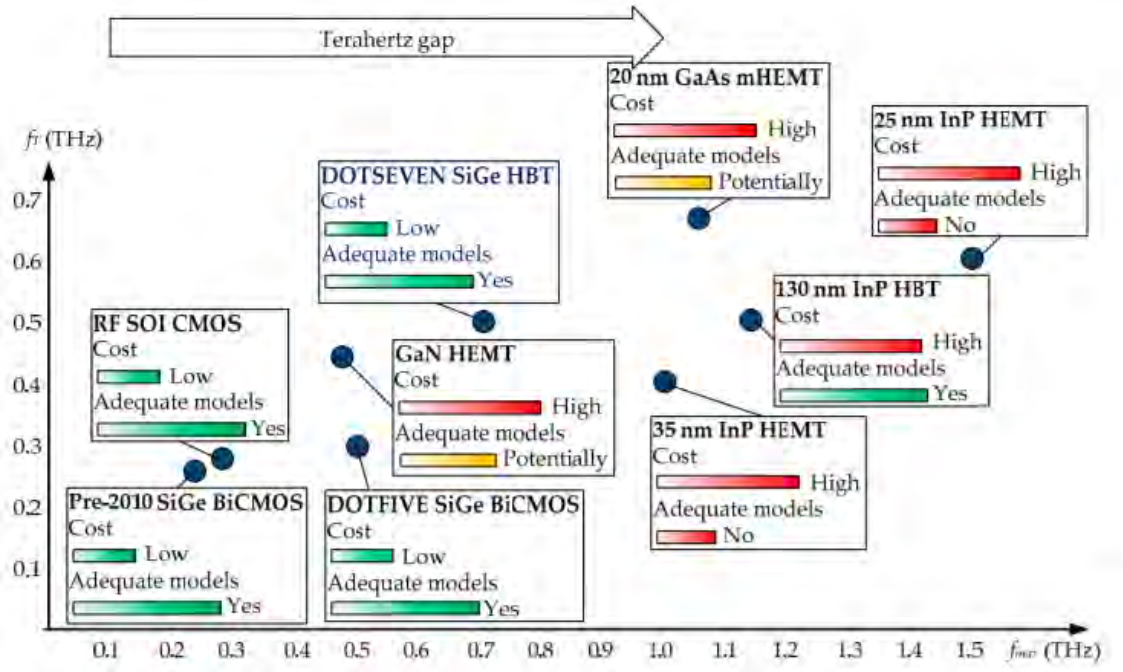

Figure 1.2: Semiconductor comparison for scaled processes of transition frequency over max frequency. Figure is reproduced from [39].

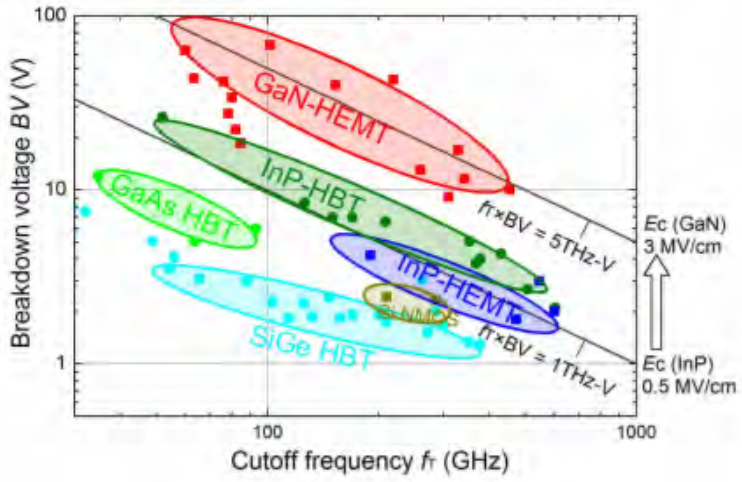

Figure 1.3: Semiconductor comparison for scaled processes of breakdown voltage over transition (cutoff) frequency. Figure is reproduced from [40].

Fig. 1.4a shows the layout of the HRL T3 40-nm gate GaN/AlGaN double HEMT [40]. The

motivation here is that the power of an individual transistor drops roughly as the square of frequency for a given process [41]. For increasing RF power output from a transistor, power-combining with multiple devices, increasing breakdown voltage, and increasing maximum drain current are obvious options. Power-combining at the device level is where more active channels are combined, in multi-fingered HEMTs as seen in Fig 1.4b, to increase the total periphery area and consequently the total power output. A higher breakdown voltage allows for an increase on drain voltage swing from the dc power supply, effectively increasing the RF output power. The saturated drain current is related to the device transconductance, g_m, which is proportional to the transition frequency and inversely proportional to gate-to-source capacitance. Increasing transition frequency through device scaling raises the total saturated drain current and raises the total output power.

In addition to the power dropping with frequency, the efficiency of transistors also scales. One of the reasons is that smaller gate lengths which correspond to small capacitance inherently have increased resistance. Therefore, for the same output power, the loss to heat increases decreasing the efficiency. Additional contributors to efficiency decrease at a circuit level include losses of matching networks and interconnects. For power amplifiers, waveform shaping through harmonic terminations is often used to increase efficiency. This implies that some harmonic content is available requiring that the transition frequency of the process is significantly above the operation frequency which is not the case for W-band technology.

Fig. 1.5 show the outcomes of device scaling to achieve high power output at mm-wave frequencies on a 90-nm and 40-nm gate length.

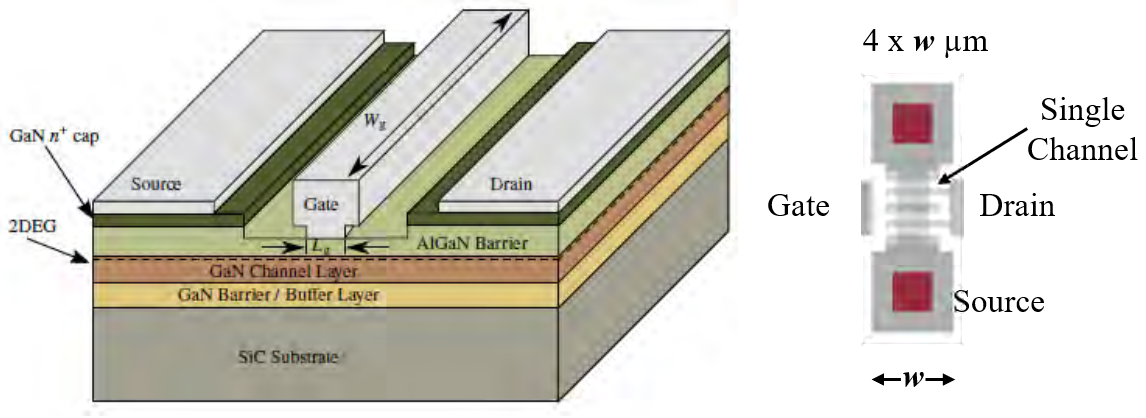

(a) (b)

Figure 1.4: Diagram of (a) a GaN/AlGaN HEMT using the HRL T3 process [42] and (b) a multi-channel HEMT in the same process.

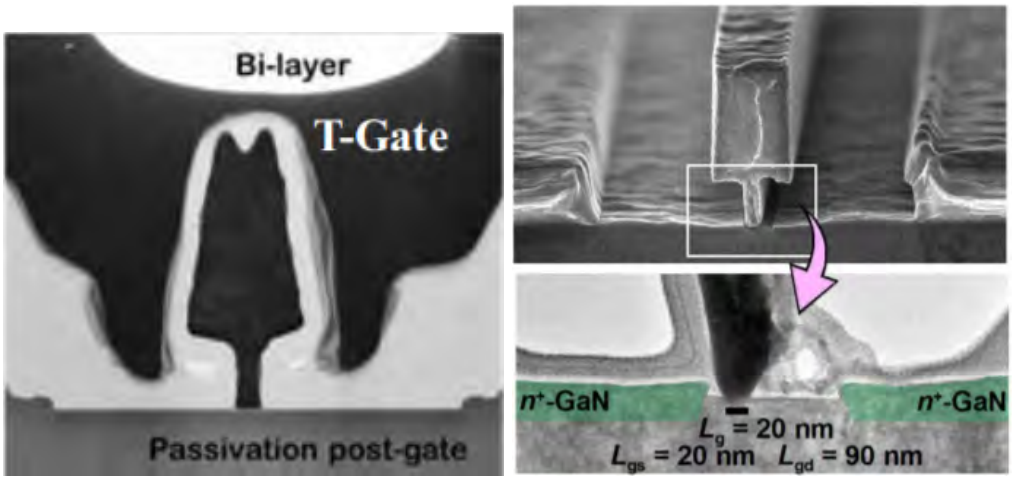

(a) (b)

Figure 1.5: Photographs gate cross-sections of (a) Qorvo 90-nm GaN HEMT sourced from [43] and (b) HRL T4 20-nm GaN HEMT sourced from [40].

The MMIC PA designs contained in this thesis are fabricated in the HRL T3 40-nm GaN-on-SiC HEMT process, documented well in [40, 44–52], and the Qorvo 90-nm GaN-on-SiC HEMT, documented well in [43, 53–55]. The goal of the designs presented in later chapters is to obtain high output powers in order to enable the various applications discussed above with its inherent

challenges.

1.3 Overarching mm-wave Challenges

Two of the main challenges for W-band spectrum usage are environmental conditions and the increasing system complexity and cost due to the small wavelength at mm-wave. With system-level integration, care must be taken for high-power output as well as variability in packaging and fabrication due to the tight tolerances needed.

Fig. 1.6 illustrates the various important features of the atmosphere relevant to mm-wave propogation.The troposphere is the first layer, 10 miles thick, of the Earth's atmosphere. This region contains most of the communication networks and other mm-wave usage while also where weather events and airborne molecules/gases are concentrated. An electromagnetic plane wave that propagates through this rapidly changing inhomogenous medium encounters frequency-dependent scattering and absorption; attenuating a transmitted signal. The sources of attenuation are identified to include rain/water vapor, clouds and gases, and tropospheric scintillation. The other layers of the atmosphere also affect millimeter-wave propagation, however, a majority of applications do not preclude transmission from space to earth or vice versa and these phenomena are not particularly well-studied above V-band.

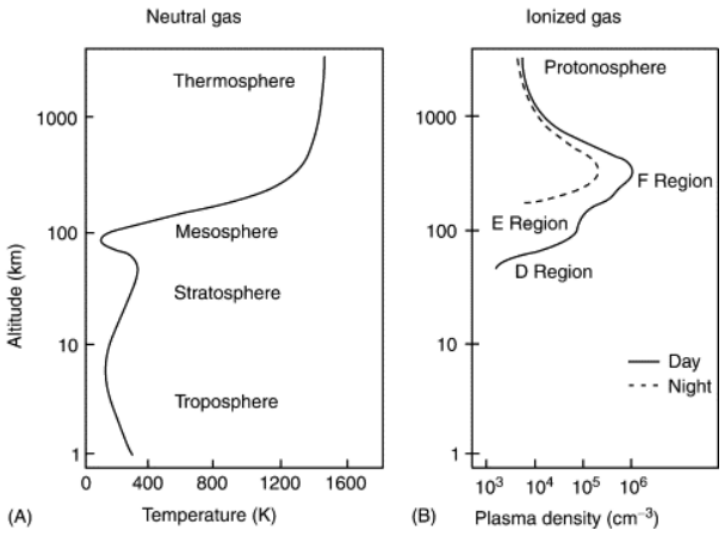

Figure 1.6: Diagrams of (a) atmospheric temperature and (b) ionosphere plasma density with various layers designated [56].

Fig. 1.7 shows the water vapor and oxygen attenuation over frequency. There are frequency 'windows' in these attenuation spikes where a large majority of the long distance communication uses lie. However, it is still clear that the relatively lower attenuation of these windows is much higher, such as 0.4 dB per km at 94 GHz, than lower frequencies such as in X-band where attenuation is less than 0.03 dB per km. Models of attenuation and delay rates due to fog/cloud conditions for mm-wave can be found within [57]. For interactions with other gases and airborne molecules, [58,59] are good resources.

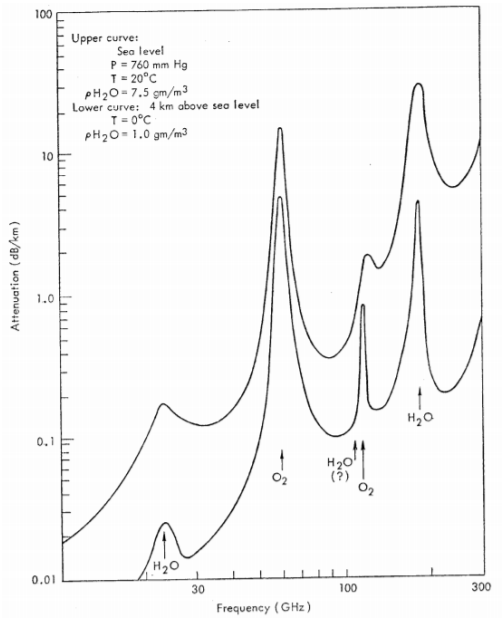

Figure 1.7: Horizontal attenuation due to oxygen and water vapor [60].

Attenuation in weather events, specifically rain, can change due to intensity of a storm [59]. Fig. 1.8 shows these varying levels of path loss due to rain rate. Storm forecasting prediction and the correlated value of rain rate to mm-wave attenuation is important for maintaining high-data rate communication in significant weather conditions. A comprehensive survey of attenuation prediction models is contained within [61].

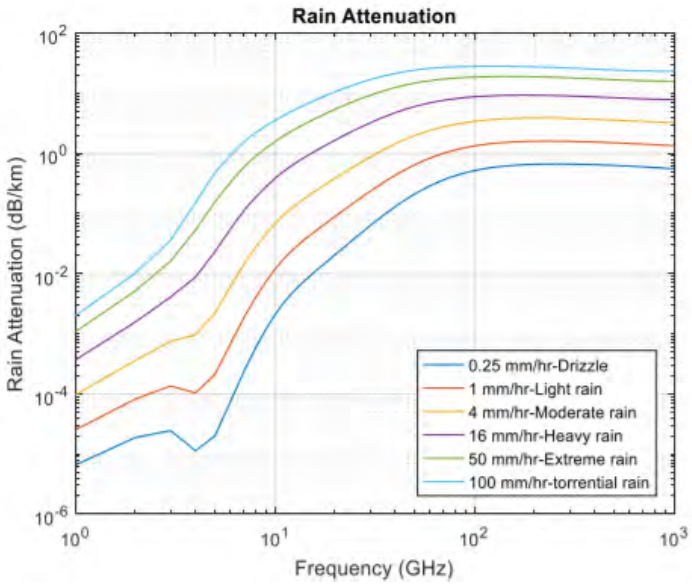

Figure 1.8: Attenuation over frequency due to varying rain intensity [62].

Less dominant phenomena such as scintillation and depolarization can also impact mm-wave systems significantly [10]. Scintillation is rapid fluctations of in signal amplitude and phase along the propagation path due small-scale non-homogenous refractive indexes from atmospheric turbulence and has been measured up to 58.5 GHz [63–65]. Depolarization occurs when the propagation path is through non-spherical particles, such as fast rain drops and ice crystals and also has been measured at 50 GHz [66]. Depolarization is when the polarization of propagating wave may change its state on interaction with matter.

This thesis aims to increase the power output and bandwidth of W-band transmitter front-ends. This allows the environmental path loss to be compensated as a fade mitigation technique for maintaining a high signal-to-noise ratio (SNR). Broadband operation is desired to cover multitudes of application space. However, solid-state power amplifiers are limited in total output power, bandwidth, and efficiency at mm-wave frequencies. This requires a balancing act between high number of elements for power-combining, tight spacing due to transmission loss and mm-wave design, and low performances of III-V semiconductors at mm-wave. For transmitters at lower frequencies, high power outputs from single devices can be split and routed through feed networks

to multiple antennas. However, with high losses at millimeter-wave frequencies in waveguides, transmission lines, and free-space, spatial power combining arrays with minimal power division are of interest to achieve transmitters with high effective isotropic radiated power (EIRP), e.g. [67]. This usually means sub-dividing a whole array into smaller sub-arrays to simplify construction and tightly integrate components. A full array is then comprised of a multitude of arranged sub-arrays. Fig. 1.9 shows two sub-array modules of large arrays and Fig. 1.10 shows complete systems where these sub-modules are combined.

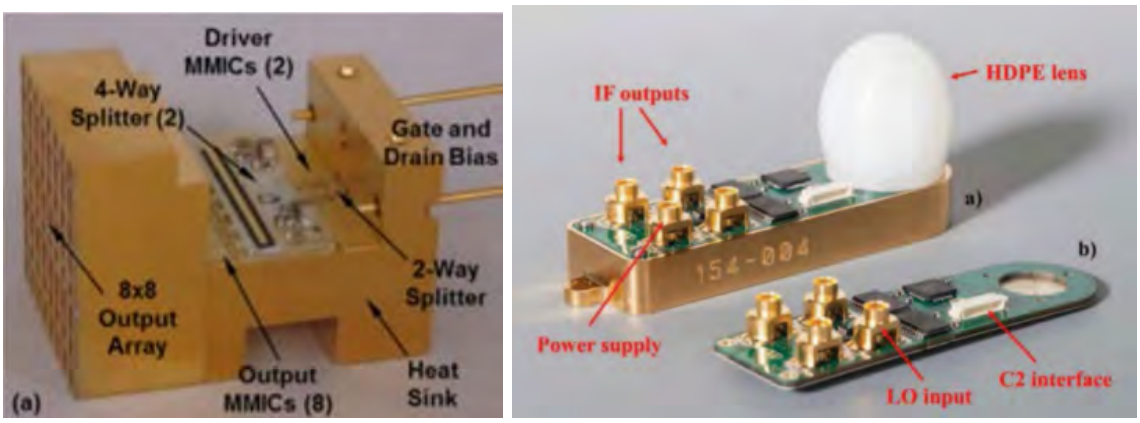

(a) (b)

Figure 1.9: Sub-module transmit/recieve photographs from (a) a 94 GHz 7 W GaN 8x8 output array [67] and (b) a 94 GHz GaAs single element lens [13, 68].

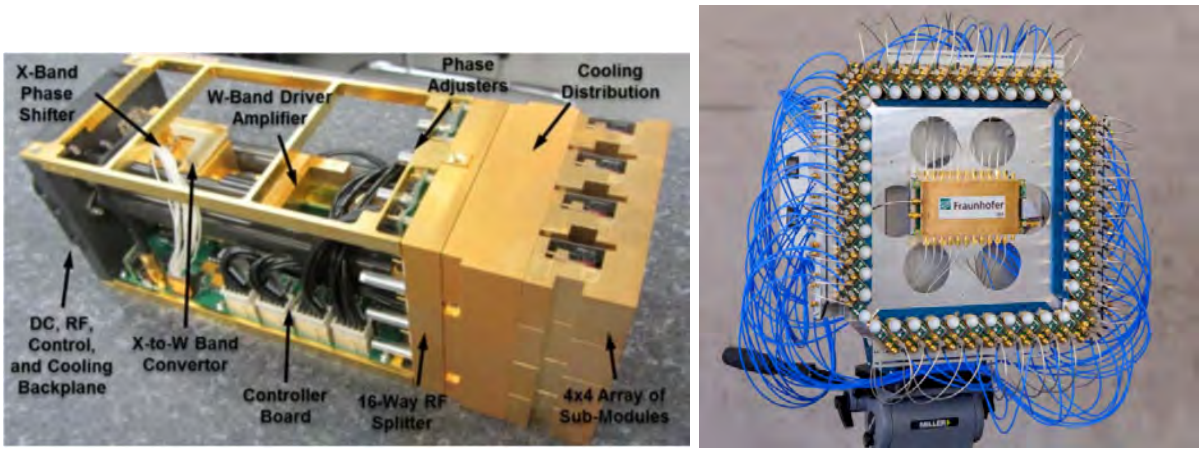

(a) (b)

Figure 1.10: Complex module transmit/recieve photographs from (a) a 94 GHz 100 W GaN 32x32 element output array [67] and (b) a 94 GHz GaAs 44 element MIMO imaging array [13].

In a front-end transmit array, routing, amplifying, and power-combining mm-wave energy is a complex design task. To reduce high losses internal to the system at mm-wave, tight integration becomes a necessity. With tight integration, high coupling requires careful full-wave electromagnetic simulations. Further, all designed components are highly sensitive in RF electrical performance to fabrication tolerances. For example, 1 degree of electrical length at 92.5 GHz in a 50 Ω microstrip line in 50 μm thick GaN-on-SiC is 3.5 μm. An additional challenge is the fact that transistors have high gain at the low frequencies, making these designs stable requires comprehensive stability analysis and network features.

1.4 Outline of Thesis

The work presented in this thesis aims to address system-level integration problems for wideband, high power W-band transmitters with detailed millimeter-wave power amplifier design in current state-of-the-art in GaN-on-SiC process and as well as novel packaging techniques and waveguide construction in 3D printed metal processes. Fig. 1.11 shows the flow of components that this thesis presents for broadband millimeter-wave operation.

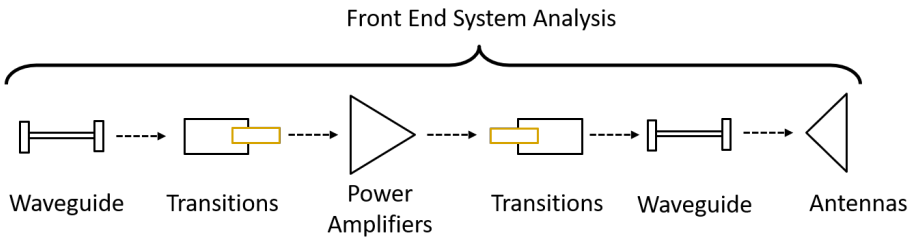

Figure 1.11: A diagram of the 'virtual' millimeter-wave broadband front-end that this thesis aims to cover from passive component design and analysis to power amplifier design and measurement to statistical system analysis.

The content of each of the chapters are as follows:

Chapter 2: presents designs of a number of passive 3D printed V- and W-band rectangular metal waveguides, such as straight sections, couplers, and splitters. As well, 3D printing methods useful for metal structures with fine geometrical features are described.

Chapter 3: presents small-signal measurements of the fabricated waveguide structures. An analysis of the surface roughness and feature resolution in respect to measured RF electrical performance is presented.

Chapter 4: describes W-band transistion designs from metal rectangular waveguide to planar MMICs.

Chapter 5: presents the details of the designs for two 3-stage W-band MMIC PAs in an HRL 40-nm GaN HEMT process. A description of W-band power amplifier measurement setups for small- and large-signal is presented.

Chapter 6: describes two W-band power-combining PA architectures using the two designs from Chapter 5 as 'Units'. An analysis of the effect of the amplitude and phase imbalances from the combining circuits is presented and compared to the measured RF performance of the MMIC PAs.

Chapter 7: presents a novel statistical analysis process flow of density estimation and sampling performed on a measured small-signal data-set from MMIC PAs made in a Qorvo 90-nm GaN HEMT process.

Chapter 8: generates and uses random variable sets from the density estimates found in statistical analysis in Chapter 7 to present an analysis of the effects of cascading S-parameters from mm-wave networks on spatial power combining.

Chapter 9: summarizes the thesis and discusses some ideas for future work.

Chapter 2

Metal 3D Printing for mm-Wave Waveguides

Contents

Motivation for the recent interest in additive manufacturing (AM) for microwave and millimeter-wave metallic waveguide components and antennas is the potential for reduced cost and weight, shorter fabrication times and the ability to fabricate assembly geometries not possible with traditional split-block machining techniques [69]. Metal-coated plastics such as fused-deposition modeling (FDM) and stereolithography (SLA) result in coated surfaces that are fairly smooth. However, components produced by these techniques are fragile, especially combined with other purely metal-

lic components. Instead, direct printing with metal powders can be used: selective laser melting (SLM), or direct metal laser sintering (DMLS) also sometimes called selective laser sintering (SLS). In this chapter, DMLS of metal mm-Wave passive components is quantified. After a brief overview of DMLS processes, a review of rectangular metal waveguides is presented as a context for component design.

2.1 Fabrication Techniques Specific to Rectangular Metallic Waveguides

As will be shown below, hollow rectangular waveguides have two important material needs: highly conductive and smooth walls to reduce loss and mechanically stable construction for intense environments in respect to high power, high thermal stress, and vibration. The main methods of waveguide construction are either destructive, such as CNC milling and electric discharge machining (EDM), or additive, such as electroforming.

Computer numerical control (CNC) milling is an automated machining process which does not easily support hollow structures requiring split block waveguide design. This means that a waveguide must be split in half so that the tool part can access the internal features. Due to current distribution, the best place to cut a rectangular waveguide is along the broad wall (cut the E-plane). Certain feature resolution problems arise with the machine tool radius by rounding corners and with limited flute depth. As internal complexity and frequency of operation increases, resolution becomes crucial. For CNC milling, the cost is also typically based on complexity either through tool activity time or feature based cost analysis. Moreover, this is usually the cheapest of the techniques, and uses materials such as brass, aluminum, and copper.

Electric discharge machining is a destructive process developed to handle more durable materials where a component is created using electrical discharges. The more common method of EDM used in waveguide construction is wire-cut EDM. Here, a cutting wire is one electrode and the work-piece is the other, with voltages of 50 to 300 V between gaps of 0.5 μm to 1 mm. The resulting breakdown

removes conductive material from the component. This technique allows for very fine resolution, extreme aspect ratios, and a smooth surface finish. However, the cost is high and complexity needs to be kept fairly low. This technique also does not easily allow fabrication of hollow components with more complexity than straight bores.

Electroforming is an additive process where electro-deposition occurs on a model-part, known as a mandrel. Conductive mandrels are treated to keep separation either mechanically or chemically-passivated from the electroformed part. After construction, the mandrel has to be separated, ideally intact, but can be melted away or chemically dissolved. A big benefit of this technique is that component complexity can be drastically increased over the other methods and split block construction is not forced. However, electro-deposition is an extremely slow process in comparison to other techniques and expendable mandrels must be used in extremely complex growth. These two downsides lend to the high cost for electroforming.

The two benefits of using additive manufacturing (AM) are the ability to increase complexity of waveguide geometries and features and to reducing cost per feature to a cost per part size. The V- and W-band waveguide components developed in chapters 2 and 3 of this thesis are made using stereolithography apparatus (SLA) with a copper coating and direct metal laser sintering (DMLS) in a variety of metal alloy powders.

2.1.1 Plastic 3D Printing with Electroless Plating

Of the various plastic 3D printing techniques, fused deposition modelling (FDM) and SLA have the largest community usage. The main difference between the two is how material is used to form a solid part. For both, the method of plating consists of a chemically treated surface that allows metal in a solution to adhere to the surface and form a layer larger than the skin depth at the waveguide's operating frequencies.

In FDM, plastic feedstock material is heated and then extruded from a component tip. This molten plastic exits the nozzle and adheres while cooling to the material on the printer bed. Nozzles usually have a diameter between 0.3 mm and 1.0 mm, which limits feature resolution. The printer

adds layer upon layer until the print part is complete. This is the cheapest version of plastic printing and comes with low resolution and usually visible periodic layers. For waveguide construction, this method is not consistent enough for high-frequency operation.

In SLA, an ultraviolet laser is focused into a vat of photopolymer resin. The resin photochemically solidifies to create a layer of the part. The build platform then lowers into the resin and the process reoccurs. Complete parts are then cleaned with solvent to remove uncured resin from the component. In this thesis, commercial SLA process is used to fabricate V- and W-band components that can be compared to metallic AM.

2.1.2 Metallic Additive Manufacturing

In changing to component construction where the feedstock material is metal or metal alloys, three main categories exist: powder-bed systems, powder-feed systems, and wire feed systems. A thorough review of metal additive manufacturing can be seen in [70]. Wire-feed and powder feed systems function on a similar construction technique to FDM.

The technique studied in the work presented here is direct metal laser sintering (DMLS), with selective laser melting (SLM) being a closely related method. DMLS and SLM are powder-bed systems where a laser energy source congeals a solid component layer by layer. Once one layer is complete, the part bed descends and another layer of material is deposited in the work area. Fig. 2.1 displays a standard setup for a powder-bed system. The advantages of these powder-bed systems are the ability to create high resolution features due to small alloy particle size (maybe as low as 30 to 50 μ in diameter), internal voids, and have tight dimensional control. Unlike DMLS, the SLM process has the ability to fully melt the metal feed-material and has the ability to use pure metals.

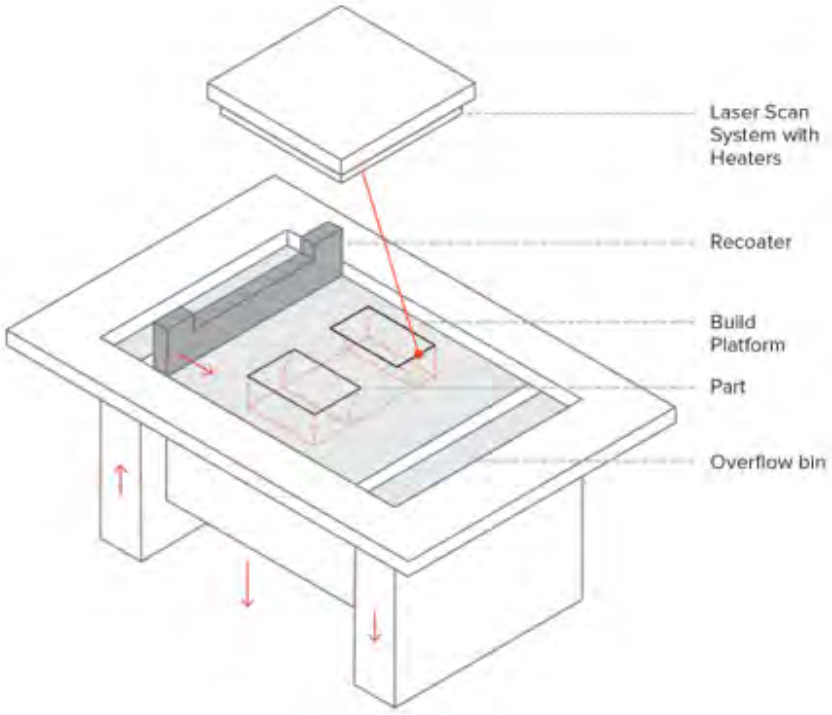

Figure 2.1: A conceptual image of the DMLS printing process [71].

2.2 Why 3D Printing is Good for mm-Wave Waveguide

A majority of work to date demonstrates plated plastic waveguide components using stereolithography (SLA) and fused deposition modeling (FDM). For example, additive manufactured copper-coated SLA waveguides at 10.7-12 GHz replace an antenna feed chain with no signal degradation observed [72]. A lightweight 2-by-2 horn antenna array with a complex feeding network is designed and fabricated for Ka-band using electro-less copper-plated SLA [73]. Split block W-band through lines and 6th-order iris bandpass filters printed using plated FDM and SLA are demonstrated in [74]. The through lines demonstrate attenuation of 11 dB/m at the band edges, while an unloaded quality factor of 152 is measured [74]. This paper also gives a good comparison with existing waveguide components. Groove gap waveguide at Ka-band is printed in metalized SLA with average measured losses of 1.4 dB/m [75]. Termination structures at X-band are characterized in [76], where the printed part is inserted into through lines. Single-block W-band bandpass filters

are designed and fabricated using laser micromachining and copper-plated SLA with good agreement between simulated and measured results [77]. While metal-coated plastic waveguides can be rapidly prototyped and are smooth, they tend to be fragile and the fabrication processes are not commercially available.

Direct printing of bandpass filters for E-band using SLM with Cu-15Sn alloy powder, and a shifted passband and increased insertion loss are observed in [78]. Using SLM with CU-15Sn alloy powder, rectangular through lines are fabricated at E, D, and H bands, with average E-band attenuation of 7.51 dB/m and 7.76 dB/m for 50 mm and 100 mm waveguide lengths, respectively [79].

More recently, metal coated plastic waveguide has been demonstrated from W and D band in [80] up to WR-1.5 (500-750 GHz) and WR-1 (750-1100 GHz) in [81]. High-order SLM waveguide filters with relatively complex internal geometries have been demonstrated with good performance at Ku band, e.g. [82]. However, feature size limitations and additional loss due to surface roughness result in limited performance at higher frequencies. The goal of this work is to quantify performance of V- and W-band waveguide components fabricated using commercially available AM methods. A number of components are designed using full-wave simulation tools starting from fundamental rectangular waveguide principles. Specifically, loss due to material conductivity and surface profile is investigated.

2.3 Rectangular Metal Waveguide Review

At mm-Wave frequencies, hollow metallic waveguides provide superior performance in terms of loss, bandwidth, and power handling compared to planar transmission lines. Although they can have many cross-sectional shapes, the rectangular waveguide is used most often and is the only one discussed here. Metal waveguides do not support TEM modes, but rather a set of modes usually categorized as TE and TM [83, 84]. The rectangular waveguide is useful because it has a dominant TE_{10} mode which is the only one that can propagate within a relatively broad bandwidth. Standard

waveguide bands, such as the ones used in this thesis, this fractional bandwidth is around roughly 40 percent. Fig. 2.2 shows the basic straight metal waveguide with relevant characteristics discussed in the remainder of this thesis.

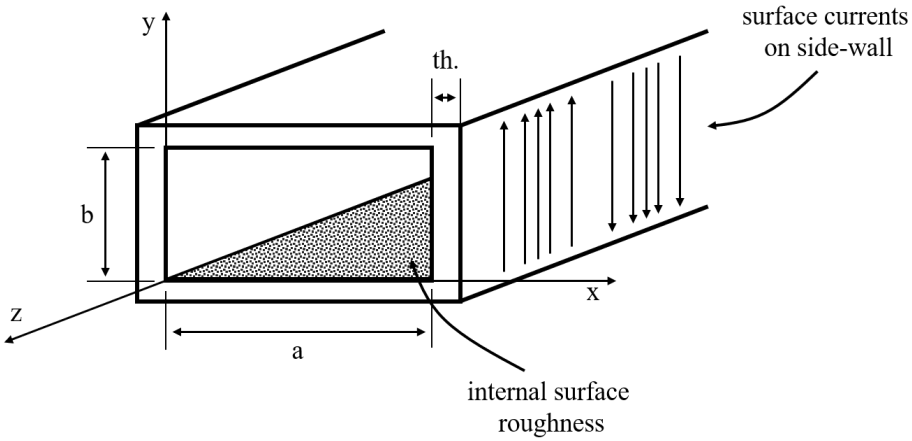

Figure 2.2: Geometry of a rectangular waveguide dimension a and b with transmission in the negative z-direction. Here the thickness, th., needs to be greater than the skin depth at the lowest frequency of operation. A mock-up of a rough surface is shown in the internal portion of the waveguide. The surface current direction and intensity is shown on the sidewalls.

The waveguide dimensions a and b determine the frequency range where the dominant mode exists without any other modes. Within this range, a single dispersive wave impedance can be derived from the wave equation and appropriate boundary conditions [83, 84] and is given by:

$$Z_{TE,10} = \frac{\mathrm{E}_y}{\mathrm{H}_x} = \frac{\sqrt{\frac{\mu_0}{\epsilon_0}}}{\sqrt{1-\left(\frac{f_{c10}}{f}\right)^2}} \quad \text{where} \quad f_{c,10} = \frac{1}{2\pi\sqrt{\mu_0\epsilon_0)}}\sqrt{\left(\frac{\pi}{a}\right)^2} \tag{2.1}$$

Refering to Fig. 2.2 the wave propagates in the negative z-direction at a frequency f where the phase constant is given by:

$$\beta_{10} = 2\pi f\sqrt{\epsilon_0\mu_0}\sqrt{1-\left(\frac{f_{c,10}}{f}\right)^2} \tag{2.2}$$

And the corresponding guided wavelength is this:

$$\lambda_g = \frac{2\pi}{\beta_{10}} = \frac{1}{f\sqrt{\mu_0\epsilon_0}\sqrt{1-\left(\frac{f_{c,10}}{f}\right)^2}} \tag{2.3}$$

The propagation constant $\gamma = \alpha + j\beta$ contains an attenuation constant α which is a result of conductor loss, surface roughness loss, and in general mismatch loss. In our case, there is no dielectric loss as all waveguides are airfilled.

If β is imaginary at a specific frequency (below cutoff for a specific mode), then the mode becomes heavily attenuated and it's impedance purely imaginary. This contributes to mismatch loss as described in [84] in the context of waveguide discontinuities.

Conductor loss for a smooth waveguide wall is given by the skin effect. The power loss due to the conductors can be calculated by integrating the square of the surface current on the waveguide walls multiplied by the surface resistance [85]. Because all quantities are a function of frequency within the operating band, the attenuation due to conductor loss is frequency-dependent. This loss can be minimized by choice of conductor and plating with inert metals. However, the conductor is not perfectly smooth, and this is especially the case in AM components. Loss due to surface roughness is not as well-established as other loss mechanisms in a waveguide. Qualitatively, this loss is due to a longer path that the surface current travels as it follows the conductor profile. However, this will obviously depend on shape, size, and quasi-periodicity of the profile.

2.3.1 Surface Roughness Effects

In 3D printed components at mm-Wave, the surface roughness loss becomes comparable to conductor loss. To the author's knowledge, the only paper to directly apply surface roughness attenuation to rectangular waveguide excited in the mode TE_{10} is [86], where a formula is derived for loss due to finite conductivity waveguide walls with empirical correction factors that account for roughness. The problem with this method is the difficulty in calculating each factor with a lack of ambiguity.

Attempts to describe the interaction between EM waves and rough surfaces date back to at least Lord Rayleigh [87]. In an oft-cited paper, [88] derives quasi-static eddy-current problem for a

two-dimensional (2D) periodic ridge structure, and derives a power absorption 'enhancement' factor to account for additional losses due to surface geometry. In an extension, [89] this factor is used to fit an empirical model, which has been the most used formula for quantifying conductor surface roughness on loss which is implemented in contemporary CAD tools. However, in previous work [90], it is shown that for increasing frequency, the Hammerstad enhancement factor saturates at a value of 2 and does not accurately describe surface roughness loss for high-frequency components [90].

Methods have been proposed to more accurately describe surface roughness loss in two ways for both two dimensional and three-dimensional (3D) cases: periodic and random scattering. For periodic roughness, finding an equivalent surface impedance is a standard route for solving this problem. In two well-cited papers, Holloway and Kuester describe a 2D periodic rough surface by a generalized impedance boundary condition and find a power loss associated with that generalized impedance, where special care is taken to properly enforce the boundary condition [91], [92]. Wu and Davis, in an extension from Morgan's paper, use a square groove surface model to find an equivalent surface resistance and reactance [93]. Matsushima and Nakata use a local surface impedance and apply an equivalent current source method to find power loss at that surface [94]. Lukic and Filipovic model 3D and 2D surface roughness using periodic cubical, semiellipsoidal, and pyramidal indentations, as shown in Fig. 2.3 , and their 2D equivalents using finite-element methods , [95]. Huray created a "snowball" method where the scattering from copper spheres stacked into pyramidal shapes is charaterized into power loss [96]. Huray leaves open the possibility of different distributions for ball stacking. In a recent extension, Yi proposes a modified Huray model for substrate-integrated waveguide and compares to D-Band measurements [97].

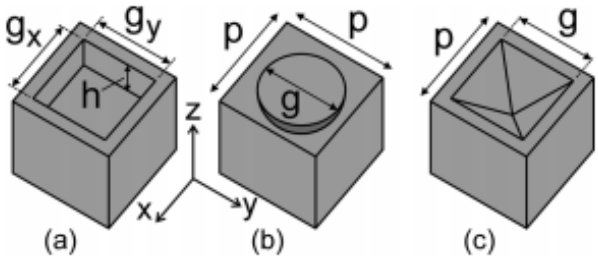

Figure 2.3: Unit cells of periodic: (a) cubical, (b) semiellipsoidal, and (c) pyramidal indentations in a conductor surface. Image taken from [95].

Sanderson uses the Rayleigh-Rice method for 2D periodic grooves on propagation of the TEM mode in a parallel-plate guide [98]. Rayleigh-Rice/Fano method, also called small perturbation method (SPM) with varying orders of complexity, can be described in [87], [99], [100]. Proekt and Cangellaris formulate a first-order perturbation method for a periodically corrugated 2D surface and derive an effective conductivity including the effect of surface roughness [101].

In initial approaches to random rough surfaces, Wait [102] and Biot [103] both describe a 3D rough surface model with different distributions of hemispherical "bosses" in conducting plane. In a large spread of papers, Tsang and Braunisch begin dealing with random surface roughness in 2D and 3D cases (as seen in Fig. 2.4) for dielectric and conductive medium by using the second-order small perturbation method (SPM2) [104–108]. These all take into account that the power spectral density (PSD) of a rough surface is equivalent to the fourier transform of the correlation function. Ruihua, Tsang, and Braunisch in [107] and [108] apply SPM2 in parallel-plate waveguide for finding coherent wave propagation and power loss.

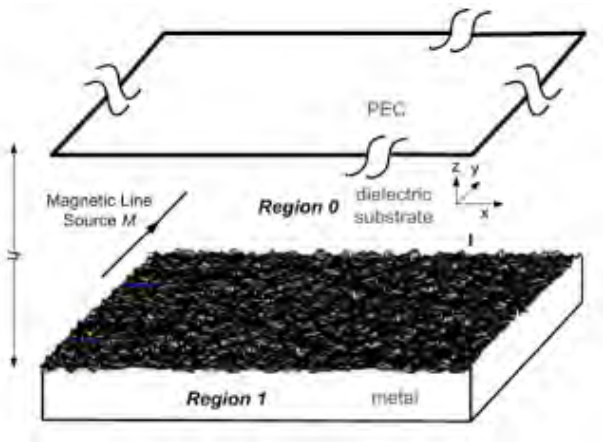

Figure 2.4: A 3D model of a parallel plate waveguide with random surface roughness; image taken from [108].

In previous work [90] and shown in Chapter 3, the correlation function for 3D surface roughness in direct metal laser sintered (DMLS) V- and W- band waveguide is found and root mean square height and autocorrelation lengths established for various metallic powders. Thus the small perturbation method is promising for directly correlating the measured surface characteristics to waveguide power loss.

The goal of this work is to quantify the performance of surface roughness on mm-Wave components from 3D printing. To that end, a number of components have been designed to test attenuation, performance over achievable feature size.

2.4 Waveguide Component Designs

A 10 cm straight section, 20-dB coupler, and filter W-band waveguide components, shown in Figs. 2.5, 2.6, and 2.7, are designed as single pieces. In addition, an 11 cm straight section, 20-dB coupler, and filter waveguide components are designed in V-band. Lastly, we designed two V- and W-band power splitters.

The waveguide components are designed using finite-element modeling (HFSS) with measured conductivity data assuming smooth walls. All designs use standard UG-387 for WR-10 and WR-15

(MIL-DTL-3922/67E) flanges to connect to existing standard waveguide in the lab. Some of the components include an "anti-cocking" ring around the edge of the flanges. This outer flange ring helps prevent misalignment due to part angle and varied screw tightness during testing.

Figure 2.5: Photograph of straight 10-cm WR-10 waveguides implemented in a variety of materials. From left to right: metal (Cu) coated plastic (MCP), GRCop-84 (Cu), Inconnel 625 (Ni), 3 AlSi10Mg with different laser settings, and maraging steel (MS).

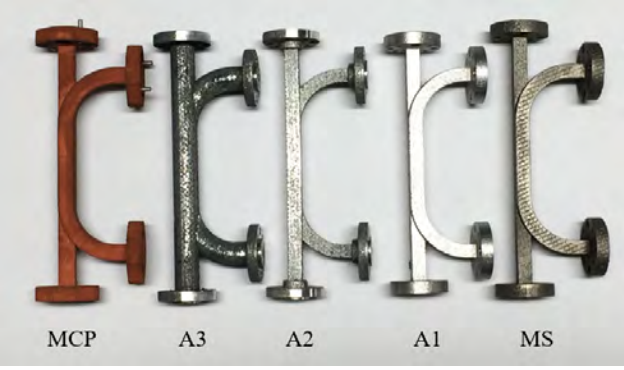

Figure 2.6: Photograph of WR-10 20-dB waveguide couplers implemented in a variety of materials. From left to right: metal (Cu) coated plastic (MCP), 3 AlSi10Mg with different laser settings, and maraging steel (MS).

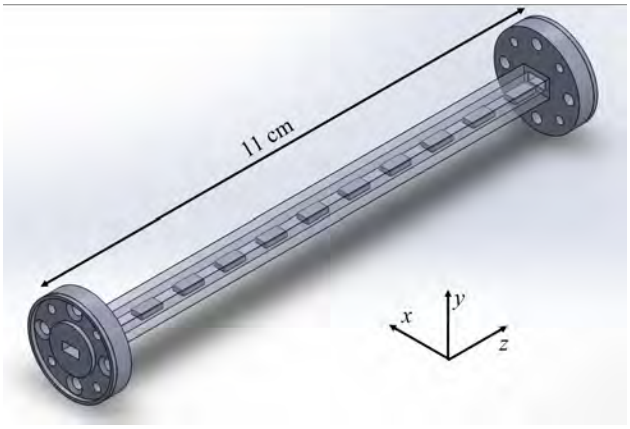

Figure 2.7: 3D view of WR-10 filter waveguide section with a transparent midsection. The filter is comprised of 11 blocks of the same width, height, and depth in a WR-10 straight waveguide section. A similar filter was designed for V-band in WR-15 waveguide.

The simulated WR-10 20-dB coupler design uses 12 identical round coupling holes in a periodic array. The resolution of the DMLS process allows for a minimum wall thickness of 0.3 mm and a minimum feature size of 120 μm. The WR-10 20-dB coupler DMLS design utilized a 0.508 mm hole diameter and a horizontal (defined here as "along-guide", vertical being "across-guide') center-to-center hole spacing of 1.375 mm. Fig. 2.8a shows the fabricated dimensions of the WR-10 component. Because of the SLA process limitations, a second WR-10 coupler was designed with a larger hole spacing at the expense of bandwidth.

The WR-15 20-dB coupler design uses 14 identical round coupling holes in a periodic array. The DMLS fabricated WR-15 20-dB coupler design utilizes a 0.62 mm hole diameter and a horizontal center-to-center hole spacing of 1.99 mm and a vertical center-to-center hole spacing of 2.33 mm. Fig. 2.8b and 2.8c illustrate the dramatic printing improvement with WR-15's larger dimensions.

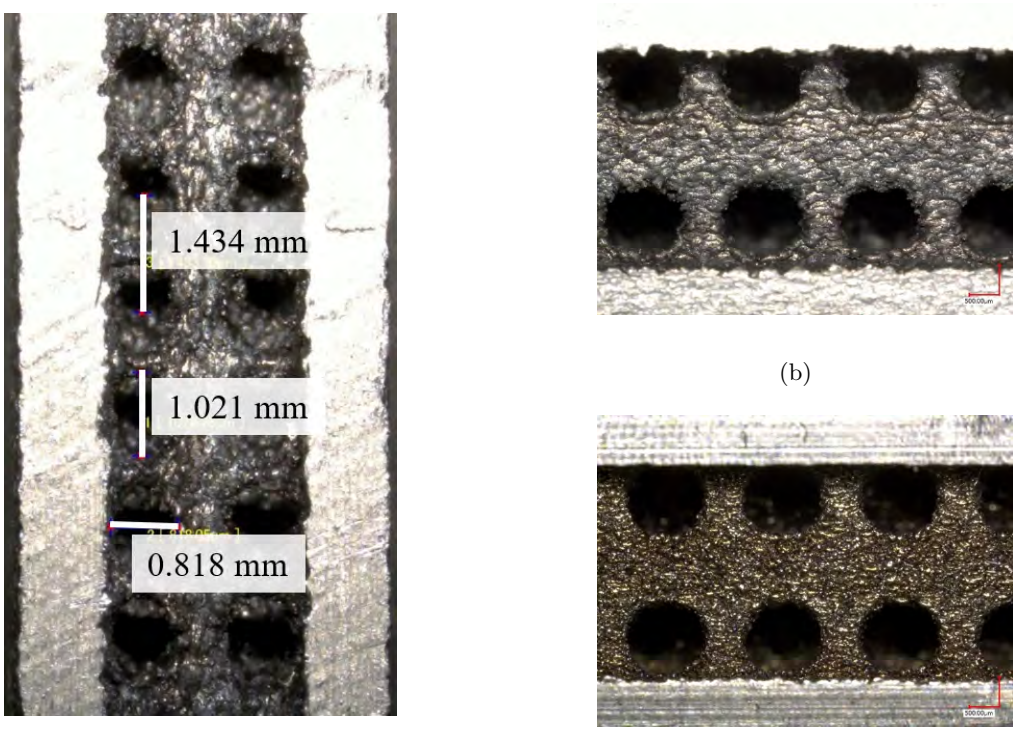

(a)

(b)

(c)

Figure 2.8: Photographs of the interior coupling holes of 20-dB directional couplers after destructive testing (a) the WR-10 A1 component with measured dimensions, (b) the WR-15 AlSi10Mg component, and (c) the WR-15 MS component. Measured dimensions for (b) and (c) are discussed in section II.B, Fig. 5, and Table II. The images are created using FVM at x50 magnification.

The symmetrical filter design uses 11 blocks with consistent height, width, and depth for both WR-10 and WR-15. Tolerance issues with the DMLS process were taken into account during the design process. Fig. 2.7 shows this design for WR-10 clearly. Both WR-15 and WR-10 waveguide filter designs were created in AlSi10Mg and MS1.

The splitter design is not a standard E-plane geometry as in [109], but instead attempts to improve return loss and coupled-port isolation using a septum similar to what is presented in [110] and [111]. Fig. 2.9a shows the overall geometry. The inherent loss due to surface roughness of AM manufacturing is estimated based on [90] and used in the design to provide a resistive septum analogous to a Wilkinson divider, shown in detail in Fig. 2.9b. Instead of a stepped impedance,

the work presented here uses a continuous taper enabled by additive manufacturing, indicated in Fig. 2.9a at waveguide ports 2 and 3. Further, the 3D printing allows output ports (2 and 3) to be colinear with port 1.

The simulated S-parameters of the splitters assuming smooth waveguide walls with loss associated skin depth in maraging steel is shown in Fig. 2.10, and compared to the performance of a standard E-plane splitter. Notice that the septum and tapered impedance ports contribute to improved input match ($|S_{11}|$) and isolation ($|S_{32}|$). We expect that the measured insertion loss will be increased due to surface roughness.

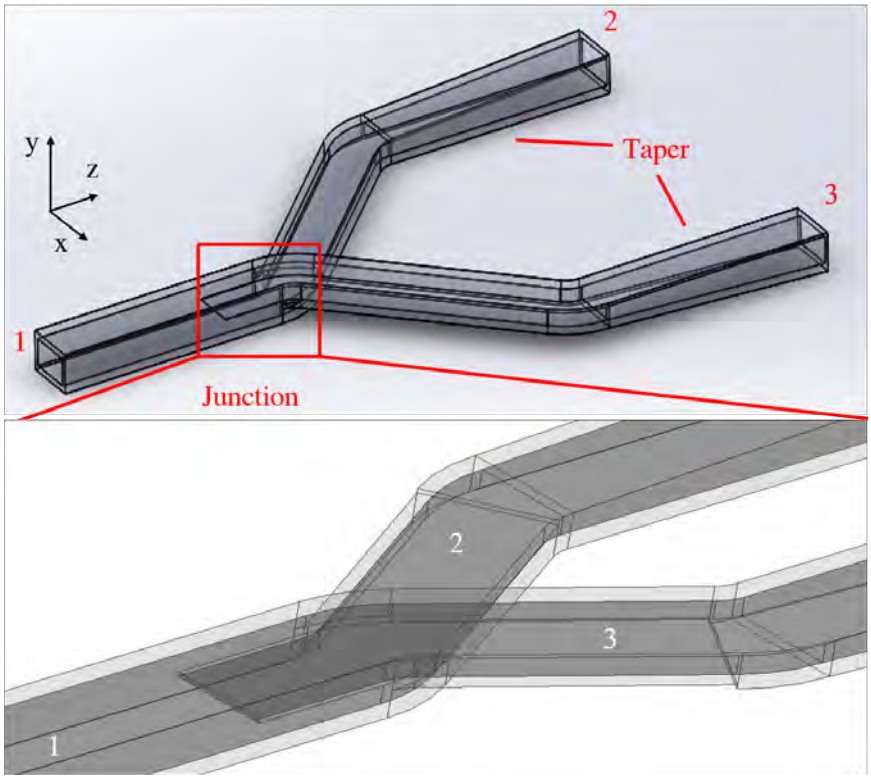

Figure 2.9: (a) Transparent 3D-view of the WR-15 waveguide splitter showing continuous tapered impedance waveguide ports 2 and 3. (b) Zoomed-in junction showing septum (width of 0.05 mm) for V band. WR-15 and WR-10 aperture dimensions for designed components are 3.7592 mm $\times$ 1.8796 mm and 2.54 mm $\times$ 1.27 mm, respectively.

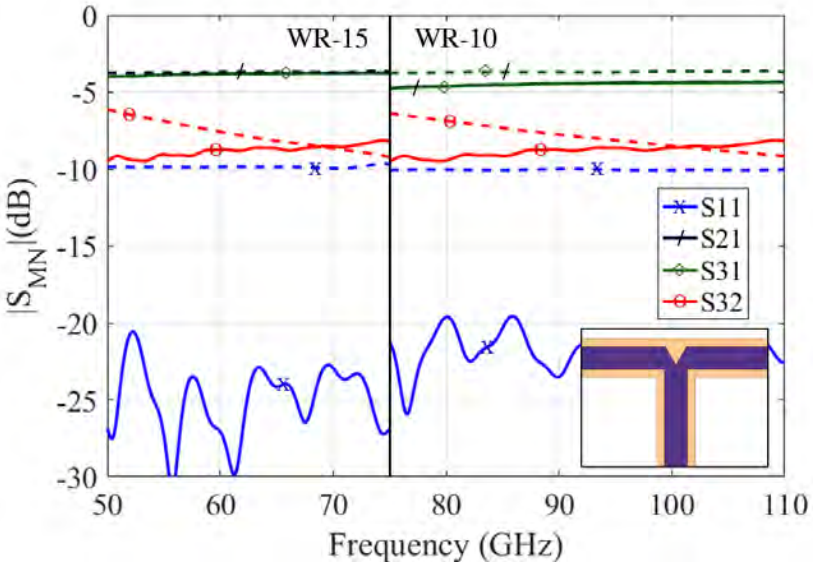

Figure 2.10: Simulated S-parameters for the V- and W-band splitters using conductivity of maraging steel [90], $\sigma = 2.05 \times 10^6\,\mathrm{S/m}$, and assuming smooth walls. The performance of the splitter geometry from Fig.2 (as solid lines) is compared to a standard E-plane splitter shown in the inset (as dashed lines).

2.5 Waveguide Component Fabrication Details

The DMLS process in this work uses 20-40 μm metal particles that are sintered together with a Yb-fiber laser with a focused finite spot diameter that varies in both size and intensity with output power. Table 2.1 lists the machine standard settings (laser power, focus diameter, and scan speed) employed by different manufacturers. Since waveguide features at millimeter-wave frequencies are usually smaller than 100 μm, different laser scanning strategies are employed. Typically, laser output power, spot speed, and distance between multiple sintered lines, hatches, are varied.

During the sintering process, the direction of the component build fundamentally changes the spatial resolution of internal features and measured surface roughness. For clarity in the build direction, as denotated in Fig.2.7, the xy-plane is defined as the machine bed and powder is layered upward in the z-direction. In the straight sections, the build direction is straight upwards (z-

direction) from the build plate with the flanges parallel to the build plate (xy-plane) of the DMLS machine. For the internally complex components, the 20-dB couplers and the filters, there are always a few walls with no structural support during build. This lack of support causes the melt pool to bend downward into untouched powder space. In order to minimize this bend, the component is tilted in the xz-plane by 45°. The part is still built along the z-direction.

Table 2.1: DMLS Processing Parameters

	Machine	Power (W)	Focus (μm)	Scan Speed (mm/s)
Midwest Composite	M270/280	200 or 400	100	750
Visser Precision	M290	400	100	500-850

2.5.1 Materials Used

Various metallic alloys in powder form are available for direct metal laser sintering; in this work we use AlSi10Mg, an aluminum alloy, GRCop-84, a copper alloy referred to as Cu, MS1, maraging steel referred to as MS, and Inconel 625, nickel chromium superalloy referred to as Ni. These parts were printed on Electro Optical Systems (EOS) DMLS machines EOSINT M270/M280 and EOS M290 through manufacturing suppliers Midwest Composite and Visser Precision respectively. The stereolithography components were plated in copper using a proprietary electro-less process via supplier Swissto12; these parts are referred to as MCP.

Conventional 4-point probe resistivity testing was performed on both MS1 and AlSi10Mg parts. The measured conductivity for MS1 is found to be 1.60x10^6 S/m; the measured conductivity for AlSi10Mg is found to be 2.66x10^7 S/m. A summary of the material properties and referred names are shown in Table I.

Table 2.2: Metal Powder Alloy Properties

Alloy	Referred Name	Bulk σ (S/m)	Measured σ (S/m)
MS1*	MS	2.05x10^6	1.60x10^6
AlSi10Mg**	A1, A2, A3	1.8-2.5x10^7	2.66x10^7
Inconel 625***	Ni	7.75x10^5	-
GRCop-84****	Cu	4.17x10^7	-

* For more information on MS1 see EOS material list.

** For more information on AlSi10Mg see EOS material list and [112].

*** For more information on Inconel 625 see EOS material list.

**** Taken at room temperature. For more information on GrCop-84 see [113].

2.5.2 Fabricated Components

In this work, three WR-10 AlSi10Mg straight components (A1, A2, and A3) are printed as can be seen in Fig.2.5. A1 (Midwest Composite) and A2 (Visser Precision) are printed using the standard manufacturer settings seen in Table 2.1. A3 (Visser Precision) is printed with higher energy density in the perimeter scan. In using a higher energy density, less surface roughness occurs, however, the component has reduced feature resolution. The W-band couplers are also printed in all the same materials minus the GRCOP-84 and Inconel 625. Both a W-band straight section and a W-band 20-dB coupler were printed in SLA and coated in copper from Swissto12.

The V-band 11 cm straight, V-band 20-dB coupler, and V- and W-band filter waveguide components are only printed in two DMLS alloys, AlSi10Mg (aluminum) and MS1 (maraging steel).

The splitter components shown in Fig. 2.11 are fabricated by MidWest Composite Technologies [114], using M270/280 EOS machines with a laser power of 200/400 W, focus of 100 μm and a scan speed of 750 mm/s. The direction of growth is in the $-z$ direction as denoted in Fig. 2.10. The

only post-processing of the components are the center-tapped holes in the flanges.

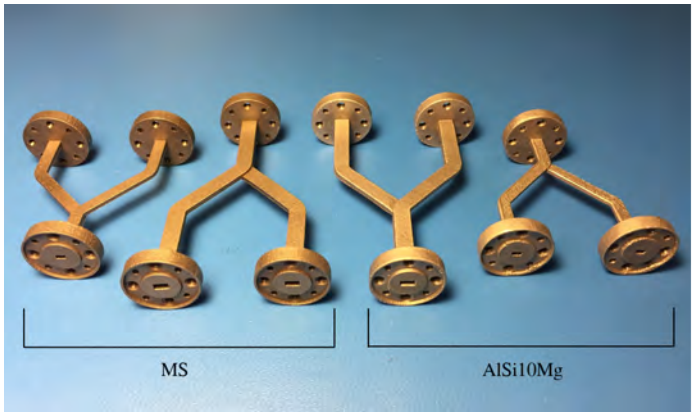

Figure 2.11: Photograph of WR-10 and WR-15 waveguide 3-dB splitters implemented in maraging steel (MS) and aluminum alloy ($AlSi_{10}Mg$). The $AlSi_{10}Mg$ components were not functional due to poor printing tolerances that could not meet the dimensions of the internal splitter design geometry.

2.6 Conclusions

Here, a series of waveguide components are designed to test various capabilities of metallic additive manufacturing over different alloys, in particular of surface roughness and internal printing resolution of complex features, and between two techniques, metal-coated plastic and direct metal laser sintering. Waveguide designs for both V- and W-bands with straight waveguides, 20-dB couplers, and corrugated filters were designed using HFSS. Additionally novel power splitters that use geometries only 3D-printing can provide were created.

As the field has progressed rapidly in the few years since this work was published [90] and [115], a revisit to the print-able alloys and geometries would be of interest for future work. As well, there is interest in scaling to higher frequencies in waveguide such as W-band to D-band transitions and increasing complexity in D-band waveguide structures.

Chapter 3

Additively Manufactured Component RF Performance and Surface Roughness Analysis

Contents

3.1 RF Measurement

The fabricated designs from the previous chapter are next characterized in terms of RF parameters and fabrication tolerances. RF performance is shown in this section for the waveguide components shown in Figs. 2.5, 2.6, and 2.7 fabricated in different materials as discussed in Ch. 2. The RF performance was measured with an HP8510C with W85104A W-band and V85104A V-band fre-

quency extenders. Calibration was performed using calibration kits HP W11644A for WR-10 and V11644A for WR-15, resulting in $|S_{11}|$ < -30 dB for the termination standards.

3.1.1 Straight Waveguide Sections

The measured $|S_{21}|$ parameters of the straight 10 cm WR-10 waveguide sections are shown in Fig. 3.1. While $|S_{11}|$ < -10 dB for nearly all WR-10 straight 10 cm components, $|S_{21}|$ varies for each material and best performance across-band is observed with MCP. In reference to the aperture mismatch, A2 can be seen having a fairly flat response as the component was close to design. The Cu component has a consistently large standing wave across-band. Ni and A1 have poor responses across the entire band.

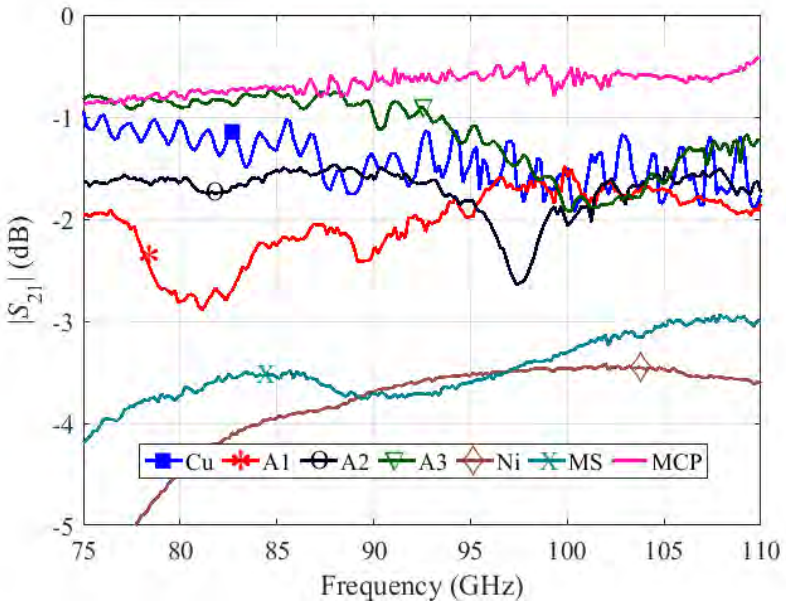

Figure 3.1: $|S_{21}|$ data for the various fabricated WR-10 10 cm waveguide sections. It is assumed the standing wave patterns or poor across-band response is due to aperture dimension deviation and/or imperfect flange mating.

For the WR-15 straight 11 cm waveguide sections in maraging steel and aluminum, Fig. 3.2 shows $|S_{21}|$ data. Using the measured conductances described in section II.A, components in HFSS

were simulated and are shown in Fig. 3.2 for a comparison between design and printed. While $|S_{11}|$ < -20 dB for both components, $|S_{21}|$ varies for each material and a flat performance across-band is observed with MS.

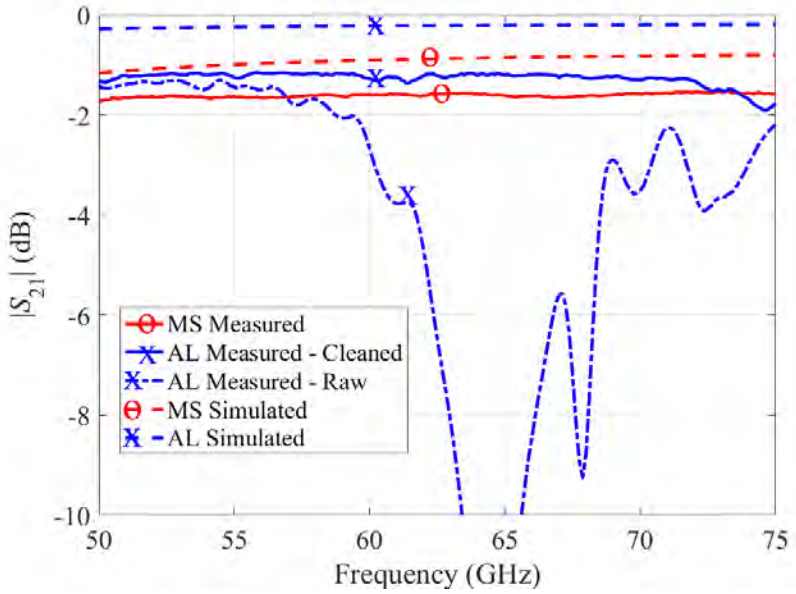

Figure 3.2: $|S_{21}|$ data for the fabricated WR-15 11 cm waveguide sections. The easily visible misprinted threads in the AlSi10Mg, as discussed in this section, are assumed to be causing significant amounts of reflections. The response improves after cleaning. The HFSS simulation data using the conductivity results of the four point probe measurements are included.

With this specific production run, another printing problem was found in the AlSi10Mg. Thin stalactites, stalagmites, and threads of metal connecting walls are easily visible within the waveguide. This phenomenon is explained by liquid metal expulsion [116]. During lasering and due to differing pressures, a recoil force can exist on the melt pool causing liquid metal to be expelled onto cooled surfaces. In the first measurement of this aluminum part, these "misprints" caused significant reflection loss at unexpected frequencies. After cleaning the AlSi10Mg waveguide section with a non-abrasive material (so that surface roughness was left intact) and subsequently flushing with acetone, the large drops in $|S_{21}|$ are removed and a flatter response is seen. A summary of the S-parameter data for both WR-10 and WR-15 straight components at center frequencies (92.5

GHz for W-band and 62.5 GHz for V-band) is given in Table V.

Table 3.1: S-parameter data for WR-10 and WR-15 at center frequencies

Band	Material	$\lvert S_{21}\rvert$ (dB)	$\lvert S_{11}\rvert$ (dB)
WR-10	Cu	-1.22	-14.87
WR-10	AlSi10Mg A1	-2.01	-14.84
WR-10	AlSi10Mg A2	-1.64	-22.37
WR-10	AlSi10Mg A3	-0.90	-17.91
WR-10	MS	-3.88	-20.50
WR-10	Ni	-3.59	-37.03
WR-10	MCP	-0.57	-24.87
WR-15	AlSi10Mg	-1.58	-31.53
WR-15	MS	-1.21	-21.29

3.1.2 4-port Couplers

The S-parameters of the various WR-10 20-dB couplers are shown in Fig. 3.3. The AlSi10Mg couplers achieve close to 20 dB coupling ($|S_{31}|$) but the transmission coefficient $|S_{21}|$ is far below desired and the response is not flat. The MCP coupler has less loss than the other components and a mostly flat response; however, the coupling factor is not as designed. The MS coupler performs best; the 20-dB coupling is extremely flat across-band and the observed $|S_{21}|$ is expected due to the material conductivity. The A3 AlSi10Mg coupler has physically blocked innards due to printing issues. As such, the A3 AlSi10Mg sample has no through transmission ($|S_{21}| \ll 0$ dB) and is excluded from Fig. 3.3. $|S_{11}|$ is < -10 dB on average for all components, with $|S_{11}|$ < -20 dB for the MS coupler and isolation $|S_{41}|$ < -20 dB on average for all components.

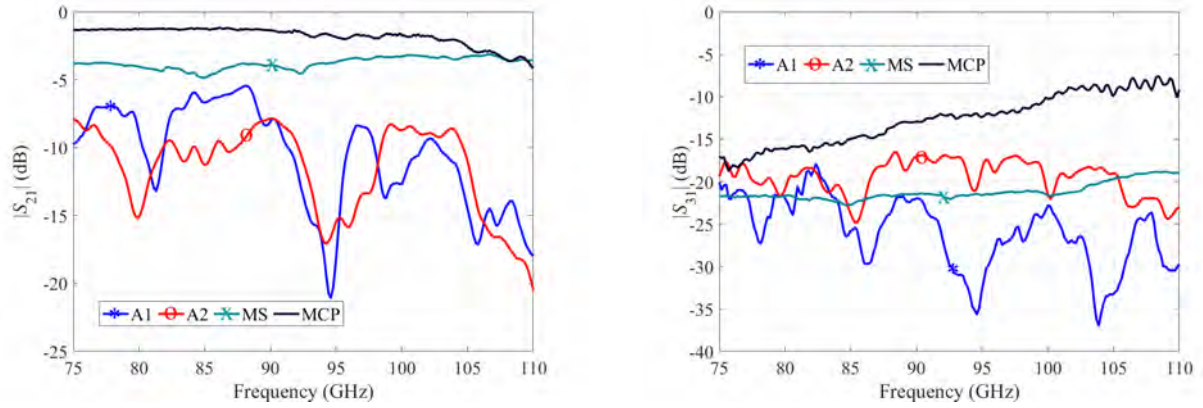

(a) (b)

Figure 3.3: (a) $|S_{21}|$ and (b) $|S_{31}|$ data for the various WR-10 20-dB couplers.

The S-parameters of both WR-15 20-dB couplers are shown in Fig. 3.4. The MS coupler performs best; the response is extremely flat across-band in both $|S_{21}|$ and $|S_{31}|$ and matches closely the simulated maraging steel data.

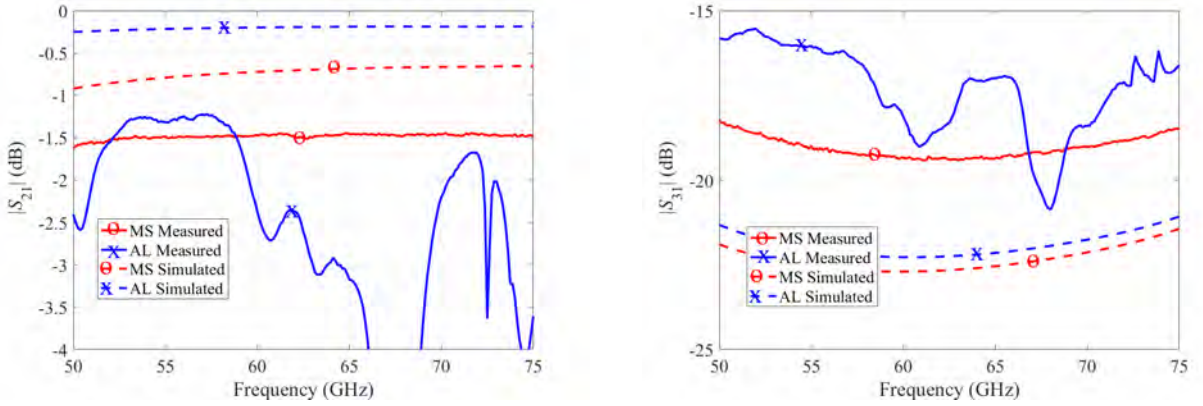

(a) (b)

Figure 3.4: (a) $|S_{21}|$ and (b) $|S_{31}|$ data for the various WR-15 20-dB couplers. S-parameter data from simulated couplers using the measured 4-point conductivity is also shown.

The printing issues in this production run also plagued the AlSi10Mg coupler. Unlike the straight section, the complexity of the coupler does not allow for a thorough cleaning. On average, $|S_{11}|$ is $<$ -20 dB for both WR-15 components and $|S_{41}|$ is $<$ -30 dB on average for both components

with the WR-15 MS coupler $|S_{41}|$ consistently below -40 dB.

3.1.3 Filter Structures

The WR-15 filter sections are designed to have a passband from around 61 GHz to 65 GHz. In Fig. 3.5, the simulated filter's $|S_{21}|$, using a perfect electric conductor, is shown in black and the $|S_{21}|$ and $|S_{11}|$ data of the MS and AlSi10Mg are shown in red and blue respectively. The null around 64 GHz in the MS could be attributed to liquid expulsion or misprints in corrugation edges.

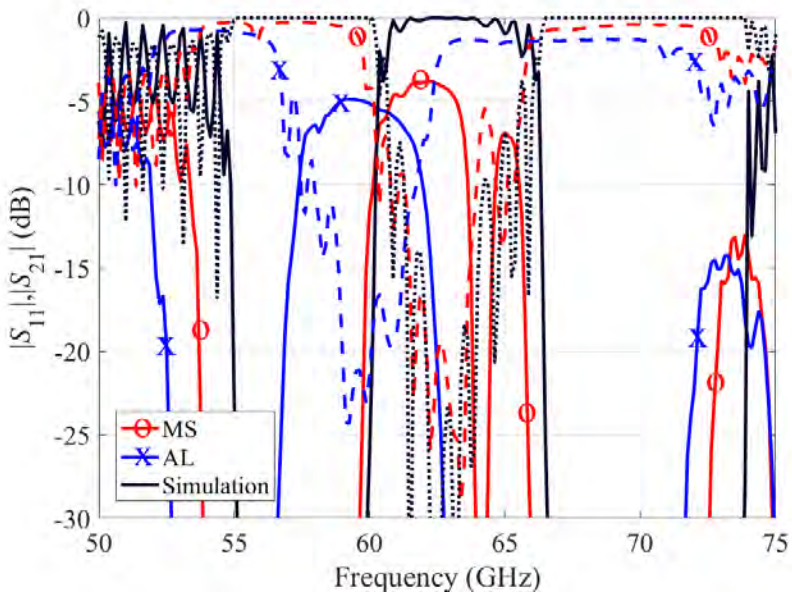

Figure 3.5: $|S_{21}|$ (solid line) and $|S_{11}|$ (dashed line) data of the WR-15 filter waveguide components. The simulated filter $|S_{21}|$ data using a perfect electric conductor is shown in black.

In comparison to the simulation, the passbands of the printed components are shifted. The shift on AlSi10Mg is more significant than the MS filter. Notice here that the through transmission, $|S_{21}|$, of the AlSi10Mg passband is close to, if not less than, the MS $|S_{21}|$. Solely based on conductive loss, the aluminum alloy's $|S_{21}|$ should be about 1 dB less than the maraging steel. However, inconsistent printing issues in the whole aluminum piece cause these shifts and degradation in RF performance.

The loaded and unloaded quality factor, Q_L and Q_U, are found using

$$Q_L(f_0) = \frac{f_0}{\Delta f} = Q_U(f_0) * (1 - |S_{21}(f_0)|) \tag{3.1}$$

where Δf is the 3-dB bandwidth and f_0 is the center frequency [74]. A summary of the loaded and unloaded quality factors from printed and simulated WR-15 filters is contained in Table 3.2. The ideal Q is for a perfect electric conductor.

Table 3.2: WR-15 filter Q, loaded and unloaded

	Q_L	Q_U
AlSi10Mg	14.03	32.29
MS	19.34	53.50
Ideal	11.62	199.58

3.1.4 3-port Splitters/Combiners

The $AlSi_{10}Mg$ components were not functional due to poor printing tolerances that could not meet the dimensions of the septum and decreased internal height. Figure 3.6 show the measured input match, coupling, insertion loss and isolation of the maraging steel components compared to simulations.

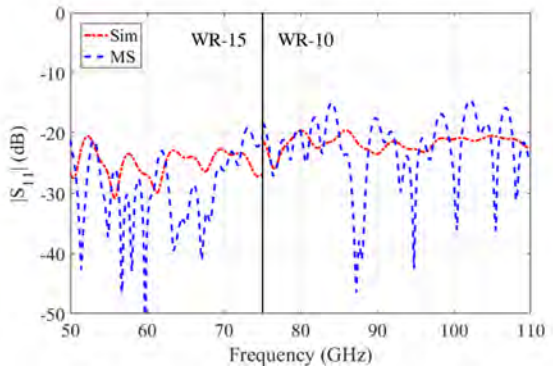

(a)

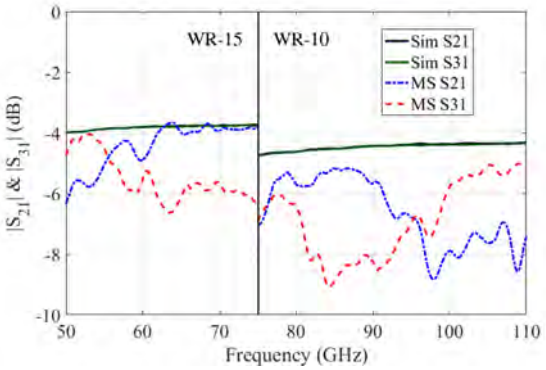

(b)

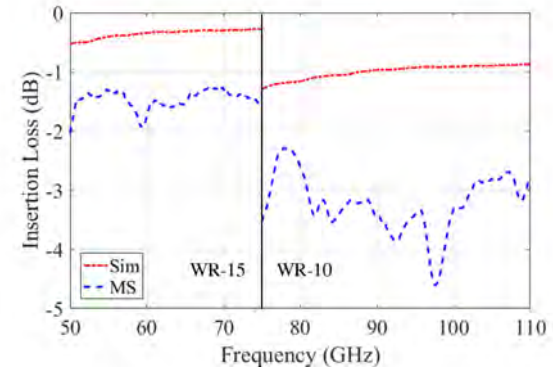

(c)

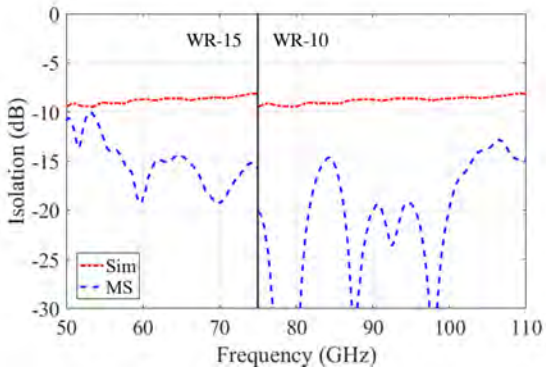

(d)

Figure 3.6: Simulated (using MS conductivity measured in [90]) and measured (a) reflected power, (b) power split, (c) insertion loss, and (d) isolation of the WR-10 and WR-15 splitters.

Fig. 3.6a shows the measured input match agrees with the simulations across both bands. In Fig. 3.6b there is a 2-dB asymmetry between the two ports over the band, which is discussed in the next section. The insertion loss in Fig. 3.6c is calculated as

$$IL = 20 \log \frac{|S_{21}| + |S_{31}|}{\sqrt{2}} \tag{3.2}$$

The insertion loss is 1.5 dB higher than the predicted value over V-band and 2 dB over W-band. The simulations do not include surface roughness, and the increase in loss is consistent with the results quantified for maraging steel in [90] for the component lengths in Fig. 3.6d. The additional

loss due to surface roughness, compared to that in Fig. 2.10 which only takes into account the skin-effect loss, is estimated to be 10.8 dB/m at 62.5 GHz and 33.9 dB/m at 92.5 GHz, consistent with the results in [90]. The isolation between ports 2 and 3 (Fig. 3.6d) shows improved isolation due to increased loss, as expected.

3.2 Feature Analysis

Precise feature printing becomes a critical issue in the construction of functionally more complex components. Here we characterize the complex internals of the WR-15 waveguide components and the apertures of the WR-10 waveguide components in relation to designed specifications.

3.2.1 Coupler Holes

In DMLS, the internal coupling holes are created using a varied hatch pattern per deposition layer due to the lack of support at the hole edges and suspension between guides. During the cooling of the melt pool at each layer, the edges of the coupling holes harden with a roughness difficult to predict. The edge roughness is quantified by the root mean square deviation (RMSD) from the designed hole to the printed one. In addition to finding the hole RMSD, the horizontal and vertical center-to-center hole spacing is determined and compared to specification.

Using focus variation microscope (FVM) images at magnitudes of 100 and 50 and a generalized Hough Transform on a Canny-filtered image with techniques developed in [117] and [118], the center-point of a single hole can be found and then used to overlay a circle with the dimensions of the WR-15 coupler design. The original image is then segmented by using a Fast Marching Method based on pixel weights derived from the image gradient; using the center-point, the algorithm radially sweeps the segmented image to find the coupling hole edge, overlay-ed on the original image as shown in Fig. 3.7. This analysis is also performed on the images shown in Fig. 2.8b and 2.8c for finding the center-points of each hole. Using these points, the vertical and horizontal center-to-center hole spacing is determined.

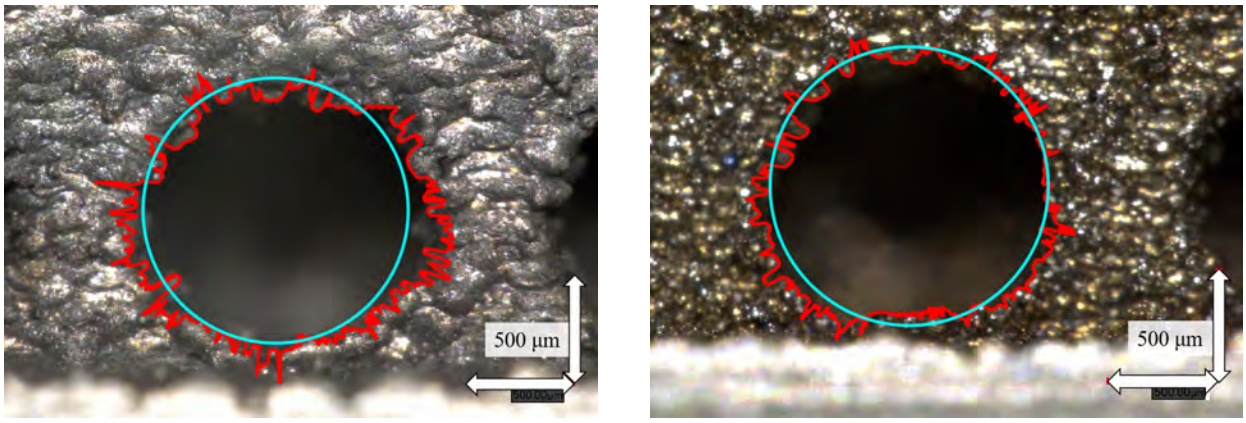

(a) (b)

Figure 3.7: WR-15 20-dB coupler holes images (a) AlSi10Mg and (b) MS1 with superimposed lines for the designed hole specification and an algorithmically-found printed edge (jagged line). The images are created with FVM at x100 magnification. The scale shown is 500 μm.

A summary of WR-15 coupler hole misalignment with comparison to designed specifications is shown in Table 3.3. The maraging steel has better edge structure, as evidenced by root mean square deviation, and is generally closer to designed center-to-center spacing than the AlSi10Mg component.

Table 3.3: WR-15 coupler hole misalignment

	RMSD (μm)	Avg. Horiz. (mm)	Avg. Vert. (mm)
AlSi10Mg	83.8	1.95	2.22
MS	50.2	1.94	2.31
Ideal	0	1.99	2.33

3.2.2 Corrugations

For the filter, the deviation between fabricated and simulated geometric features is essential for frequency response modeling. Fig. 3.8 shows fabricated dimensions; both components deviate from

the designed structure. The maraging steel is smaller in total area whereas the AlSi10Mg is slightly longer horizontally but smaller vertically than designed. The maraging steel corrugation is shifted closer to one sidewall.

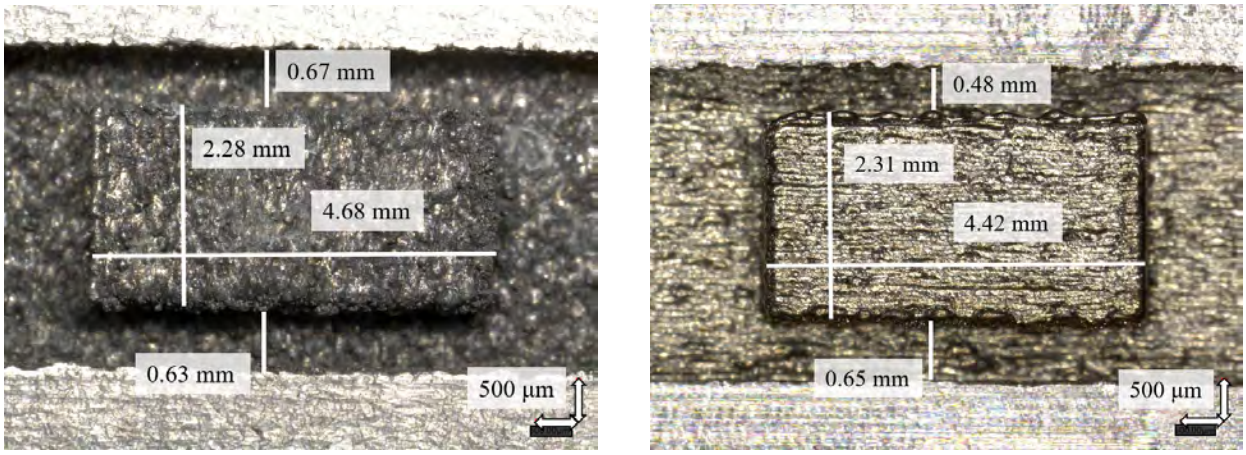

(a) (b)

Figure 3.8: WR-15 filter images centered on the raised blocks, taken with FVM at a magnitude of 50, with overlay-ed lines for measured distances. The scale shown is 500 μm.

A summary of the WR-15 filter corrugation size and misalignment is shown in Table 3.4.

Table 3.4: WR-15 filter corrugation size and misalignment

	Vert. (mm)	Horiz. (mm)	Avg. Wall Deviation (μm)
AlSi10Mg	2.28	4.68	29.6
MS	2.31	4.42	114.6
Ideal	2.4	4.63	0

3.2.3 Aperture Mismatch

A feature issue that becomes more visually obvious at WR-10 proportions than WR-15 is misprinted aperture dimensions. Fig. 3.9 shows four FVM images of the WR-10 waveguide apertures in different materials. By standard designation, WR-10 aperture dimensions are 2.54 mm by 1.27 mm. However,

the printed dimensions are as much as 13% and 34% larger in the x and y directions, respectively. For the GRCop-84 waveguide, Fig. 3.9a, this creates an impedance mismatch to a standard flange which can be seen in return and insertion loss measurements. AlSi10Mg A3, Fig. 3.9d, which is created using a higher energy density has a rounded shape. In RF performance, this shape causes loss due to higher-order mode excitation at higher frequencies. The MCP and AlSi10Mg A2 components have the closest dimensions to the standard.

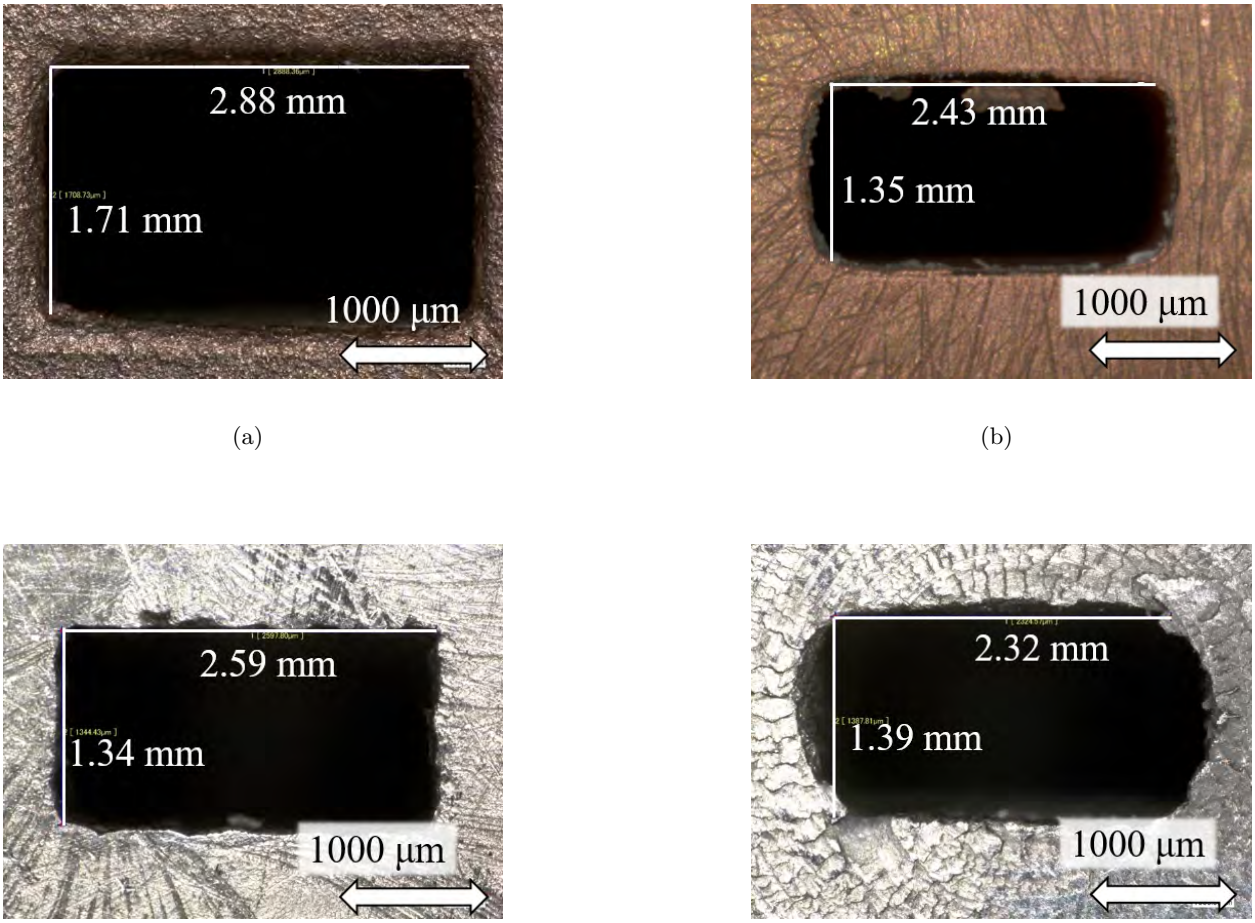

(a) (b)

(c) (d)

Figure 3.9: WR-10 aperture dimension deviation for (a) Cu, (b) MCP, (c) AlSi10Mg A2, and (d) AlSi10Mg A3 waveguide section. WR-10 aperture dimension for designed components is 2.54 mm by 1.27 mm.

3.2.4 Septum of Splitters

The asymmetry in the measured coupling $|s_{21}|$ and $|s_{31}|$ in Fig. 3.6b is analyzed by first comparing the actual fabricated geometry to the design of the junction shown in Fig. 2.9. An optical beam-splitter is used to couple green light into the waveguide port 1, and a camera is focused on the septum portion, resulting in the photo shown in Fig. 3.10. Although it is difficult to focus on all parts of the inner waveguide junction simultaneously, and some parts are not illuminated, it is evident from the photo that the waveguide junction shows a tilt asymmetry in the xy-plane. We believe that the tilt is due to the small dimension of the septum design (50 μm) which is close to twice the particle size of the fabrication process and exhibits a "balling" phenomenon [119]. A similar imperfection was seen in the W-band splitter, with an even larger effect due to more stringent dimensional needs.

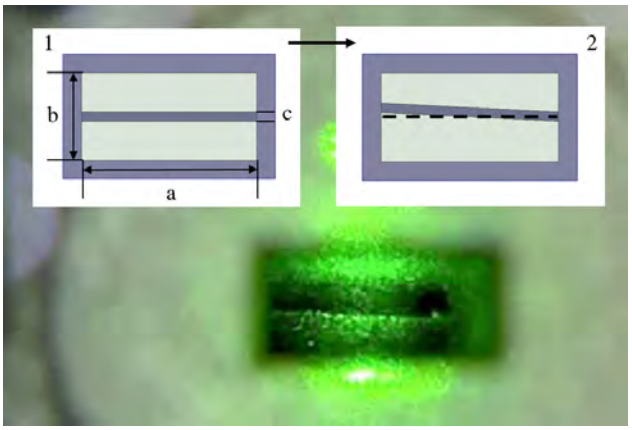

Figure 3.10: Photograph of the WR-15 waveguide junction. The dimensions shown in inset 1 are (a) 3.76 mm, (b) 1.88 mm, and (c) 0.05 mm (designed bifurcation width). Inset 2 shows the simulated asymmetry with a linear slope of 3%.

From the photograph, the tilt is estimated to be 0.15 mm at the waveguide edge, which corresponds to a 3.9% slope. The geometry shown in the second inset of Fig. 3.10 is simulated in HFSS and the results are shown in Fig. 3.11 for the 50-75 GHz band and compared to a perfectly symmetrical junction. Both 1% and 3% slopes result in asymmetry in the coupling, to a varying degree.

Although the walls are again assumed to be smooth in the simulation, and the tilt is assumed to be linear, these results explain the measured asymmetry in the coupling coefficients seen in Fig. 3.6b.

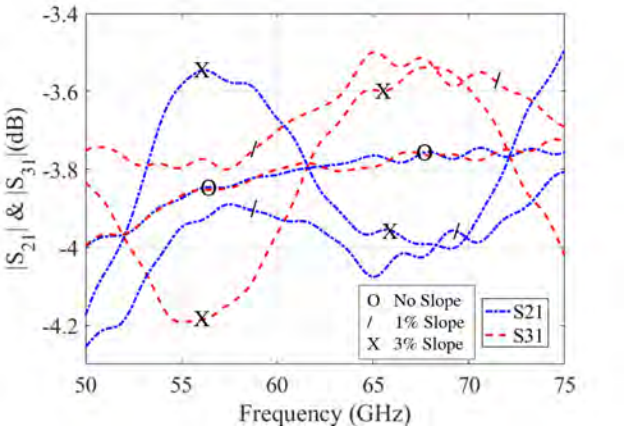

Figure 3.11: Simulation of linearly sloped asymmetries in the bifurcation for the WR-15 waveguide splitter compared to the ideal junction geometry (circular symbol. Both 1% (slash symbol) and 3% (cross symbol) show asymmetries similar to the measured coupling coefficients in Fig. 5. The walls of the waveguide are assumed to be perfectly smooth with a conductivity for maraging steel.

3.3 Surface Roughness Analysis

Surface roughness and realizable fabrication resolution are the primary limitations in AM millimeter-wave waveguide assemblies [120, 121]. Fabrication feature resolution was discussed in section II.B; this section focuses on surface roughness characterization. In [122], the spatial bandwidth limitations of FVM, an optical surface finish measurement technique, are analyzed and a measurement protocol is introduced to greatly reduce errors in the technique. The technique described in [122] is used in this work to characterize the surface finish of the AM waveguide components.

Shown in Fig. 3.12 are the FVM composite photographs of the waveguide interior surfaces taken during an FVM measurement. Fig. 3.13 shows the measured deviation in height of the interior of the WR-10 Cu (GRCop-84), WR-10 A3 AlSi10Mg, WR-15 AlSi10Mg, and WR-15 MS waveguides. The RMS surface roughness S_q and autocorrelation length S_{al} are typically used to characterize

the roughness of machined surfaces. The S_q value is a measure of the mean deviation of the height and the S_{al} value gives an idea of how the deviation is distributed laterally.

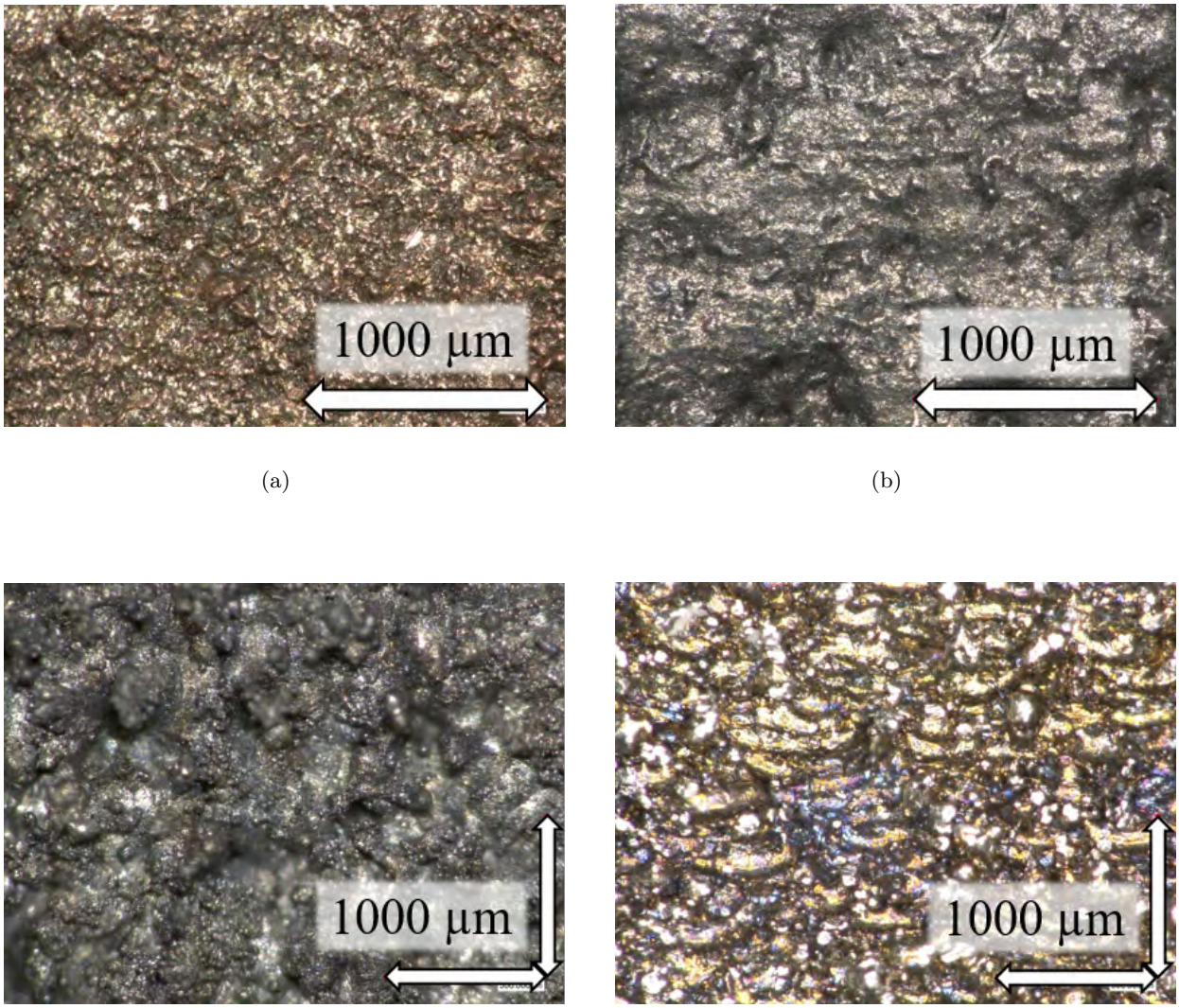

(a) (b)

(c) (d)

Figure 3.12: Composite images of (a) WR-10 GRCop-84, (b) WR-10 AlSi10Mg A3, (c) WR-15 AlSi10Mg, and (d) WR-15 MS straight waveguide section interior surfaces at x200 magnification.

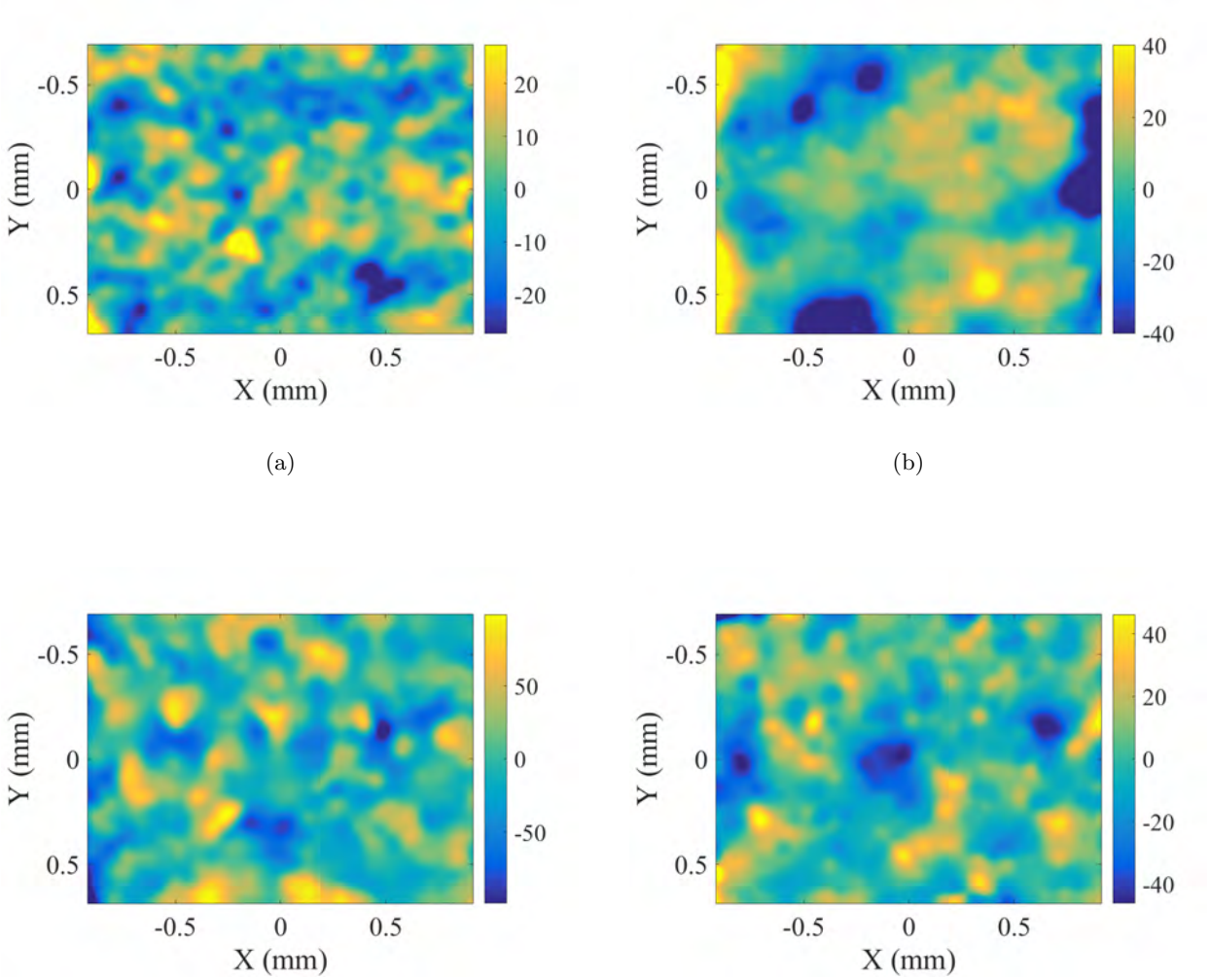

(a) (b)

(c) (d)

Figure 3.13: Measured (a) WR-10 GRCop-84, (b) WR-10 AlSi10Mg A3, (c) WR-15 AlSi10Mg, and (d) WR-15 MS straight waveguide sections topographical map with colormapped height deviation in μm.

In this work, common surface roughness measurement assumptions are made. First, the surface's autocovariance function (ACV) is isotropic and exponential and is modeled as:

$$ACV(\tau_x, \tau_y) = (S_q)^2 e^{-\tau/S_{al}} \tag{3.3}$$

where S_q is the RMS height variation and τ is the lag or displacement. The lag τ is defined as

$\tau = \sqrt{\tau_x^2 + \tau_y^2}$ where τ_x and τ_y are the 1D lag in the respective x and y directions.

The second assumption is that all height variations, S_q, follow a Gaussian distribution. Fig. 3.14 shows the measured comparison to these assumptions for WR-10 GRCop-84. Fig. 3.14 a shows an isotropic surface as the lag is homogeneous in the x and y directions. Fig. 3.14 b shows that the normalized surface height variation closely follows a Gaussian distribution. Because the protocol used in the FVM measurements depends on these assumptions to produce accurate results, it is useful to plot the normalized autocorrelation of the measured surface roughness profile, as in Fig. 3.15.

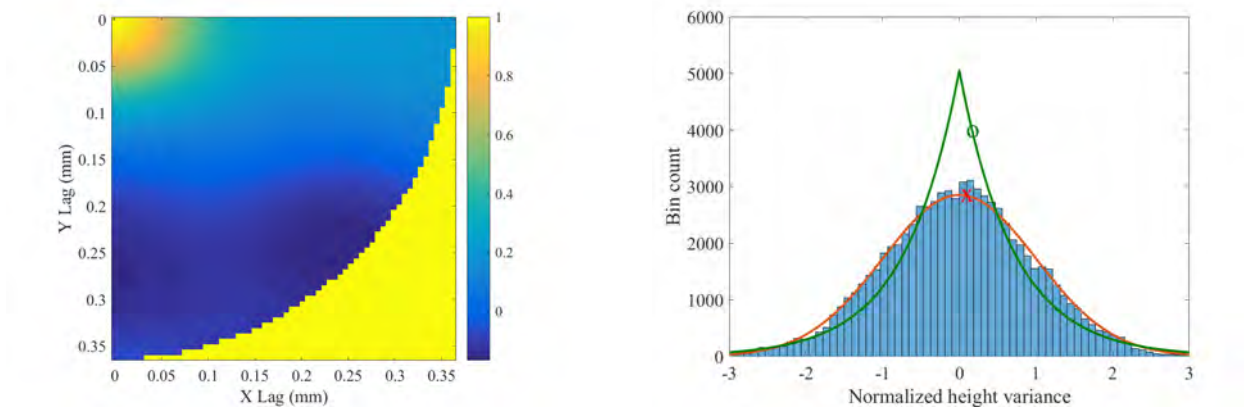

(a) (b)

Figure 3.14: (a) 2D array of calculated normalized autocorrelation as a function of τ (lag) in x and y directions from 0 to field-of-view (FOV) divided by 2π. (b) Histogram of normalized height variation with Gaussian (X-marker) and exponential (O-marker) curves. Both images use topographical data of the WR-10 GRCop-84 straight waveguide section interior surface at x200 magnification for computation.

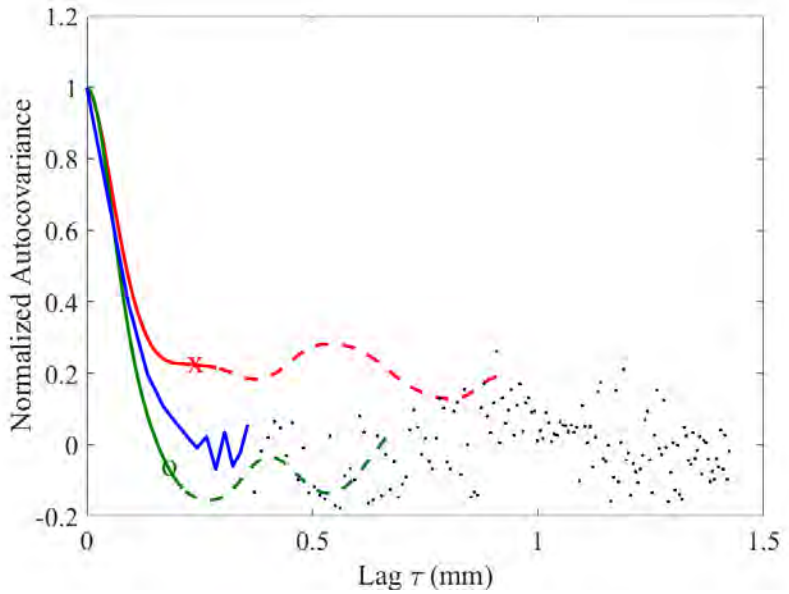

Figure 3.15: 1D computed normalized autocorrelation S_q (smooth line), for GRCop-84 from the image in Fig. 13a. Autocorrelation lengths in the horizontal (X-marker) and vertical (O-marker) directions show that computed S_q is a good fit to the ACV model before edge effects in the FOV limit affect accuracy.

With the isotropic and exponential behavior of the surface roughness of the fabricated waveguide confirmed, the autocorrelation or autocovariance and RMS surface roughness can accurately be measured. Table 3.5 shows the RMS height, autocorrelation length, and measured loss, α_m, for the various fabricated components. Surface roughness testing for the Ni alloy, Inconel 625, was not performed because the material is an extremely durable superalloy and successful destructive testing was not possible.

From a loss budget study, it is found that standard models do not accurately predict loss due to surface roughness for surfaces where the RMS height S_q is much larger than skin depth δ. In [89], a commonly used approximation for determining loss due to surface roughness takes the form:

$$C_{SR} = 1 + \frac{2}{\pi} \arctan\left(1.4 \left(\frac{\sigma}{\delta}\right)^2\right) \tag{3.4}$$

Table 3.5: Summary of AM Waveguide Surface Finish Characteristics at Center Frequencies (92.5 GHz and 62.5 GHz)

Fab.	Band	Material	S_q (μm)	S_{al} (μm)	α_m (dB/m)
3D Printed	W	AlSi10Mg A1	34.95	39.18	22.7
	W	AlSi10Mg A2	31.70	32.19	16.2
	W	AlSi10Mg A3	14.06	144.26	10.3
	W	MS	9.45	42.4	38.8
	W	GRCop-84	12.50	60.85	14.1
	W	Inconel 625	-	-	36.9
	W	Cu MCP	9.46	199.89	5.5
3D Printed	V	AlSi10Mg*	34.95	99.54	11.0
	V	MS	18.14	88.52	14.4
Machined	W	Silver**	-	-	3.54
	V	Silver**	-	-	1.97

* Using measurement after non-abrasive cleaning.
** Parts ST10R (W-band) and ST15R (V-band) from Custom Microwave, made using Coin Silver (90% Silver, 10% Copper)

where C_{SR} is a correction factor applied to the attenuation constant as: $\alpha_{rough} = \alpha_{smooth} C_{SR}$. It is seen that the predicted loss saturates at $2\alpha_{smooth}$ for WR-10 and WR-15 frequency ranges regardless of material. From the measured loss in Table 3.5, the WR-10 waveguide components shows the loss near $4\alpha_{smooth}$ (using $\delta_{Cu} = 0.215\,\mu$m at 92.5 GHz,$\sigma_{Cu} = 4.17\text{x}10^7$ S/m,), much higher than the predicted $2\alpha_{smooth}$. The WR-10 GRCop-84 waveguide aperture (in Fig. 3.9a) does not meet the standard WR-10 dimensions resulting in a standing wave in Fig. 3.16. The approximate surface roughness loss for GRCop-84 waveguide is calculated by subtracting the mismatch loss and conductor loss due to copper, from the measured $|S_{21}|$.

In addition, the measured data from WR-15 components does not agree with Eq. 3.4. In Fig. 3.2 and for maraging steel, the α_{smooth} at 62.5 GHz using measured conductivity is 8.0 dB/m where α_m is 14.4 dB/m. With the still saturated correction factor (using $\delta_{MS} = 1.406\,\mu$m at 62.5 GHz, $\sigma_{MS} = 2.05\text{x}10^6$ S/m), the predicted surface roughness is larger than measured; here, the α_m is equal to $1.8\alpha_{smooth}$. Eq. 3.4 is most common in commercial EM simulators, but the conclusion from the measurements in this paper is that it does not accurately predict loss at V and W bands for very

rough surfaces ($S_q \gg \delta$).

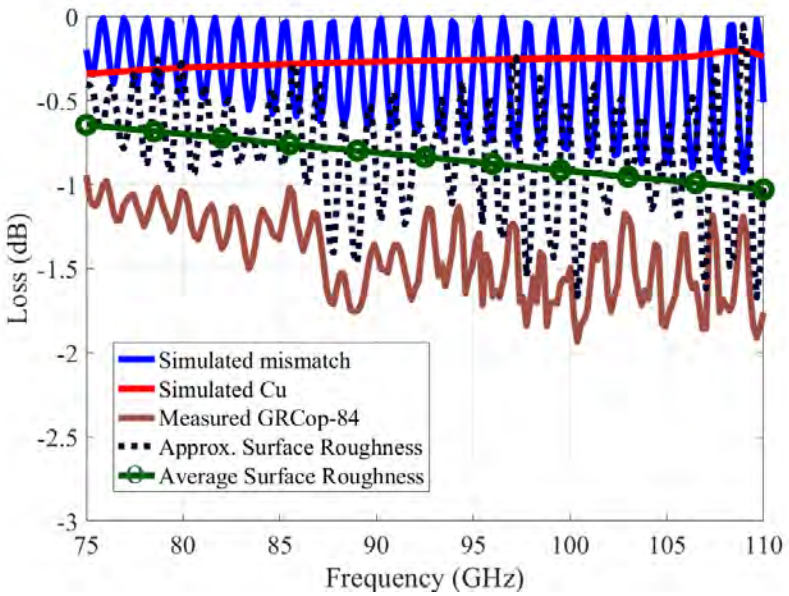

Figure 3.16: Different loss mechanisms for GRCop-84 AM waveguide. The surface roughness loss is approximated by subtracting simulated losses (mismatch from aperture dimension deviations and idealized Cu loss) from the measured S-parameter data. Average surface roughness loss (O-markers) is the moving average of the calculated approx. surface roughness loss.

3.4 Conclusions

Here, the designed waveguide structures from Chapter 2 were fabricated, measured, and analyzed for surface finish and feature resolution with respect to electrical performance and between two main alloys, AlMgSi10 and maraging steel. It is determined that there is a tradeoff between measured electrical conductivity and feature resolution, where maraging steel performs better with less surface roughness and higher printing repeatability at the cost of decreased conductivity.

An analysis of the printed surfaces is performed and the 3-dimensional RMS and autocorrelation values of the unprocessed surface roughness is determined. It is also determined that the highly used surface roughness models such as the Hammerstad model fails to accurately capture loss from

surface roughness as waveguide frequency increases. Most of these results are reported in [90] and [115].

For future work, it would be of interest to use the correlation function for the 3D roughness found in [90] with an extended version of the small perturbation method from Section 2.3.1 for directly correlating measured surface characteristics to waveguide power loss.

Chapter 4

Millimeter-Wave Metal Waveguide-to-MMIC Transitions

Contents

In the previous two Chapters 2 and 3 metal rectangular waveguides are discussed. In tightly integrated front-end packages, an interface needs to exist so that the TE_{10} dominant mode impedance in rectangular waveguide is matched to the MMIC microstrip impedance. Particularly, the waveguide impedance is dispersive and ranges from between 628-450 Ω between 75 and 110 GHz for air-filled WR-10 waveguide, while the MMIC input and output microstrip impedance is approximately 50 Ω and constant across the band. The key to this conversion interface is impedance matching through a three-dimensional structure.

4.1 Integration Types and Needs

A review of millimeter-wave waveguide transitions with various techniques is presented in [123–127] and the main designs of those references are conventional E-plane microstrip-to-waveguide transitions covering the entire W-band. In [126], transitions with a built-in dc/IF return path are designed and fabricated for both 75-110 GHz and 180-260 GHz bands, in which a traditional E-plane probe is directly connected to the backshort by a thin metal wire along the axis of the waveguide; shown in Fig. 4.1a. In [128], an iris coupling transition is designed on a single layer substrate in a a cavity that feeds into waveguide; shown in Fig. 4.1b. Proof of concept was shown from 43-47 GHz in Alumina, from 88-100 GHz on z-cut quartz, and from 87-100 GHz on fused silica. All exhibited better than 22-dB return loss at their center frequencies with less than 0.3-dB insertion loss, and at minimum a 10% 15-dB return-loss bandwidth. In [129] an inline transition between microstrip and rectangular waveguide with an intermediate step through dielectric filled rectangular waveguide; shown in Fig. 4.1c. This transition shows a return loss greater than 10 dB and mean insertion loss lower than 1 dB.

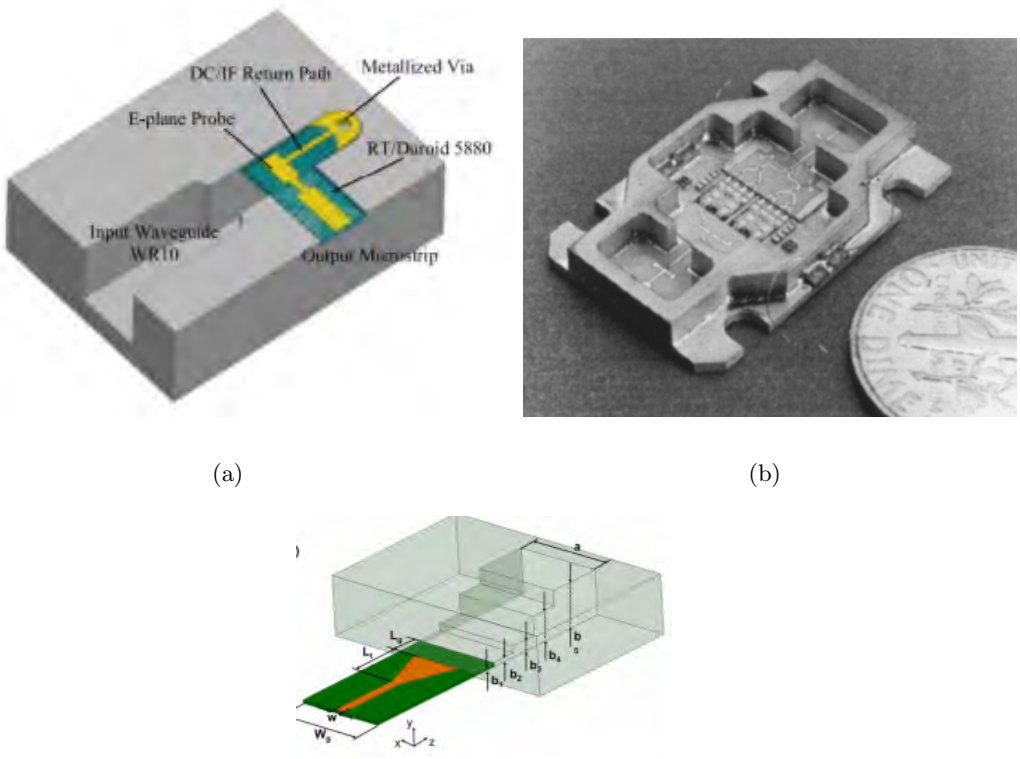

(a) (b)

(c)

Figure 4.1: Images of designed mm-wave transitions from contemporary literature: (a) [126], (b) [128], and (c) [129].

4.2 MMIC Modules

Fig. 4.2 shows a diagram of a W-band module comprised of a packaged power amplifier with dc biasing, microstrip-to-waveguide transitions, and WR-10 waveguide.

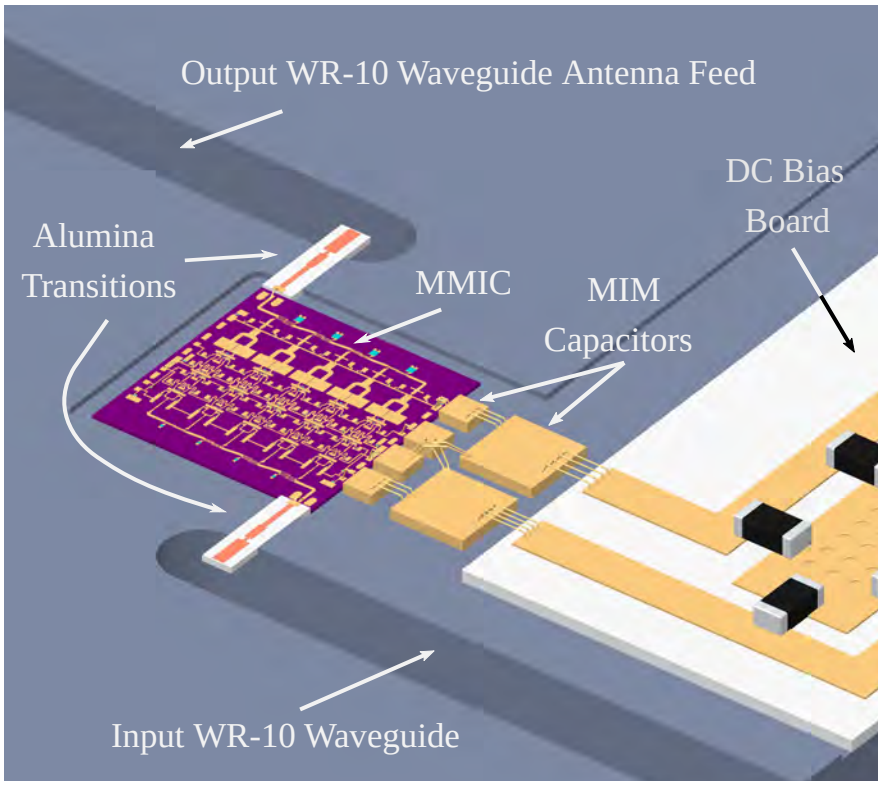

Figure 4.2: Image of W-band MMIC PAs with bias circuit, microstrip-to waveguide alumina transitions and input/output WR-10 waveguides.

The MMIC die is placed/attached in a metallic cavity for two reasons: good conductive ground and a good thermal junction. For mounting and testing in the power amplifier work presented in the next chapters (5, 6, 7, and 8), EPOTEK H20S conductive epoxy is used. This epoxy has a high thermal conductivity of 3.3 W/mK and a low volume resisitivity of less than 0.00005 Ω-cm.

Simple power amplifiers require two different voltage paths, one for RF and one for dc. The complexity can vary for both, but simply there are routing requirements for an RF input and output and at least two different voltage levels (gate and drain) applied to the transistors in a MMIC. For the dc path, concerns for power amplifier stability must be taken into account. This means that power supply transients and feedback paths must be shorted in lowpass filter networks. Here, we add 'capacitor ladders' external to the MMIC with increasing capacitor size. The capacitors used on the MMIC mountings in this thesis are bondable components from American Technical Ceramics

of 100 pF and 1000 pF, sized as 0.38×0.38 mm and 1.27×1.27 mm respectively. Images of various die mountings are seen in Fig. 4.3 with these capacitor networks bonded to them.

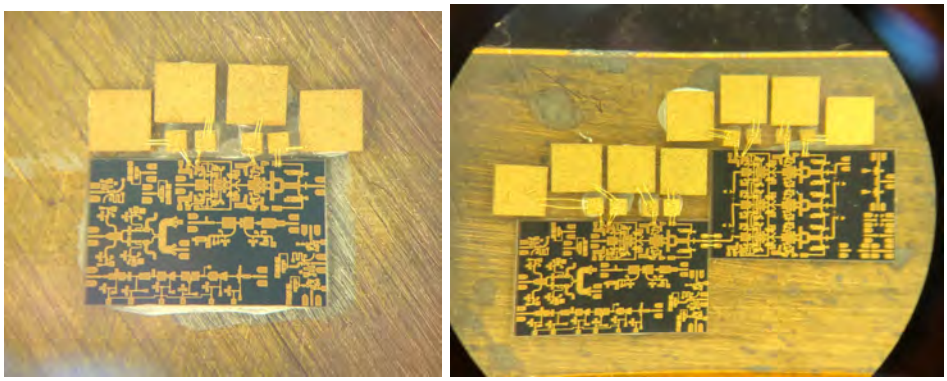

(a) (b)

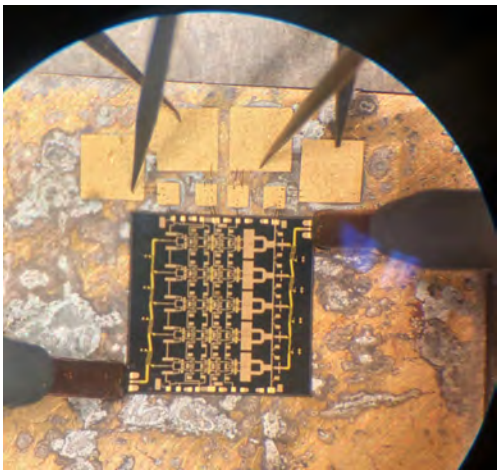

(c)

Figure 4.3: Microscope photographs of different mounted dies with power amplifiers (results shown in other Chapters). In (a), a single die shows an off-chip capacitor ladder network using bondable capacitors. In (b), two die are mounted tightly together for minimal loss from the bonded RF connection. In (c), a mounted die is tested on a probe station.

Concerning the RF path, MMIC-to-waveguide transitions need to maintain low loss transmission. This means that any transition must be mounted in a similar fashion to the MMIC with most concern placed on alignment, physical stability, and having a highly conductive ground connection.

For MMICs designed in the next Chapters, transitions were designed to convert microstrip

modes on MMICs to the WR-10 waveguide TE_{10} mode across all frequencies in W-band. First, a design implemented in Alumina is seen in the simulation model of Fig. 4.5, [42]. Second, a design implemented in a in a 100 μm GaAs-on-Si process from WiN Semiconductors is seen in the simulation model of Fig. 4.8. For both transitions, waveport 1 excites WR10 waveguide, while waveport 2 excites a 50 Ω microstrip on the MMIC. The split-block configurations are seen in Figs. 4.4 and 4.7.

4.3 Alumina Designs for W-band

An E-plane probe transition is designed and EM simulated in Ansys HFSS on a polished 100 μm Alumina substrate with a top and bottom 5 μm thick copper metal layer, seen as a detailed diagram in Fig. 4.5 . On the top side, a rectangular probe radiates into the WR-10 cavity with a back-short at $\lambda_g/4$ which is rounded due to CNC machining. A stepped-impedance microstrip line is used for matching from a capacitive load to a 50-Ω line on Alumina that ends in a gold pad for a more reproducible bond-wire MMIC to transition interconnect. On the bottom side, the metal is not deposited underneath the rectangular probe and is only underneath the matching networks and 50-Ω line. Widths A, B, C, and D are 80 μm, 130 μm, 50 μm, and 200 μm respectively.

Using finite element EM analysis in ANSYS HFSS, the nominal design shows in Fig. 4.6 less than 1 dB of insertion loss across W-band. In [42], this design was created without bondwires in mind; and including the bondwire caused slight degredation in performance (S_{21} (drops roughly 0.5 dB and has an in-band ripple).

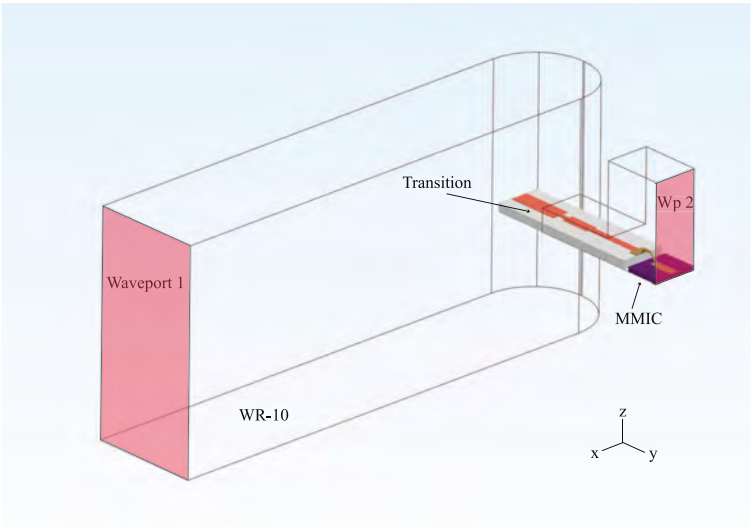

Figure 4.4: A detailed diagram from an isometric view of the designed Alumina transition bonded to a MMIC with labels describing important design areas.

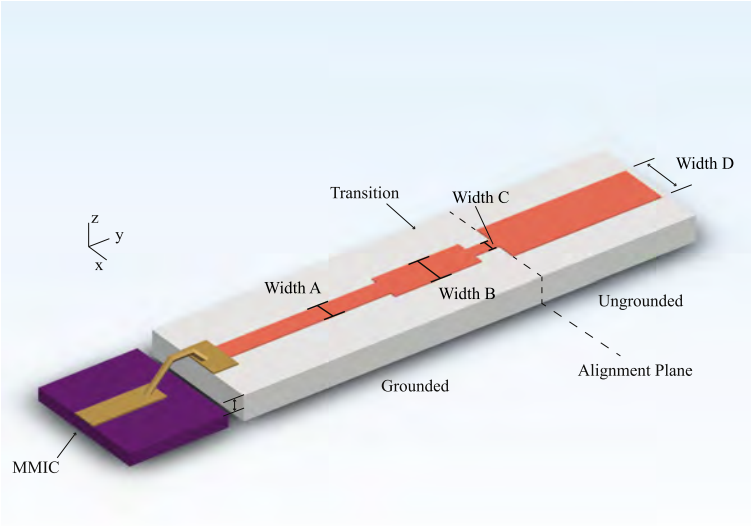

Figure 4.5: A close-up diagram from an isometric view of the designed Alumina transistion bonded to a MMIC with labels describing important design areas.

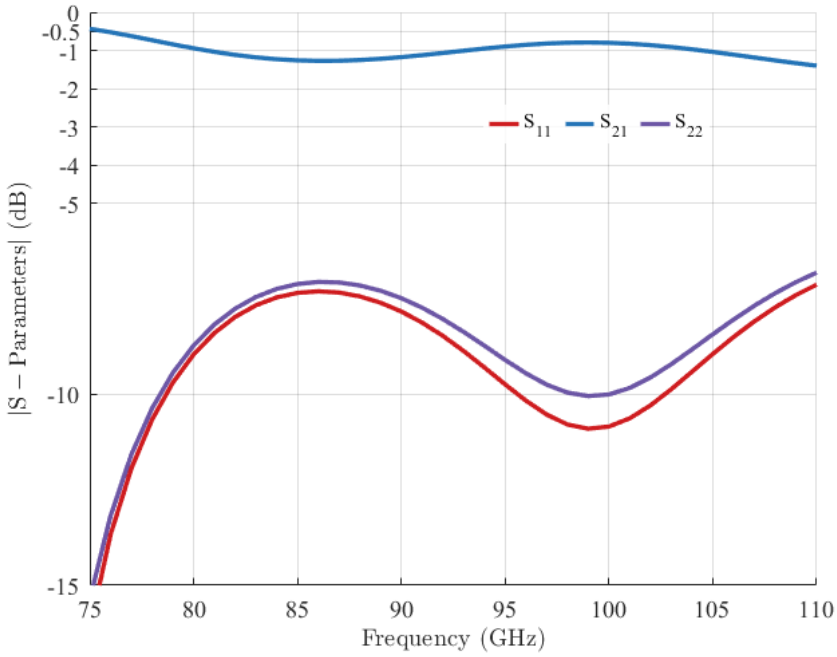

Figure 4.6: The S-parameters of the Alumina transition showing roughly 1 dB of insertion loss across W-band and below 8 dB of return loss.

4.4 GaAs Design for W-band

Several foundries offer processes for passive-only devices that include vias and complex backside processing which are more difficult to make in Alumina. An E-plane probe transition is designed and EM simulated in Ansys HFSS in a 100 μm GaAs-on-Si process from WiN Semiconductors with a top and bottom 3.1 μm thick metal layer, seen as a detailed diagram in Fig. 4.7. The transition is bonded to the RF connection in the GaN HRL T3 process ground-signal-ground (GSG) structure and the other end of the transition excites the WR-10 TE_{10}. This design is most similar to the transition described in [123].

On the top side, a rectangular probe radiates into the WR-10 cavity with a back-short at $\lambda_g/4$ which is rounded due to CNC machining. On the top side, seen as a detailed diagram in Fig. 4.8a, a smoothly stepped-impedance grounded microstrip to ungrounded microstrip line is

used for matching from a capacitive load to a 50-Ω line at 92.5 GHz. Widths A, B, and C are 40 μm, 25 μm, and 110 μm, respectively. On the bottom side, seen as a detailed diagram in Fig. 4.8b, the metal is not deposited underneath the rectangular probe and is only underneath the 50-Ω line and some of the line of width B. The width D and length D are 300 μm and 150 μm. A small cavity in the split-block, to reduce waveguide aperture coupling, is inline with the rounded dimensions of the width and length D area on the ungrounded region of the transition.

The nominal design shows in Fig. 4.9 roughly 0.5 dB of insertion loss across W-band. The bondwire and the GaN MMIC are considered in the analysis. Fig. 4.10 shows an isometric view of a simulation solution's electric field magnitudes at 92.5 GHz. This shows that the quasi-TEM mode converts effectively into the TE_{10}.

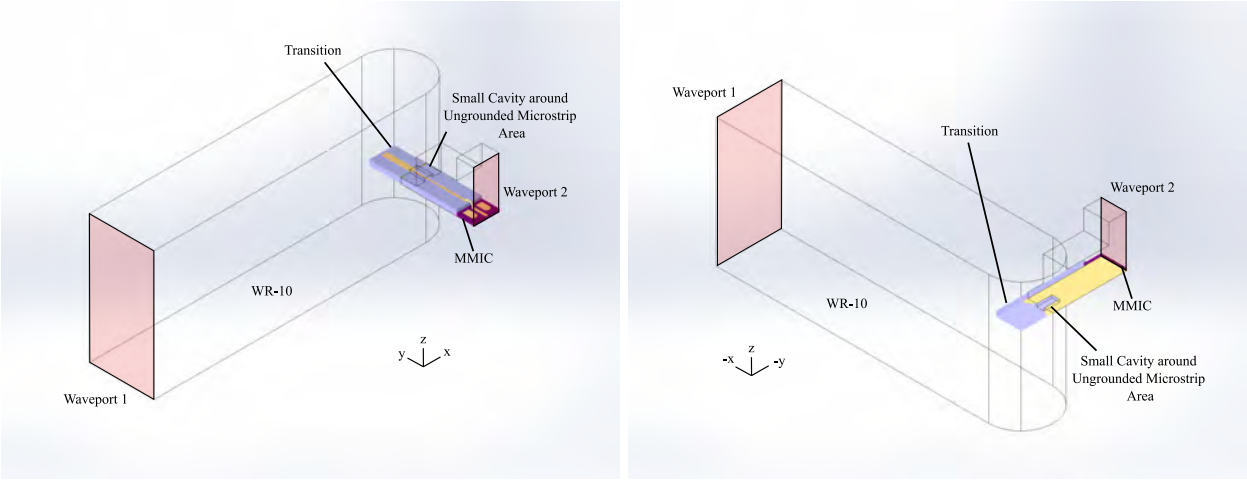

(a) (b)

Figure 4.7: A diagram of the designed GaAs transistion bonded to an HRL GaN MMIC 100 μm ground-signal-ground (GSG) structure mounted in a cavity and positioned in WR-10 for (a) top and (b) bottom isometric views with labels describing important design areas.

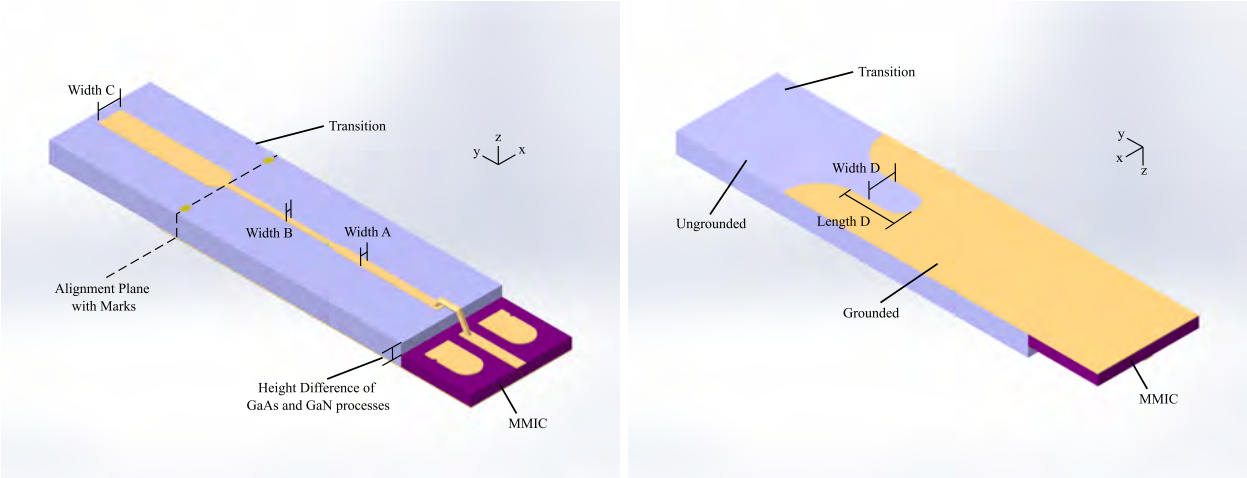

(a) (b)

Figure 4.8: A close-up diagram of the designed GaAs transistion bonded to the HRL GaN MMIC 100 μm GSG structure for (a) top and (b) bottom isometric views with labels describing important design areas.

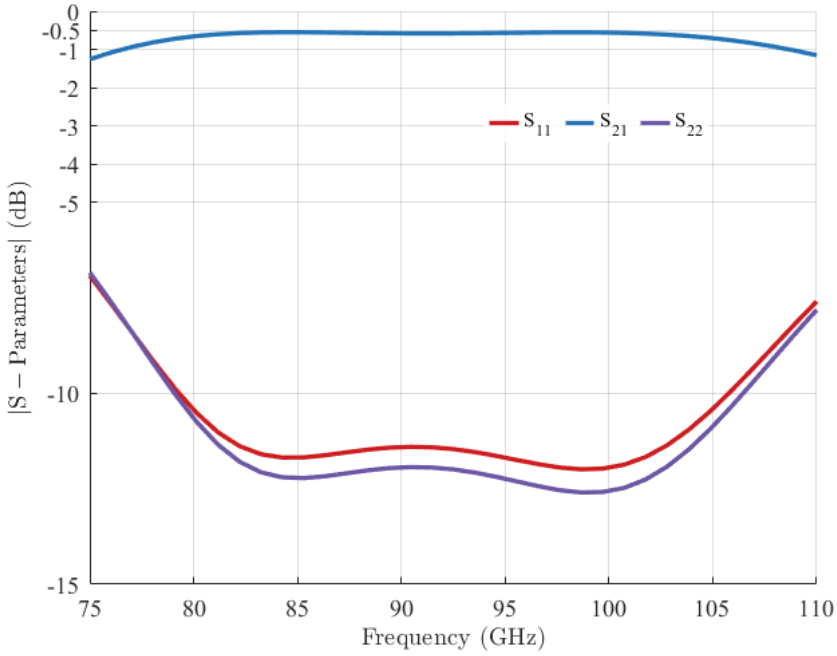

Figure 4.9: The S-parameters of the GaAs transition showing roughly 0.5 dB of insertion loss and below 10 dB of return loss for most of the W-band.

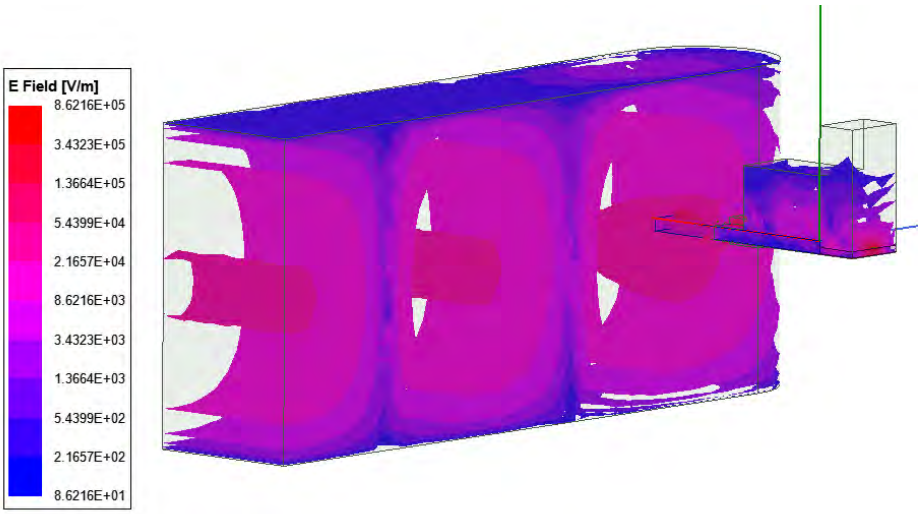

Figure 4.10: An image of the magnitude of the electric field at 92.5 GHz showing the effective mode transformation from microstrip on the MMIC to TE_{10} in the waveguide.

4.5 Conclusions

In this chapter, two E-plane probes are designed to cover all frequencies in W-band as well as transition from 50 Ω lines on MMIC PAs to TE_{10} mode in a WR-10 metal rectangular waveguide. The first design is implemented in a 100 μm Alumina process with stepped impedance sections and presents roughly 1 dB of insertion loss. The second design is implemented in a MMIC on a 100 μm GaAs process by WiN Semiconductors with smoothed impedance sections and presents roughly 0.5 dB of insertion loss.

Chapter 5

W-band 3-Stage PA Design and Staging Analysis

Contents

In this chapter, device scaling and reactive power-combing are shown on designs of 3-stage W-band PAs illustrated in Fig. 5.1 (a) and (b).

State-of-the-art published results for W-band GaN power amplifiers are summarized in Table 5.1. Power levels as high as 37 dBm with 18.3% efficiency are reported over a narrow 7% bandwidth at 95 GHz in a 100-nm process [130]. On the other hand, a 44% bandwidth from 70-110 GHz with 26 dBm peak power and a gain of 16±2 dB is shown in [131]. In this chapter we demonstrate a 37.8% bandwidth from 75 to 110 GHz (where gain greater than 15 dB), a peak power of 27 dBm and a peak gain of 23 dB. In order to show power scaling, we designed several PAs with power

combining at different levels, and progressively increased circuit complexity (Fig. 5.1). First, the device periphery is scaled in the output stage while 3 stages are introduced for sufficient gain with reactive combining of the saturated output stage. Second, to further increase power, two 3-stage reactively-combined PAs are integrated in a balanced MMIC PA. Finally, three 3-stage PAs are serially combined, as in [53, 132].

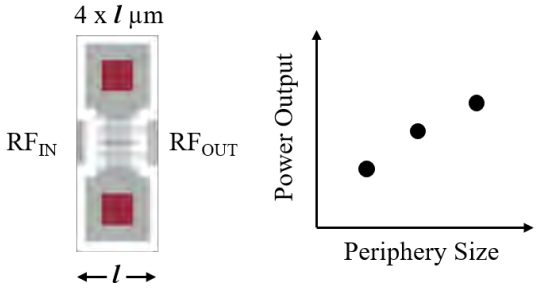

(a)

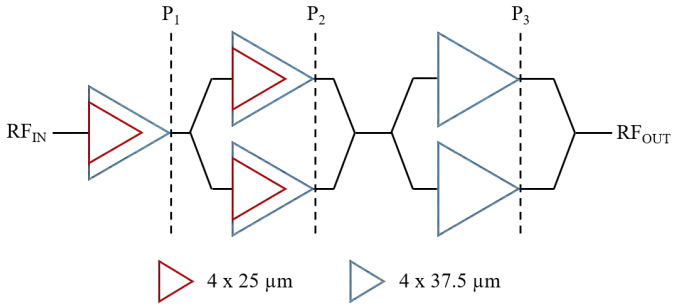

(b)

Figure 5.1: Schematics of power amplifier (PA) topologies with increasing levels of power combining demonstrated in this chapter. (a) Device scaling, where total area is proportional to power output. (b) Two three-stage PAs with power combining in stages 2 and 3, and different staging ratios, with peripheries shown in red/blue.

Table 5.1: Comparison of W-band GaN HEMT Amplifiers

Freq (GHz)	Frac. BW (%)	P_{out} (dBm)	PAE (%)	Gain (dB)	Year Ref.
84-95	12.3%	29.2 dBm	14.7%	19.6 dB	2010 [133]
90-92	2.2%	32.3 dBm	11%	15 dB	2011 [134]
70-105	40%	24.5 dBm	6%	16 dB	2012 [44]
80-100	22.2%	35 dBm	-	8 dB	2013 [135]
77.8-89	13.4%	31 dBm	12.3%	17 dB	2016 [136]
75-110	37.8%	33 dBm	-	15 dB	2016 [137]
86–94	8.8%	30.6 dBm	8%	12 dB	2017 [138]
88-93	5.5%	34 dBm	14%	15 dB	2017 [139]
70-110	44.4%	28.6 dBm	6.5%	12 dB	2018 [131]
90-97	7.5%	37.8 dBm	18.3%	15 dB	2020 [130]
75-110	**37.8%**	**20 dBm**	**8 %**	**11 dB**	**Chapter 5***
75-110	**37.8%**	**25 dBm**	**9.6 %**	**15 dB**	**Chapter 6^{+}**
75-110	**37.8%**	**27 dBm**	**3 %**	**23 dB**	**Chapter 6‘**

* Unit-B Amplifier - @ $P_{IN} = 9\,\text{dBm}$ and $86\,\text{GHz}$

+ Balanced - @ $P_{IN} = 10\,\text{dBm}$ and $76\,\text{GHz}$

‘ Driver + Serial - @ $P_{IN} = 4\,\text{dBm}$ and $90\,\text{GHz}$

5.1 Periphery Scaling in W-band GaN

The PA designs presented in this chapter are implemented in the HRL T3 40-nm GaN-on-SiC process, well documented in [40, 44–52]. A variety of W-band circuits have been demonstrated in this process, e.g. switches, low-noise amplifiers, mixers, and phase shifters [140, 141]. Recent work with bare die transistors heterogenously mounted with matching networks also shows W-band PA performance [142]. In the current T3 process, transistor scaling achieves an f_T/f_{max} of 200/400 GHz with a breakdown voltage greater than 40 V. The passives use three metallization layers to form transmission lines and air bridges. Capacitors are formed with silicon nitride (SiN) and resistors are formed with tantalum nitride (TaN). The actives and passives are processed on a 50 μm substrate.

This advanced GaN process is under development, and this chapter shows results from MMICs fabricated in two different runs as summarized in Table 5.2. In Run 2, a processing issue resulted in high current collapse [143], lower g_m and lower I_{max}, resulting in about 4 dB lower gain and lower output power than predicted by nonlinear models.

Table 5.2: Summary of Fabricated PAs

Run #	Architecture	Total Periphery (mm)	Staging Ratio
1	Unit A	0.60	1:2:3
	Balanced	1.20	1:2:3
2	Unit B	0.75	1:2:2
	Serial	2.25	1:2:2
	Driver + Serial	3.00	1:2:2

To evaluate output power versus periphery scaling, data for validated and extrapolated device sizes are used. Non-linear Angelov models for 4×37.5 μm, 2×25 μm, 6×50 μm, and 12×50 μm transistors are validated at drain voltages of +2 V, +6 V, and +12 V with quiescent drain currents of 150 mA/mm, respectively. Due to the limited availability of millimeter-wave load-pull mea-

surements for non-linear device modeling, typical models are extrapolated from lower frequency load-pull measurements around a certain quiescent bias point and for a specific periphery [**?**]. This implies that model validity is reduced when deviating from validated periphery and bias conditions, e.g. for the 4×25 μm device. Fig. 5.2 shows the power scaling with periphery, at a constant quiescent point and across the W-band range. Note that the gain is in the 3-4 dB range for all device models at maximum output power, requiring multiple stages in a PA design to achieve reasonable saturated gain.

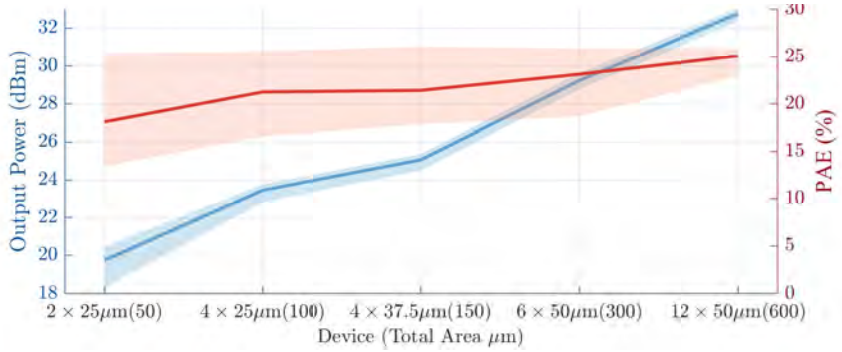

Figure 5.2: Plot of the maximum power output and corresponding efficiency with optimal impedances presented to the device input (match below -10 dB) and output (obtained by load-pull). The shaded area presents behavior across frequency from 75 to 110 GHz for each validated HEMT model, and for an extrapolated 4×25 μm HEMT model. All devices are biased at V_{DD}=12 V and V_{GG}=-0.2 V, and the compressed gain is in the range of 3-4 dB.

Fig. 5.3 shows simulated load-pull values for 4×25 μm and 4×37.5 μm devices with an input power of +17 dBm, biased at +12 V and a quiescent current of 200 mA/mm. The initial load-pull characterization at 75, 92.5, and 110 GHz is simulated by presenting a constant source impedance of $0.8\angle 181.2°$, found from an initial source-pull simulation. The resulting load-pull contours display a desired load trajectory over frequency for a peak PAE of 30 % at 75 GHz, 25 % at 92.5 GHz, and 19 % at 110 GHz. Using these peak values, a final source-pull shows an optimal source impedance region for matching the full W-band range for both devices sizes.

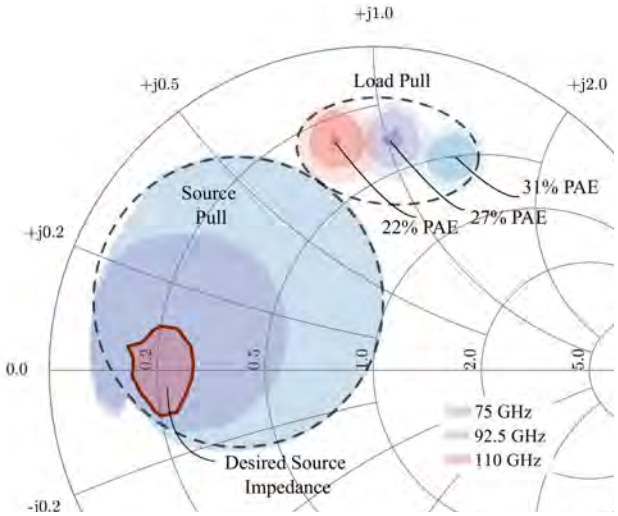

(a)

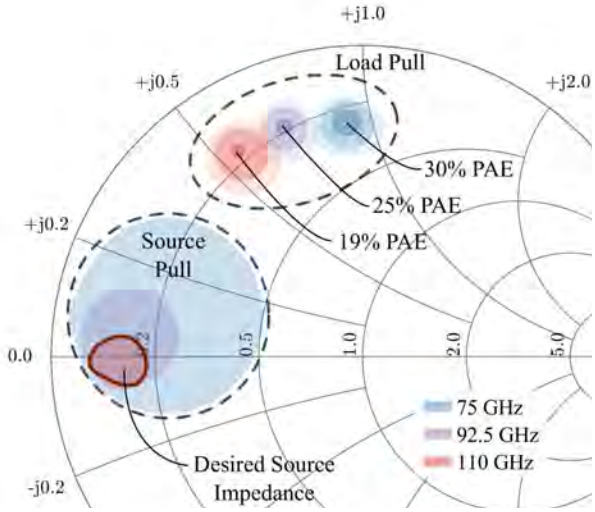

(b)

Figure 5.3: Load-pull PAE contours at 75, 92.5, and 110 GHz for (a) $4 \times 25\,\mu$m and (b) $4 \times 37.5\,\mu$m HEMT with an input power of 17 dBm and biased at 12 V with 30 mA quiescent. For high efficiency operation in the full W-band range, a fundamental load trajectory over frequency should reach each maximum PAE contour. The load pull contours are in steps of 1 %. Source-pull data shows the region corresponding to high PAE across W band.

In the 3-stage PA designs, the impedance trajectories deviate from the optimized ones shown

in Fig. 5.3, resulting in reduced power and PAE. We define a staging efficiency for m stages as:

$$\eta_{\mathrm{Sm}} = \frac{P_{IN}}{n_m \cdot P_{MAX,m}} \prod_{i=1}^{m} G_i \tag{5.1}$$

where P_{IN} is input power, G_i are the gains of each stage, n_m is the number of devices in stage m, and $P_{MAX,m}$ is the largest output power of a device in stage m. The design of a 3-stage MMIC PA is next presented, and the staging efficiencies evaluated.

5.2 Three-Stage PA with Reactive Combining

The 3-stage PAs (Fig. 1b), which we refer to as 'Unit-A' and 'Unit-B', are a 2-way power combined topology; Fig. 5.4 shows the layout of Unit-B. The output stage utilizes two $4\times37.5\,\mu$m devices in parallel to provide a total output periphery of $300\,\mu$m. Two staging ratios are implemented: 1:2:3 (Unit-A) and 1:2:2 (Unit-B), both to efficiently saturate the third stage, while providing a comparison for staging efficiency. The Unit-B PA uses only validated transistor models, and is larger by 25% in periphery at $750\,\mu$m. The bias conditions are kept slightly above the validated quiescent current to operate in class-AB. For stages 1, 2, and 3, the drain currents correspond to 30 mA, 60 mA, and 60 mA, respectively.

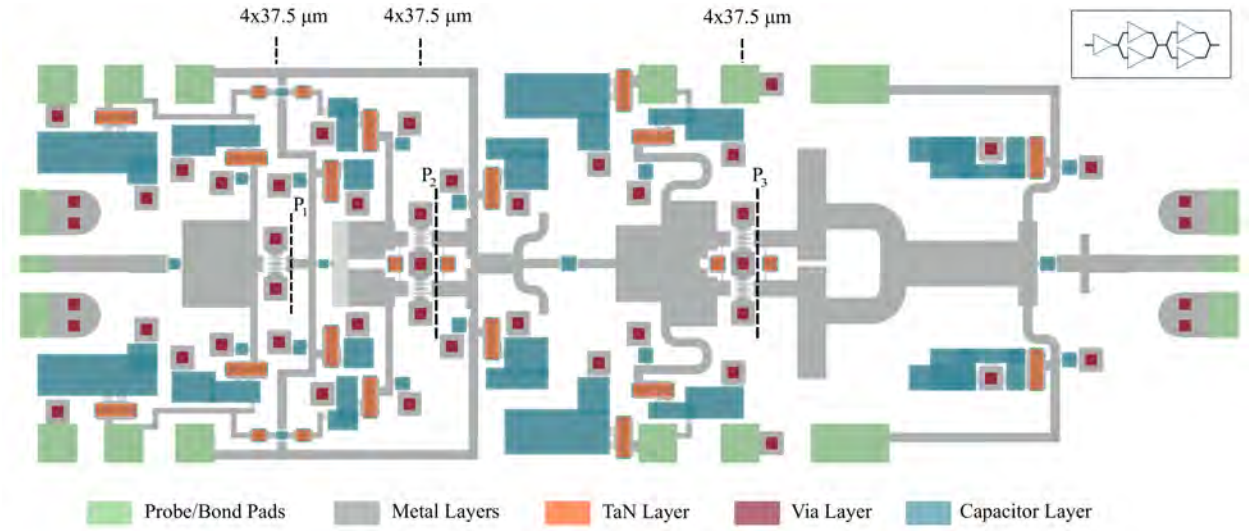

Figure 5.4: The layout of the 3-stage MMIC PA. The staging ratio is 1:2:2, and the peripheries for stages 1, 2, and 3 are 150 μm, 300 μm, and 300 μm, respectively. The die area is $3.13 \times 1.02\,\text{mm}^2$. For clarity, some metal layers and proprietary transistor layers have been removed.

5.2.1 PA Design and Simulation

Since the process does not allow capacitors over vias, low-impedance transmission lines and stubs are used for low-Q, broadband matching in the input, interstage, and output networks. In the low-impedance sections of microstrip lines, it is important to minimize current imbalances across the entire frequency range and to ensure that only the microstrip current mode exists, as detailed in [42]. Parallelizing with internally shared vias reduces the distance between transistors. The design also uses SiN capacitors with external slot vias for dc blocking and bypassing.

Because transistors in millimeter-wave processes have high gains at lower frequencies, stability needs to be carefully analyzed. Multiple stability analysis methods are performed during the design: K factor, internal Nyquist stability, and loop gain [144, 145], as described in [42]. The resulting even-mode loop gain simulations of the Unit PAs show a phase margin greater than 60°, seen in Fig. 5.5. Suppression of low-frequency gain is accomplished through accurate full-wave simulations of reactive matching networks, the addition of small resistors (about 5 Ω) in the dc gate paths,

and on-chip capacitor ladder networks with increasing capacitor size from the RF path to the dc inputs. To eliminate odd-mode instabilities, resistors are placed on the symmetry lines before and after transistors in stages 2 and 3 and minimized in value using odd-mode loop-gain simulations.

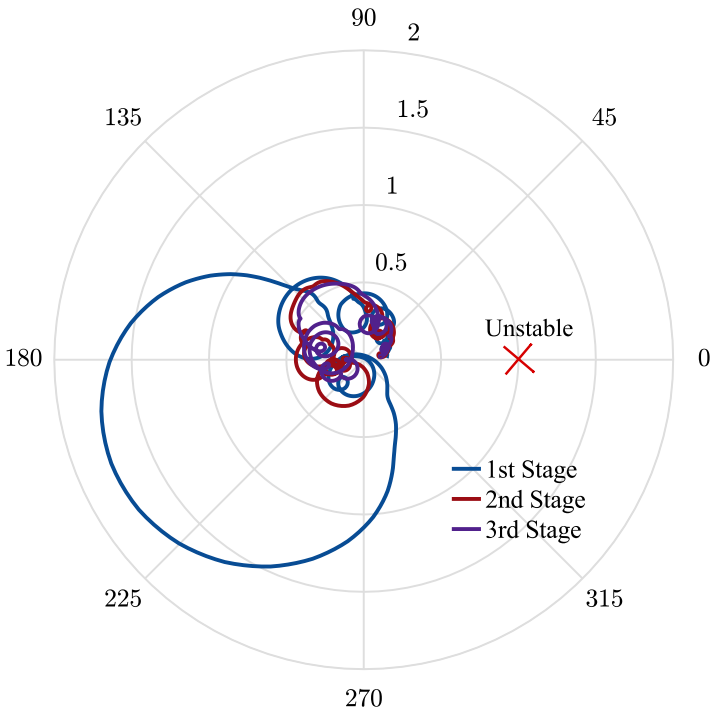

Figure 5.5: A polar plot of the even-mode loop gain for the Unit-B power amplifier with greater than 60° phase margin.

Figs. 5.6a and 5.7a show the small-signal wideband frequency response of $|S_{21}|$, $|S_{11}|$, and $|S_{22}|$ for the Unit-A and Unit-B PAs from 0.1 to 330 GHz. Sufficient low-frequency gain suppression with the minimum of approximately 5 dB at 30 GHz provides stability up to the third harmonic. For small-signal simulations (Figs. 5.6a and 5.7a), +6 V and +12 V drain bias voltages are considered, with a quiescent bias current in class-AB, $I_{\mathrm{dq}} = 200\,\mathrm{mA/mm}$. For +12 V, the simulations show small-signal gain greater than 15 dB across W-band. The simulated large-signal performance is shown in Figs. 5.6b and 5.7b at a bias point of +12 V and 200 mA/mm. The simulations predict an

output power greater than 25 dBm over 75 to 110 GHz. Over the entire W-band, a minimum PAE of 8 % is maintained. A large-signal gain of greater than 12 dB is predicted over 75 to 110 GHz.

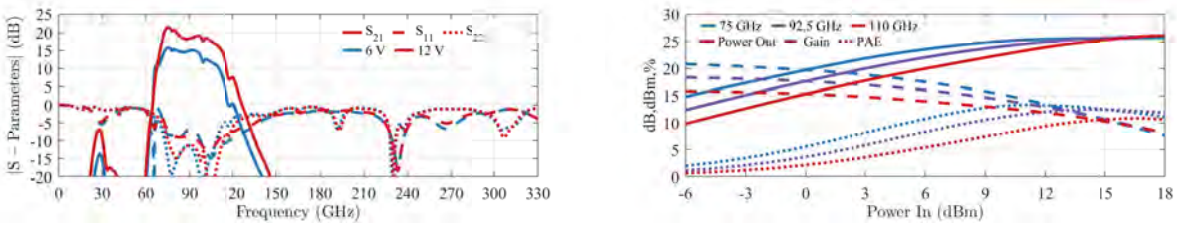

(a) (b)

Figure 5.6: (a) Small-signal simulated performance of the 3-stage Unit-A PA from 0.1 to 330 GHz at V_{DD} = +6 V (blue) and +12 V (red). (b) Simulated large-signal characteristics over a power input sweep at 75 (blue), 92.5 (purple), and 110 GHz (red).

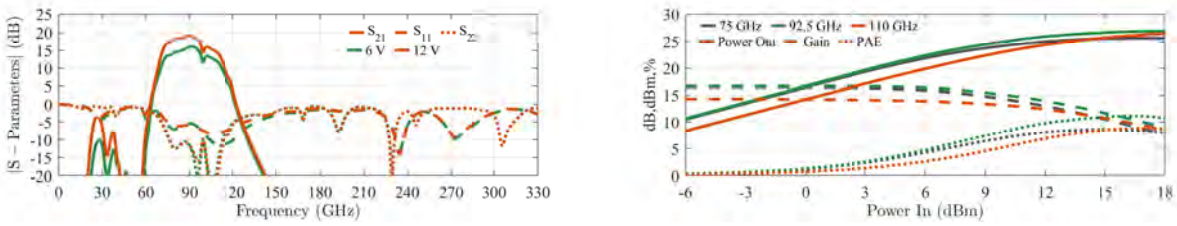

(a) (b)

Figure 5.7: (a) Small-signal simulated performance of the 3-stage Unit-B PA from 0.1 to 330 GHz at V_{DD} = +6 V (blue) and +12 V (red). (b) Simulated large-signal characteristics over a power input sweep at 75 (blue), 92.5 (purple), and 110 GHz (red).

Fig. 5.8 shows the output impedance of the three stages for both 3-stage PA designs. It is interesting to notice that the 3rd stage changes the least with compression. The first-stage impedance changes the most at lowest frequencies, and therefore has a significant impact on the staging efficiency. The source impedance shown in Fig. 5.9 remains approximately constant across power, and is within the desired regions of Fig. 5.3.

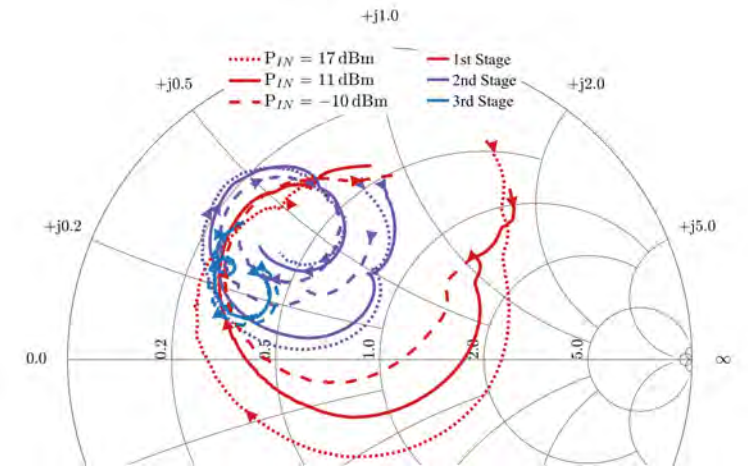

(a)

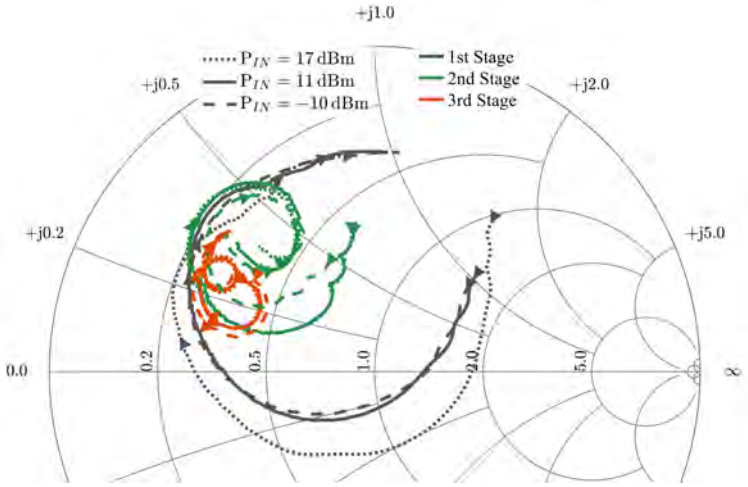

(b)

Figure 5.8: Reflection coefficient trajectories from 75 to 110 GHz (directive as the arrows on the smith chart) for the output of the transistors on the 1st, 2nd, and 3rd stages of (a) Unit-A and (b) Unit-B PAs at different input power levels.

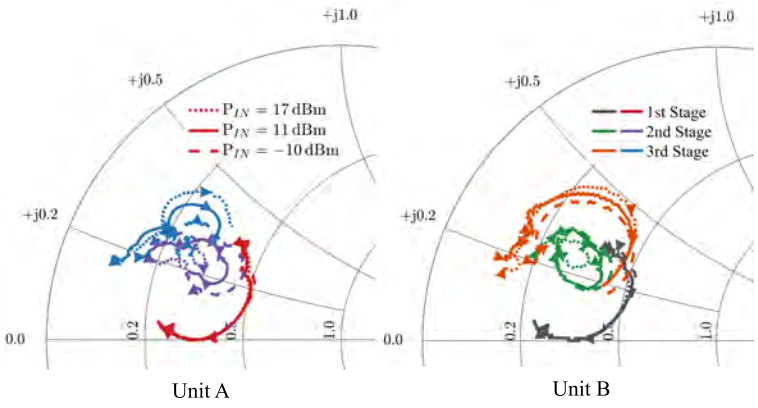

Figure 5.9: Reflection coefficient trajectories from 75 to 110 GHz (directive as the arrows on the smith chart) for the input of the transistors on the 1st, 2nd, and 3rd stages of the Unit-A and Unit-B PAs at different input power levels.

5.2.2 Staging Efficiency

The two different staging ratios enable a comparison of power-combining efficiency at each stage. First, we consider the PAE and gain for the different stages, which are inputs for Eq. 5.1. Fig. 5.10 shows the simulated PAE and gain over frequency at two input power levels. Note that for both staging ratios, the 3rd stage is the most efficient across the entire band at both power levels. The gain characteristics look similar, but the Unit A design has more gain for 11 dBm in the first and last stages. Correspondingly, the first-stage PAE of the Unit B design is lower, except at the low-frequency end of the band.

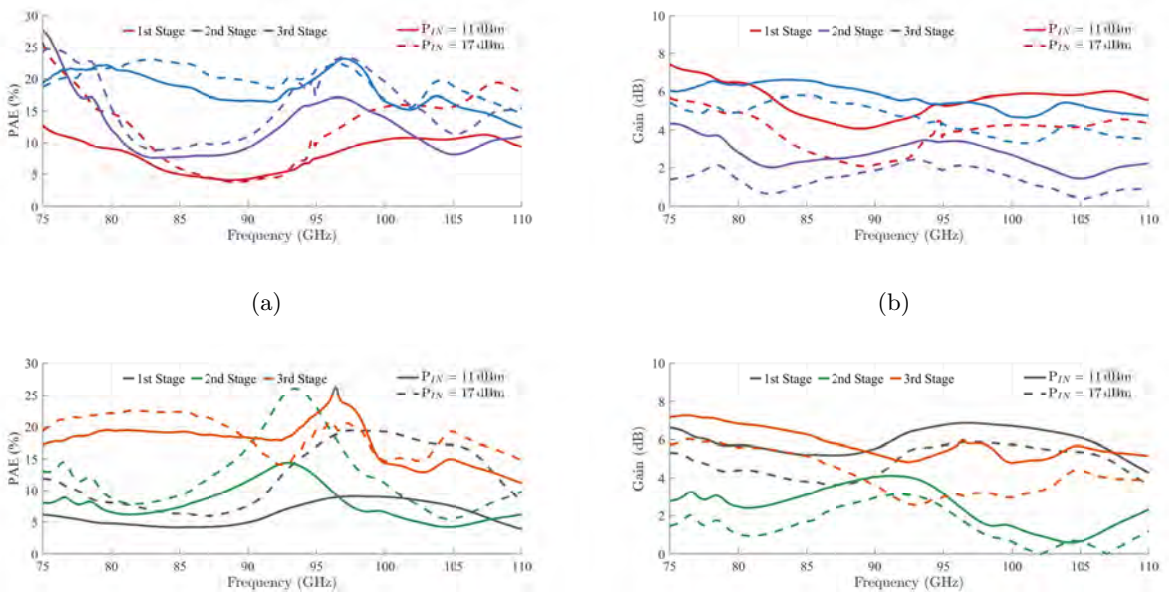

(a) (b)

(c) (d)

Figure 5.10: Simulated PAE and gain plotted for all three stages with $P_{IN} = 11\,\text{dBm}$ and $P_{IN} = 17\,\text{dBm}$, for the two PAs with different staging ratios: 1:2:3 in (a) and (b); and 1:2:2 in (c) and (d).

The staging efficiency (5.1) can now be calculated over frequency at each stage, as shown in Fig. 5.11. Overall, the combining efficiency for the Unit B staging ratio is higher across the band. The average combining efficiencies across the band are shown in Table 5.3. The first and the second stages perform worse at the edges of the band, but this is compensated in the overall 3-stage design. The final staging efficiency of the Unit B design is higher in simulations by up to 5 percentage points. The <100% staging efficiency is due to the broadband designs which cannot exactly follow the optimal maximum output power impedance trajectories of Fig. 5.3 and Fig. 5.8.

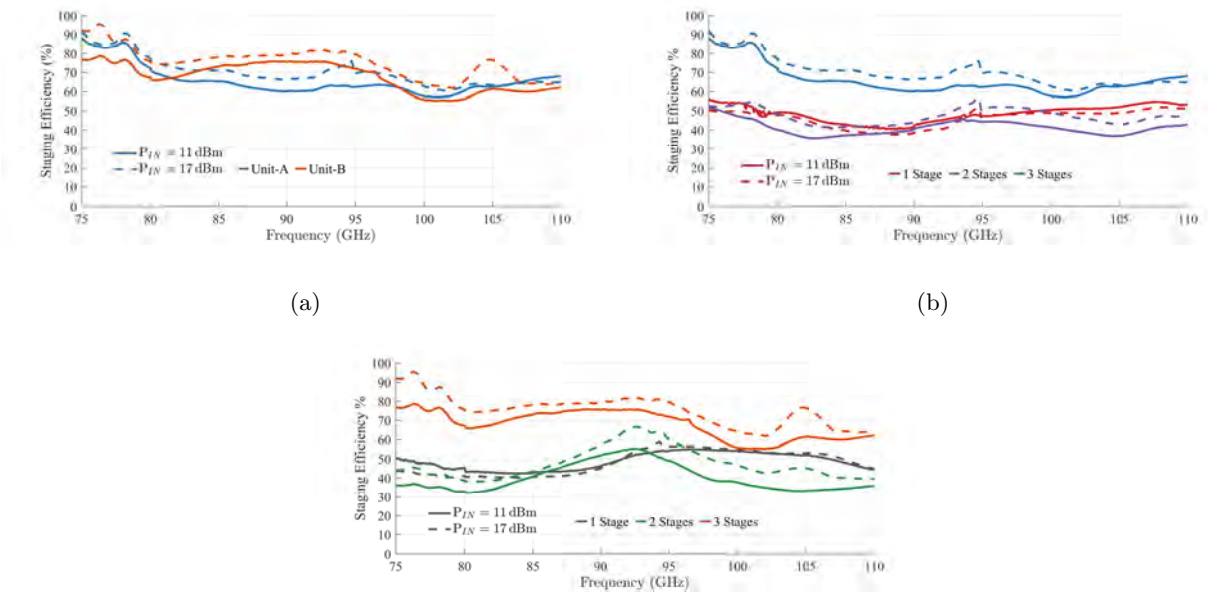

(a) (b)

(c)

Figure 5.11: Simulated staging efficiency, η_{Sm}, given by Eq.5.1 plotted for all three stages of the two PAs with different staging ratios, for $P_{IN} = 11\,\mathrm{dBm}$ and $P_{IN} = 17\,\mathrm{dBm}$. (a) Comparison of the total staging efficiency for all three stages. The η_{Sm} for the three stages of the (b) Unit-A and (c) Unit-B PAs.

Table 5.3: Average Staging Efficiency Values

Staging	P_{IN} (dBm)	1 Stage (%)	2 Stages (%)	3 Stages (%)
Unit-A	11	48.6	41.2	65.7
	17	46.2	47.3	70.1
Unit-B	11	48.8	40.2	68.0
	17	48.1	47.6	75.4

5.3 Measurement Setups and 3-Stage Unit PA Measurements

This section briefly describes the measurement setups and shows results on the Unit-A and Unit-B three-stage PAs.

5.3.1 Small-Signal Measurements

Small-signal measurements are performed with a Hewlett Packard 8510C Vector Network Analyzer (VNA) with V-band/W-band frequency extenders to WR-15/WR-10 waveguide, respectively. At the waveguide output, WR-15/WR-10 to 1 mm coax transitions connect to the 100 μm pitch GSG probes using 6 inch 1 mm coaxial cables. SOLT calibration is performed at the GSG plane with an alumina W-band impedance standard substrate from Cascade Microtech.

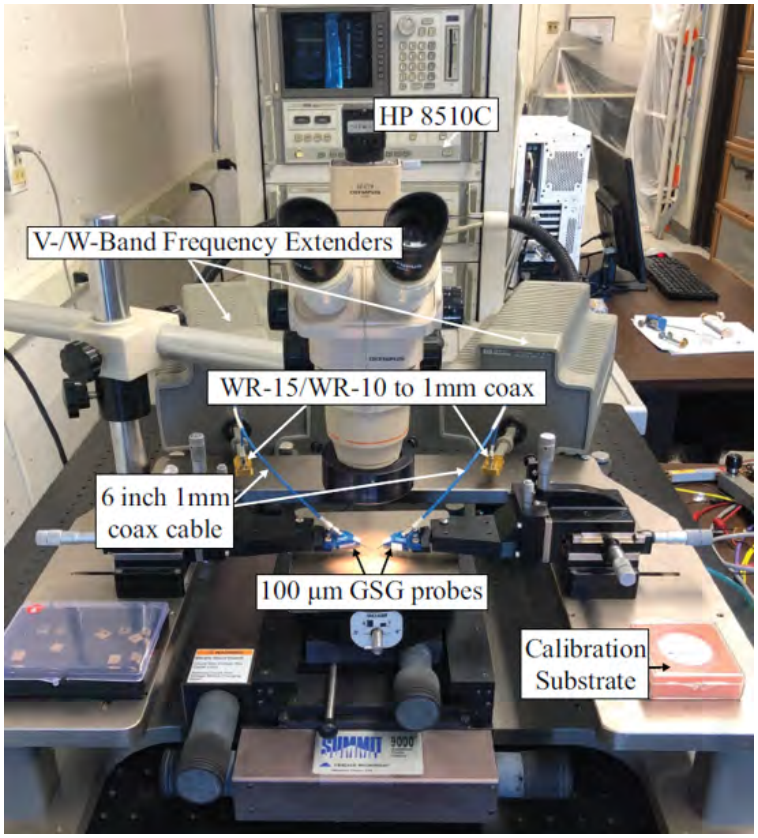

Figure 5.12: A labeled photograph of the small-signal measurement setup with the HP 8510c VNA.

The amplifier die is $3\times5\,\mathrm{mm}^2$ in size, as shown in Fig. 5.13. For low-frequency bypassing and stability, the chips are epoxied using Epo-Tek H20s on a gold-nickel coated copper-molybdenum (CuMo) carrier plate. MIM capacitors are placed in capacitor ladder of 0.1 and 1 nF close to the die to reduce bond wire inductance between the on- and off-chip capacitors. As many bond wires as possible are used to maximize current handling.

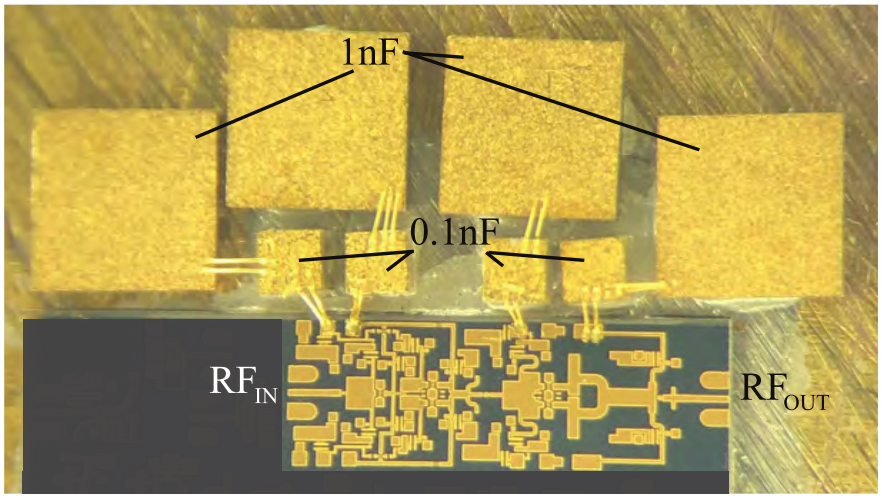

Figure 5.13: Photograph of the 3-stage Unit-B W-band 3.13 mm× 1.02 mm MMIC PA mounted on a CuMo carrier. The 4 bias pads are bonded with two 1-mil gold bond wires to 0.1 nF bypass MIM capacitors and subsequently to 1 nF MIM capacitors.

The small-signal measurements are taken on a single, stabilized amplifier, and are shown in Fig. 5.14 from 75 to 110 GHz. The bias conditions are V_{DD} = +6 V and +12 V simultaneously on both drains with I_D=90 mA on combined stages 1 and 2 and 60 mA on stage 3. The measured data shows larger gain for the Unit-B PA, which is consistent with the simulations in Fig. 5.7. The Unit-A PA gain is lower than predicted, but remains above 10 dB from 75 to 100 GHz at V_{DD} = +6 V. Fig. 5.15 shows the measurement to simulated comparison for +6 V on the drain for both Unit amplifiers.

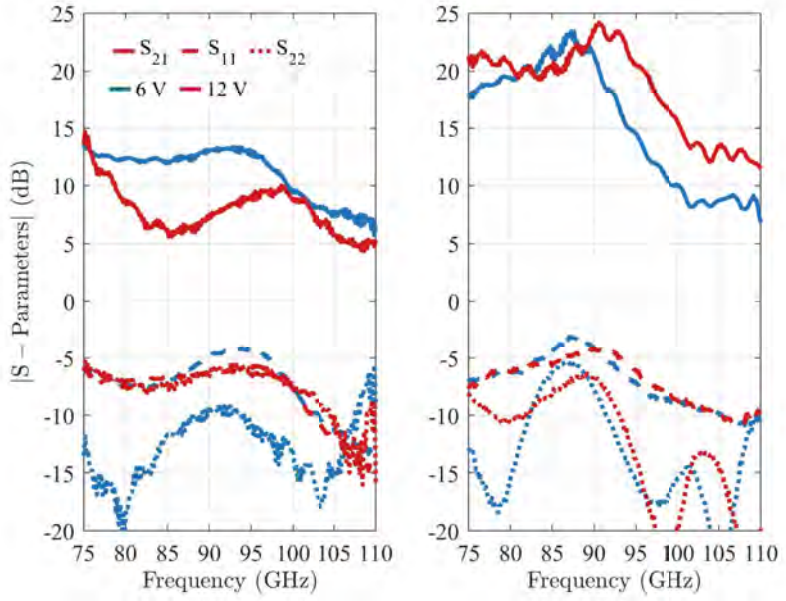

Figure 5.14: Measured S-parameters for $V_{DD} = +6\,\mathrm{V}$ and $+12\,\mathrm{V}$ with quiescent drain current of $200\,\mathrm{mA/mm}$, for the Unit-A (left) and Unit-B (right) three-stage PAs.

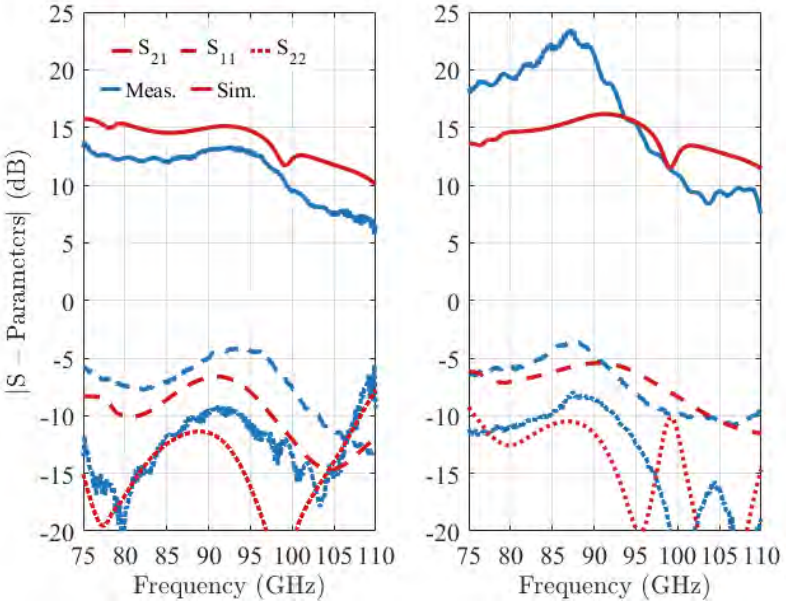

Figure 5.15: Comparison of simulation to measurement for the Unit-A (left) and Unit-B (right) three-stage PAs.

5.3.2 Large-Signal Measurements

A power-calibrated scalar test setup is used for large-signal measurements with a block diagram shown in Fig. 5.16a. The CW W-band signal is generated with a HP83650A sweeper in Ka-band. This is followed by a Quinstar amplification chain consisting of QPW-18402020-J0 Ka-band amplifier, QPM-93003W passive tripler, QFL-B4SW00 low-pass filter and QPI-W01820-H4W02 W-band driver amplifier, with a maximum output power of roughly 18 dBm. After this, an isolator with ~ 1.5 dB of forward transmission loss protects the amplification chain from any DUT mismatch. A 20-dB WiseWave coupler with a W-band power detector is calibrated with a W-band power meter. Calibrated power-meter measurements are also captured from a 10-dB coupler after the Ka-band amplifier.

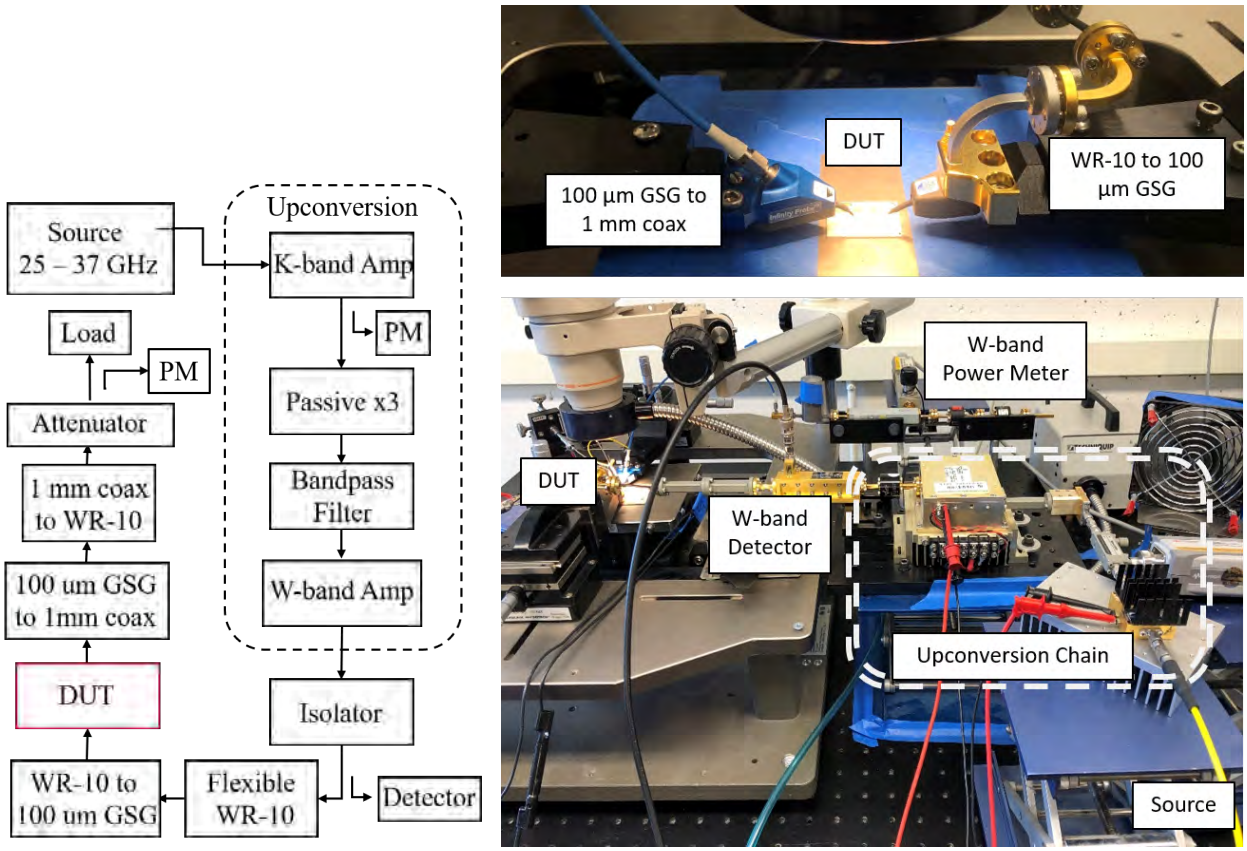

(a) (b)

Figure 5.16: Large-signal scalar power-calibrated measurement setup block diagram in (a) and a labeled photograph in (b) .

5.4 Conclusions

This chapter describes the design and analysis two 3-stage W-band MMIC PAs with simulated output powers over 25 dBm. Table 5.4 shows a summary of the measured large-signal results. The output power is lower than simulated due to a processing issue that resulted in high current collapse [143], lower g_m and lower $I_{\max}$. The power and gain are flatter over frequency for Unit-A. Fig. 5.17 shows the measured power for the Unit-B MMIC over the band at 9 dBm input power. The drive-up measurements are shown at the low edge of the band (75 GHz), center (92 GHz) and highest frequency with saturated gain above 5 dB (107.5 GHz). The design and measurement results

are described in [146].

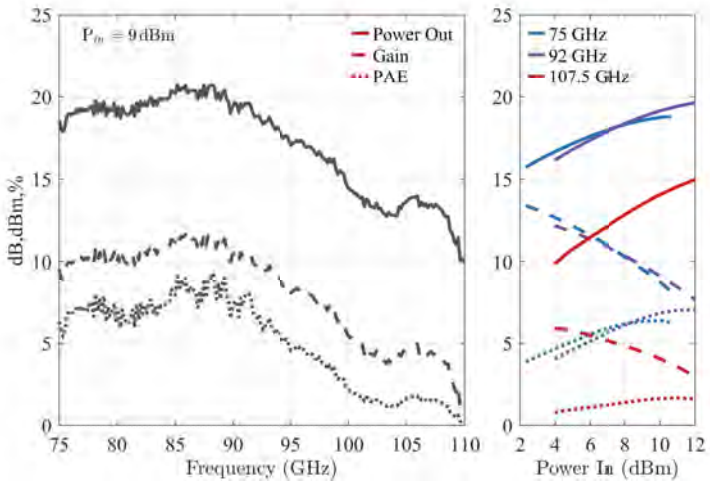

Figure 5.17: Large-signal Unit-B PA measurements over frequency (left) and compression at 75, 92, and 107.5 GHz (right).

Table 5.4: Large-Signal Measurements for Unit PAs

Freq.	Unit	P_{IN} (dBm)	P_{OUT} (dBm)	PAE (%)	Gain (dB)
75 GHz	A	10	18.9	7.7	8.9
	B		18.7	6.4	8.7
92 GHz	A	10	19.5	8.5	9.5
	B		18.7	6.1	8.7
110 GHz	A	10	15.3	2.8	5.3
	B		10.6	0.2	0.6

Chapter 6

Cicrcuit-level W-band Power-Combining Amplifiers

Contents

This chapter presents higher level of circuit-combining of two Unit-A amplifiers and three Unit-B amplifiers as shown in Fig 6.1a and b.

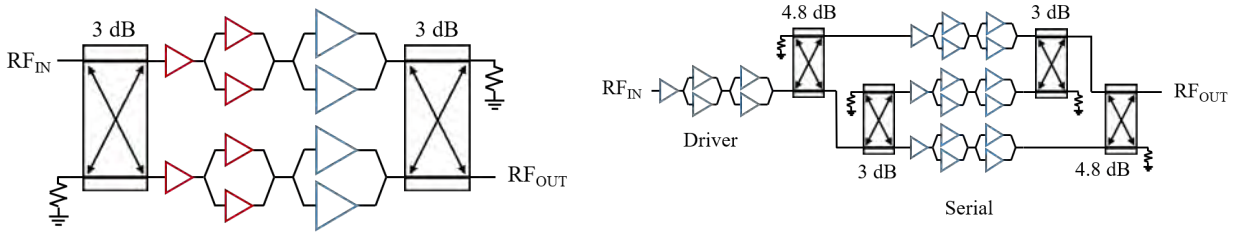

(a) (b)

Figure 6.1: Schematics of power amplifier (PA) topologies with increasing levels of power combining demonstrated in this chapter. (A) Balanced and (b) serially-combined (with a driver) architectures, using two and three 3-stage PAs from Chapter 5.

6.1 Combining Architectures

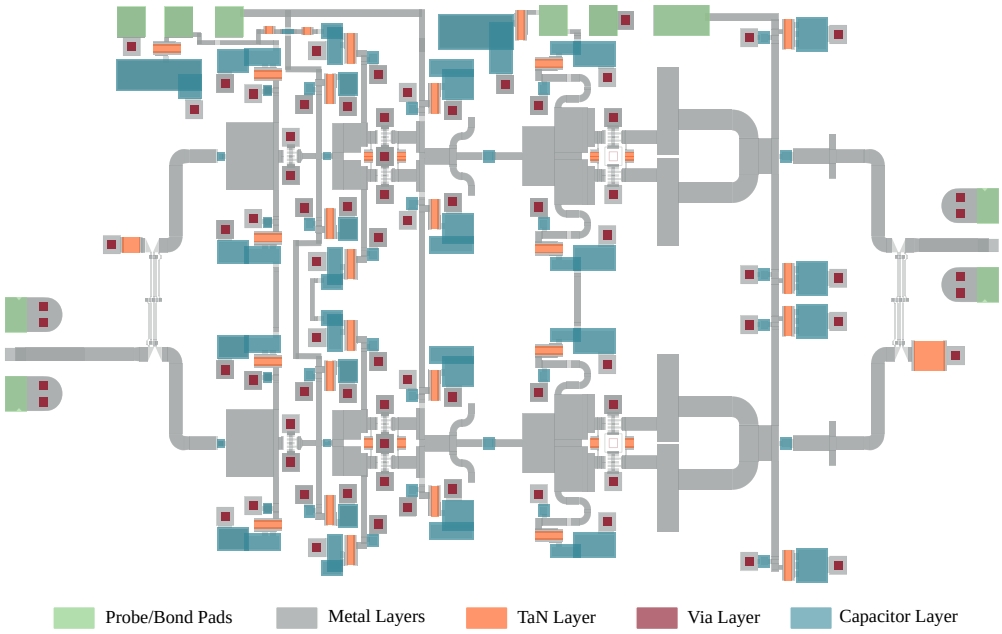

Figure 6.2: Layout of the balanced power amplifier using the Unit-A amplifier from Chapter 5.

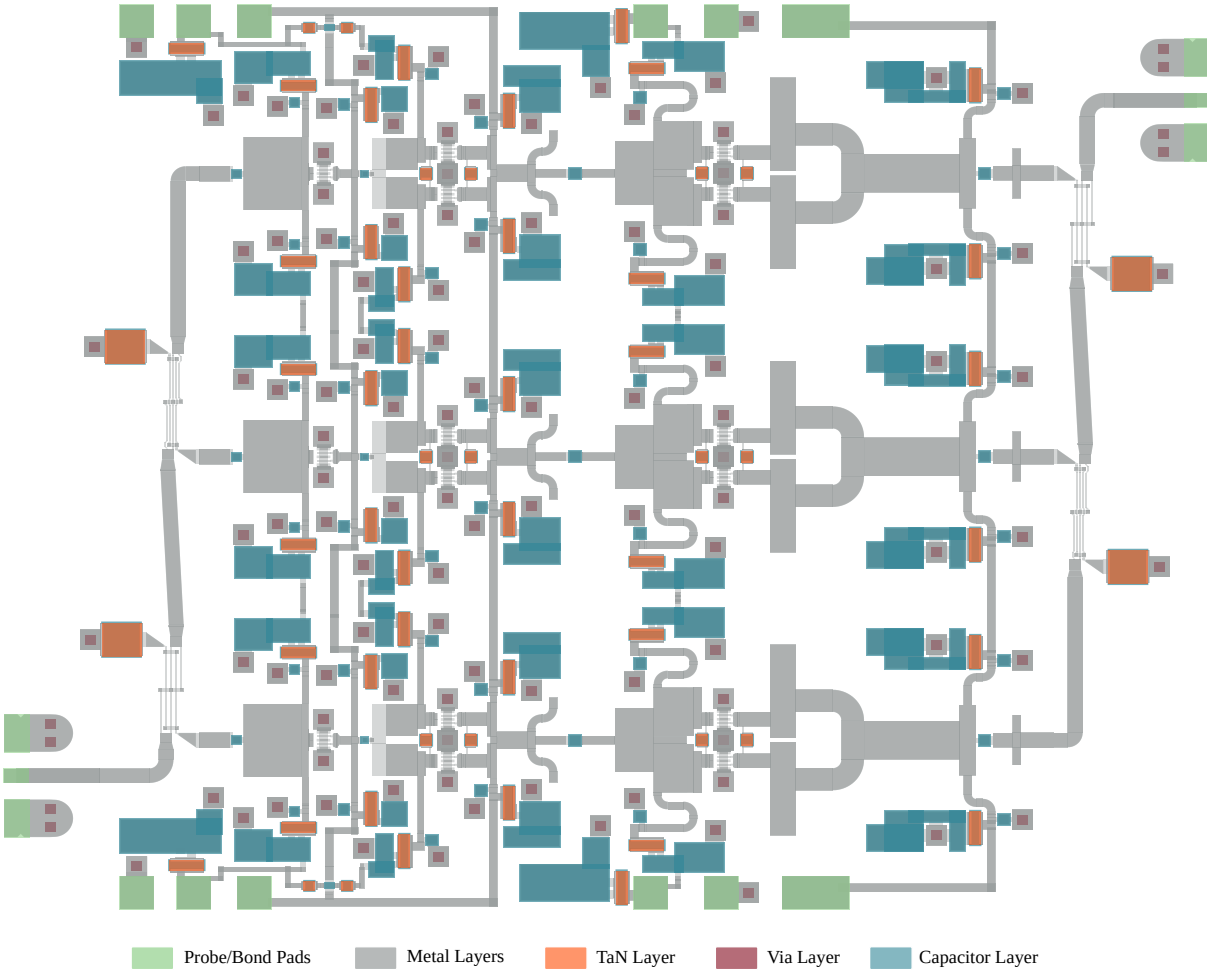

Figure 6.3: Layout of the serial power amplifier using the Unit-B amplifier from Chapter 6.

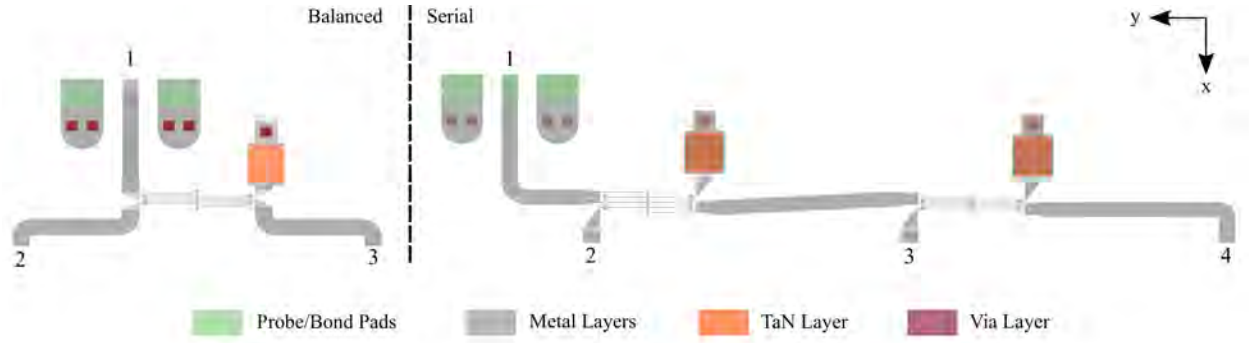

Figure 6.4: Layouts of the passive combiners: (a) Lange coupler for the balanced amplifier consisting of two Unit-A unit 3-stage PAs; and (b) cascaded Lange network for the three serially combined Unit-B 3-stage PAs. The size of the balanced combiner is $590 \times 1100\,\mu$m and the serial combiner is $585 \times 2070\,\mu$m.

The layouts of the balanced and serially combined MMIC PA are in Figs. 6.2 and 6.3. The passive combiner layouts for the two cases are shown in Fig. 6.4. The design challenge in these networks is to maintain amplitude and phase balance over the entire W band, since it affects power-combining efficiency. Fig. 6.7 shows the amplitude and phase imbalance for the 2:1 and 3:1 combiners. In the balanced amplifier, the 0.6° phase imbalance of the divider is inverted at the output combiner, but the amplitude imbalance affects saturation, and therefore the output power. In the serial combiner, both amplitude and phase affect the output power, since the input divider and output combiner networks are not symmetric and the middle amplifier will not have the same phase as the outer two at the RF output port.

The simplest way to think of the output power combining efficiency is to consider the loss of the passive output combiner and assume that the Unit amplifiers operate identically in the combined amplifier. Fig. 6.5 shows the S-parameters of the EM simulated combining networks. Using this data and Eq. 3.2, the output combining efficiency of the balanced amplifier ranges from 94.6% to 92.5% across the band being lowest at the low edge of the band. While for the serial combiner Eq. 3.2 is modified to include the fourth port, resulting in an output combining efficiency resulting in a range from 90% to 86.5%. These efficiencies can be seen in Fig. 6.6 over the frequency range.

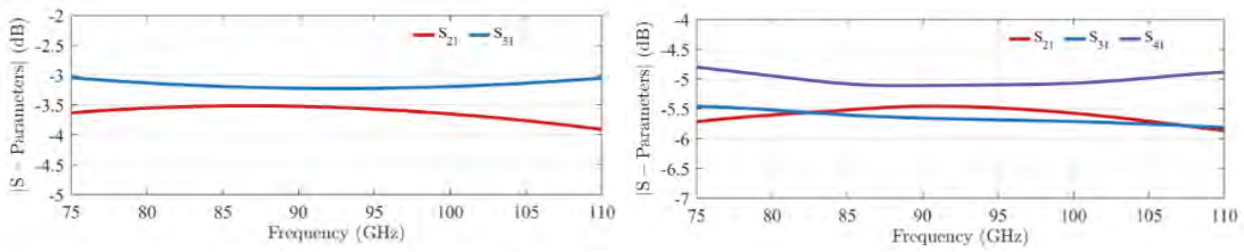

(a) (b)

Figure 6.5: (a) The simulated S-parameters of the EM-simulated balanced combining network and (b) simulated S-parameters of the EM-simulated serial combining network.

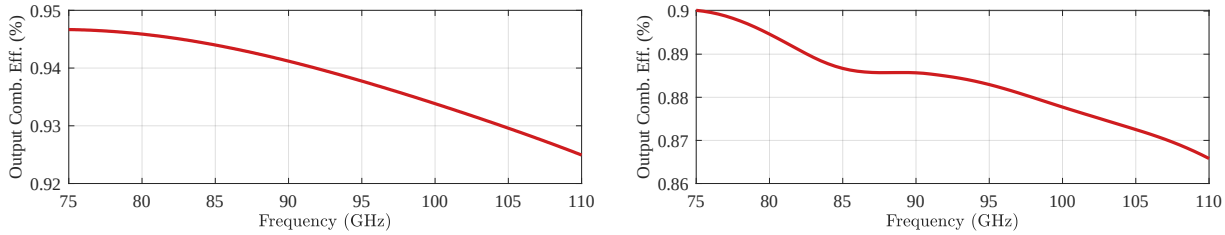

(a) (b)

Figure 6.6: The output combining efficiency of the passive lange networks for (a) balanced and (b) serial PAs.

In order to quantify the power-combining degradation due to amplitude and phase imbalances, we define the combining efficiency as function of P_{IN}:

$$\eta_{\text{comb}}(\text{P}_{IN}) = \frac{\text{P}_{OUT}}{\text{P}_{MAX\,|ideal}} \tag{6.1}$$

where P_{IN} is the input power at each of the 2 or 3 combined PAs, and $P_{MAX\,|ideal}$ is the output power assuming ideal divider/combiners of Fig. 6.4. It is interesting to evaluate $\eta_{\text{comb}}(P_{IN})$ for the case when only amplitude imbalance is present, as well as when both phase and amplitude imbalance occur. The results are shown in Fig. 6.8 for two input power levels, confirming that the balanced amplifier has a higher and more frequency-independent combining efficiency above 80%

across the band. The combining efficiency when including both amplitude and phase imbalances tracks the EM-simulated frequency-dependent behavior very closely. For the higher input power level, there is a resonant dip at 95 GHz which is predicted by the simulations and is also present in the staging efficiency in Fig. 5.11.

It is important to understand that the Unit amplifiers do not behave identically across the band when they are combined due to a different impedance environment presented at their input and output ports. Therefore, at some frequencies, they can produce more power than n times than that of the Unit amplifier alone. This explains the high efficiency numbers at e.g. 100 GHz for the serially combined PA and 87 and 102 GHz for the balanced PA.

For the case of the serially combined PA, the variation across the band is higher and again well predicted when both amplitude and phase imbalances are taken into account. The simulated small and large-signal performance for the balanced and serially-combined PAs are summarized in Fig. 6.9 and Fig. 6.10, showing the expected increase in power and comparable gain. The balanced PA shows 3-4 dB more small signal gain, while the serial PA shows more output power.

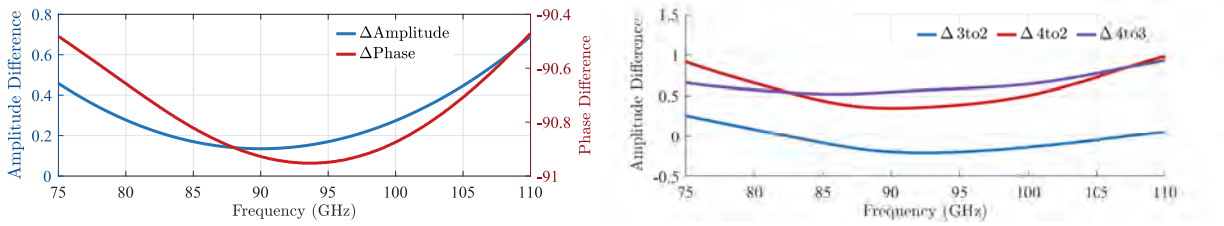

(a) (b)

Figure 6.7: (a) Amplitude and phase imbalance at the output of the EM-simulated Lange divider and (b) amplitude differences at the inputs of the 3 PAs combined serially in Fig. 6.4 at ports 2, 3, and 4. The corresponding phase difference between port pairs (2,3) and (3,4) is about 200°, and between ports 1 and 2 is about 100°.

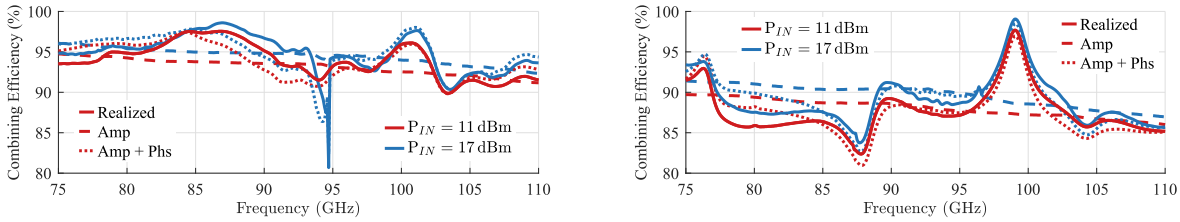

(a) (b)

Figure 6.8: Power-combining efficiency η_{comb} for the balanced (a) and serially (b) combined PAs for different imbalance cases: amplitude only (dashed line); both amplitude and phase (dotted); and EM-simulated actual layout (solid).

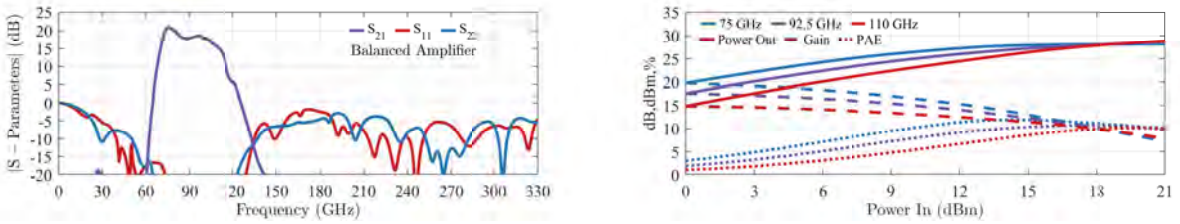

(a) (b)

Figure 6.9: (a) Small-signal simulated performance of the balanced architecture from 0.1 to 330 GHz at $V_{DD} = +12\,\text{V}$ showing no gain below the operating band. (b) Simulated large-signal drive-up characteristics at 75 (blue), 92.5 (purple), and 110 GHz (red).

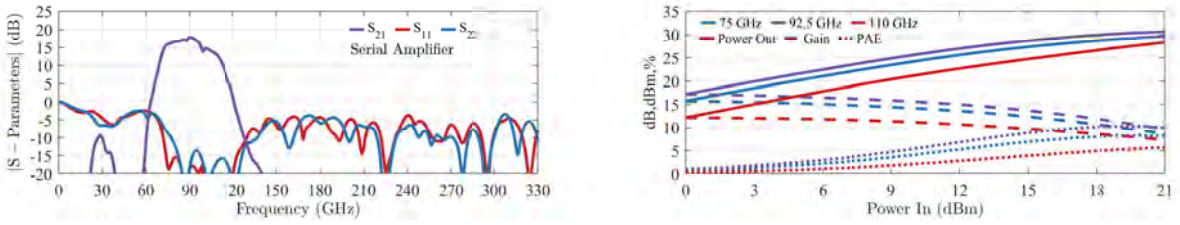

(a) (b)

Figure 6.10: (a) Small-signal simulated performance of the serial architecture from 0.1 to 330 GHz at $V_{DD} = +12\,\text{V}$ showing no gain below the operating band. (b) Simulated large-signal drive-up characteristics at 75 (blue), 92.5 (purple), and 110 GHz (red).

6.2 Measurements of Balanced and Serially-Combined MMICs

The balanced and serial PAs are measured using the same approach as for the unit PAs, but with an added Unit-B PA as a driver for the serial PA. Fig. 6.11 a and b show the mounted dies with external stabilization and bias capacitors. The small-signal measurements are shown in Fig. 6.12, and small-signal gains are lower than the model predicts. The balanced PA gain is consistent with the Unit-A PA, as expected. The serially-combined PA uses 3 Unit-B PAs but shows significantly lower small-signal gain, indicating that perhaps one of the three amplifiers was not providing gain. This advanced fabrication process is still under development at the time of the writing of this chapter, and in the presented fabrication runs shows a higher current collapse and lower g_m and I_{max} than expected.

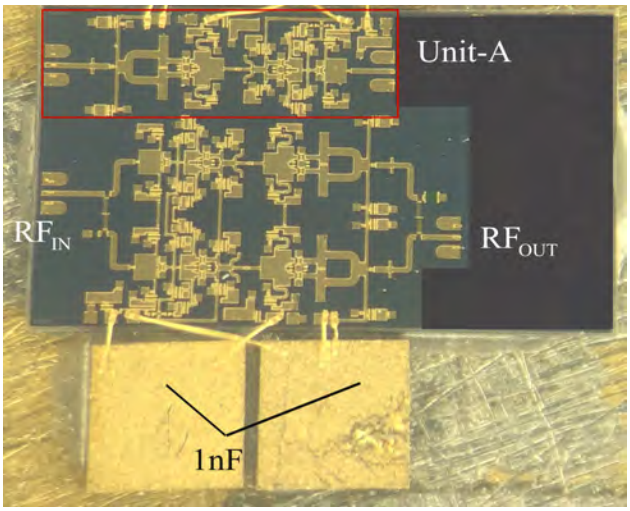

(a)

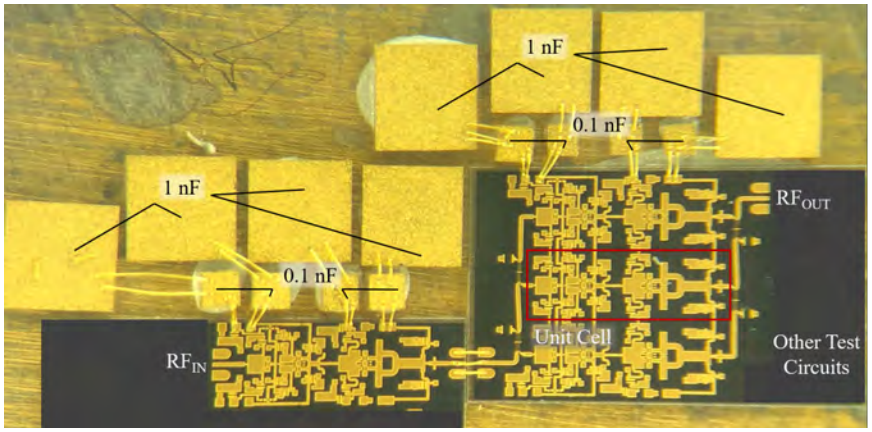

(b)

Figure 6.11: Photograph of the mounted (a) balanced and (b) serial (with a Unit-B driver) MMIC PAs.

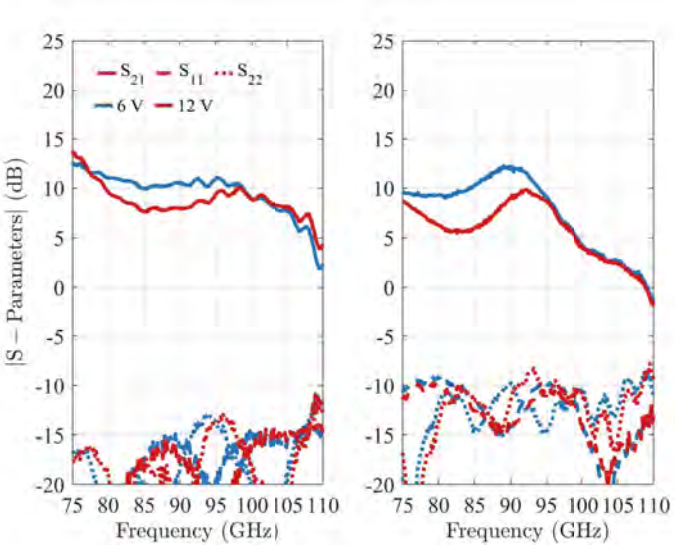

Figure 6.12: Small-signal measurements of the (left) balanced and (right) serially-combined (without the driver) MMIC PAs.

The large-signal measurements for both power-combined PA MMICs are shown in Figs. 6.13 and 6.14 and the results are summarized in Table 6.1. The measurements of the balanced PA show agreement to simulations within 2 dB and have greater power output with a bias of $V_{DD} = +6$ V in the lower half of the band. A large disagreement between simulated and measured output power of the Unit-B and serially-combined PAs shows the results of reduced g_m and I_{max}: the measured saturated output powers for serial PA alone are about 3 dB lower than predicted and the gain drops below 0 dB slightly before 110 GHz. Using a Unit-B PA as a driver (seen in Fig. 5.13b), the power output of the serial PA (seen in Fig. 6.14) is significantly improved, up to 7 dB more at 75 GHz, and shows up to 8.6 dB of saturated gain at 110 GHz.

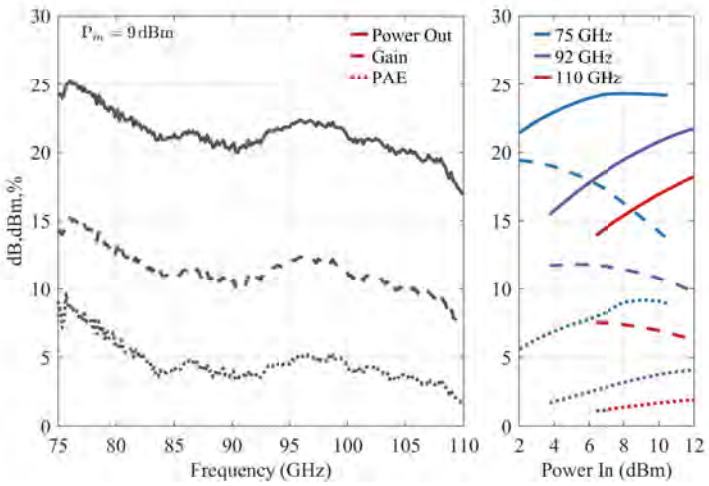

Figure 6.13: Large-signal measured characteristics of the balanced PA over frequency (left) and as a function of input power at the lower, center and upper parts of W band (right).

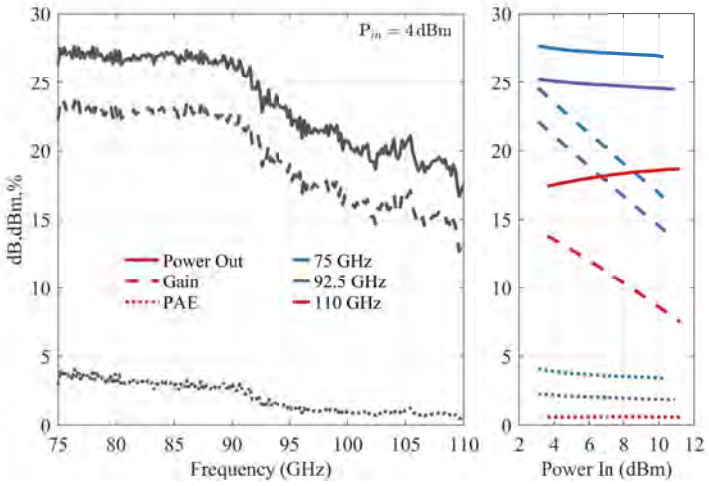

Figure 6.14: Large-signal measured characteristics of the serially-combined PA with the Unit-B driver over frequency (left) and as a function of input power at the lower, center and upper parts of W band (right).

Table 6.1: Large-Signal Comparison for Balanced vs. Serial

Freq.	Topo.	Simulated P_{OUT}*	Measured P_{OUT}*	PAE (dB)	Gain (%)
75 GHz	Bal.	22.1	24.2	9.1	14.3
	Serial	24.9	20.6	2.0	10.6
	D + S	29.8	27.0	3.5	17.0
92 GHz	Bal.	19.1	20.9	3.7	10.9
	Serial	26.4	20.5	1.9	10.5
	D + S	31.0	24.5	2.0	14.5
110 GHz	Bal.	18.1	16.9	1.7	6.9
	Serial	21.9	-	-	-
	D + S	28.9	18.6	0.6	8.6

* Units are in dBm and are simulated at P_{IN} = 11 dBm and measured at P_{IN} = 10 dBm

We next analyze combining efficiency at the circuit level, summarized in Table 6.2 at P_{IN}=9 dBm. The measured combining efficiency is defined as the measured power output of the MMIC PA over the perfect +3 dB (balanced) and +4.8 dB (serial) combining of the respective Unit PAs. The measured balanced PA combining efficiency shows agreement to simulations across the band with above 100% at 92 GHz. The measured serial PA combining efficiency shows close agreement to simulated with a drop-off in the higher region, most likely attributed to high current collapse and lower g_m of this run.

Table 6.2: Large-Signal Combining Efficiency

Freq.	Topo.	P_{IN} (dBm)	Meas. CE (%)	Sim. CE (%)
75 GHz	Balanced	9	94.7	93.6
	Serial		91.9	91.6
92 GHz	Balanced	9	108.0	93.3
	Serial		95.4	87.5
110 GHz	Balanced	9	93.7	91.6
	Serial		72.4	85.2

6.3 Conclusions

This chapter demonstrates circuit-level power-combining of two and three Unit PAs with measured highest powers of 27, 24, and 18 dBm at 75, 92, and 110 GHz respectively. Although the measured power levels are lower than simulated due to process fabrication issues, the power-combining efficiencies closely track simulated values and are above 85% in all cases and are as high as 95%. These result are reported in [146].

Chapter 7

MMIC Process-related Statistical Analysis

Contents

Due to the short gate sizes in the 10s of nm range, as well as complex heterostructures, millimeter-wave GaN processes exhibit variations larger than their lower frequency microwave counterparts. The goal of this chapter is to provide an analysis and understanding of effects of variations in millimeter-wave GaN MMIC PAs on overall performance of a transmit array. The statistical analysis process flow consists of data collection, estimation of a probability density func-

tion, sampling from the estimated pdf, and the subsequent application of the samples to a stated problem.

Here, we perform this statistical analysis for a portion of a transmit chain, taking into account the measured variations in MMIC PAs and simulated variations in transitions from microstrip-to-waveguide antenna feeds. We fit and estimate the marginal and bi-variate probability density functions of measured amplifier small-signal amplitude and phase of the S_{21}, comparing two methods (Gaussian and kernel estimation). The goal of this analysis is to determine the most appropriate probability density function (pdf) for GaN-on-SiC MMIC process fabrication variation.

7.1 W-band MMIC Design in Qorvo GaN09

Here we describe briefly a GaN MMIC PA designed for around 1 W output power across the 75 to 110 GHz frequency range, detailed in [42]. The circuit architecture is shown in Fig. 7.1, and is a 5-element chain amplifier similar to that in [132]. The number of sections, $n = 5$, is chosen to achieve 1 W output power. The amplifier is implemented in Qorvo's 90 nm T-gate GaN-on-SiC process. Each unit cell power amplifier is a 3-stage, 2-way power combined topology, with a layout shown in Fig. 7.2. Using non-linear EEHEMT models for $2 \times 40\,\mu$m, $4 \times 30\,\mu$m, and $4 \times 40\,\mu$m devices, drive staging is chosen with efficiency in mind. The bias conditions are kept at the modeled quiescent current, where 150 mA/mm corresponds to class-AB operation. The drain currents are 24 mA, 36 mA and 48 mA for the first, second and third stages, respectively.

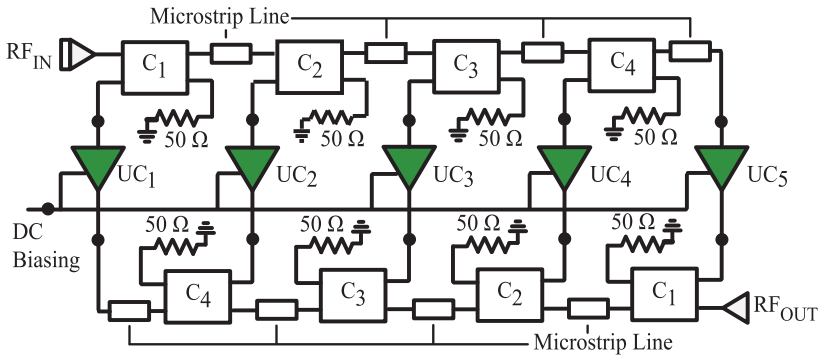

Figure 7.1: Circuit block diagram of the chain power amplifier architecture with 5 unit cell (UC) 3-stage PAs connected through Lange couplers. All 5 unit cells are biased from the same voltage supplies.

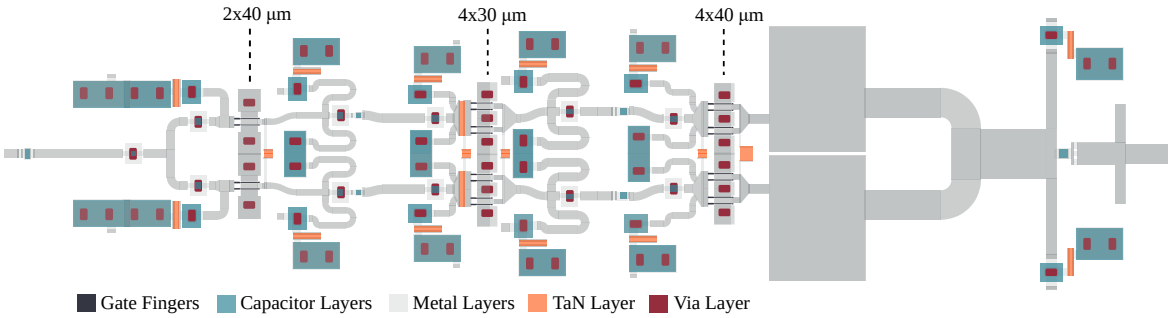

Figure 7.2: The layout of a unit cell PA in the 5-way serial power amplifier from Fig. 7.1. The staging ratio is 1:1.5:2, and the peripheries for stages 1, 2, and 3 are 160 μm, 240 μm, and 320 μm, respectively. The die area is $2.75 \times 0.64\,\text{mm}^2$. Some metal layers and proprietary transistor layers have been removed.

Transistors in millimeter-wave processes have high gains in the lower frequency region, and therefore, stability must be carefully analyzed. Multiple stability analysis methods were performed during design – K factor, internal Nyquist stability, and loop gain [144,145]. For in-band stability, resistors in the RF-path directly on the second stage gates introduce a small enough loss while maintaining overall efficiency. Small resistors, about 5 Ω, are in the dc path of the gates in all stages. To eliminate odd-mode instability, resistors are placed in the symmetry line and minimized in value using loop-gain simulations. The reactive output combiner is modeled and optimized to

reduce current imbalances.

Due to the large lower-frequency transistor gain, out-of-band stability is considered under process variations, specifically with $g_m \pm 30\%$, $C_{gs} \mp 30\%$, and $C_{gd} \pm 30\%$ and the SiN thickness varied by $\pm 10\%$, which result in instabilities between 16 and 40 GHz. A small blocking capacitance (0.03 pF) absorbed in the matching network, together with low-frequency bypassed resistors, provide a viable solution for low-frequency gain reduction, while maintaining bandwidth above 75 GHz. The resulting loop gain simulations of the final unit cell design in Fig. 7.3 show a phase margin greater than 30°.

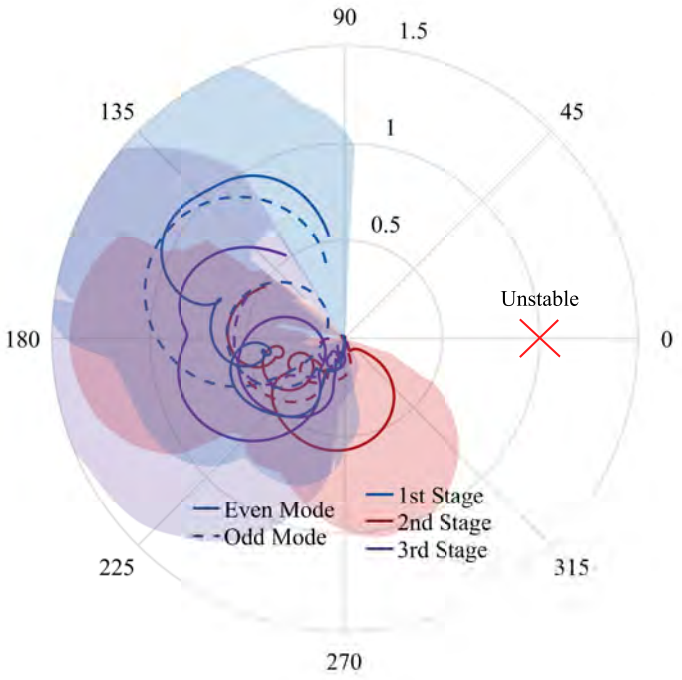

Figure 7.3: Loop gain simulations from 0.1 to 120 GHz. Both even and odd mode (due to symmetry and 2-way power combining) loop gain is analyzed at each stage. As can be seen, the nominal condition is far from the unstable region.

The stabilized unit cell PAs are arranged as in Fig. 7.1, where the input power is coupled to each of the 5 cascaded PAs for uniform drive. The outputs combine coherently and each of the unit PAs operates under the same conditions (same gain, PAE, and P_{out}). A series of four Lange combiners with varying coupling coefficients are designed. The choice of the coupling factors C_1

through C_4 is critical for equal power input, as described in [132]. For a 5-way combiner, C_4 can be found from

$$C_4^2 = \frac{t_4^2}{1 + t_4^2} \tag{7.1}$$

where t_4^2 is the efficiency of the fourth section. The remaining sections follow a recursive relationship:

$$C_i^2 = \frac{C_{i+1}^2 t_i^2}{1 + C_{i+1}^2 t_i^2}, \qquad i = 3, 2, 1 \tag{7.2}$$

Fig. 7.4 shows the coupling coefficients for a 5-stage chain PA, as a function of loss per stage. Equations (1) and (2) result in $(C_1, C_2, C_3, C_4) = (7.0, 6.0, 4.8, 3.0)\,\text{dB}$, assuming an efficiency of 1. The ports of the Lange couplers require a layout with two 90-degree bends, modified from the standard layout, as shown in Fig. 7.5 for a 3-dB version. The coupler design is adjusted by adjusting the gap between the coupled lines. The different current distribution for the different port layouts are shown in Fig. 7.5. It can be seen that careful EM simulations result in a design with coupling and through parameters that are flat across the band.

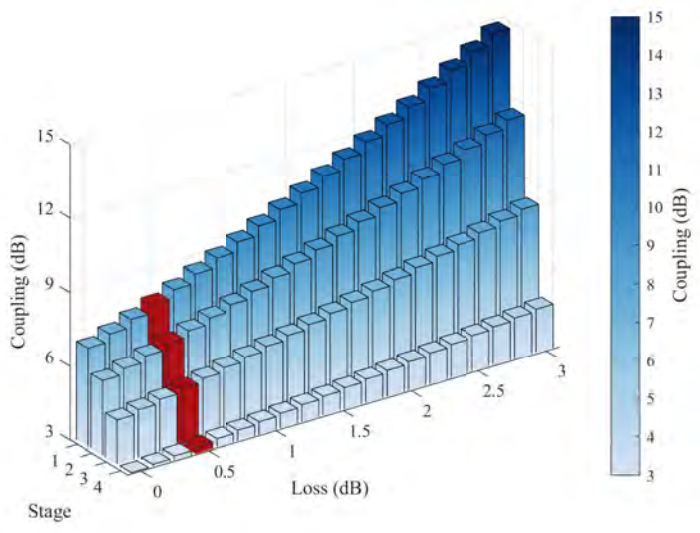

Figure 7.4: A choice of coupling at each stage in Fig. 7.1 assuming 0.5 dB of loss in each coupler and subsequent transmission line is shown in red. A pragmatic approach would be to have this choice as a first pass and calculate the loss of each coupler design around the coupling value.

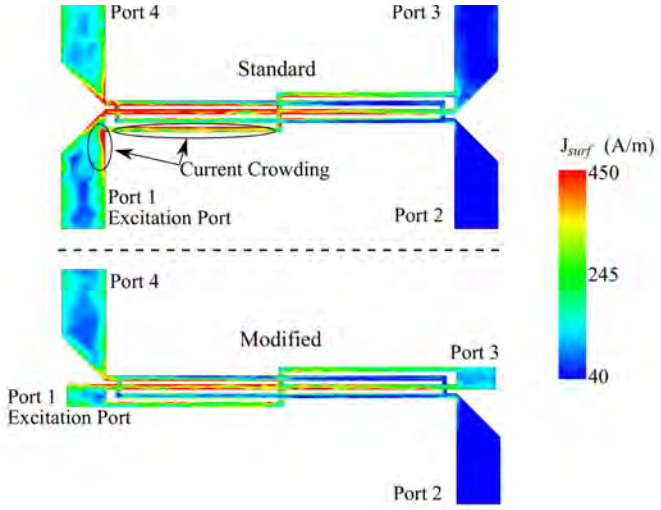

(a)

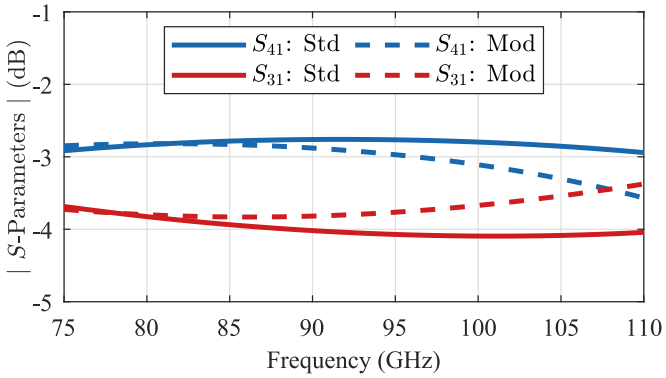

(b)

Figure 7.5: (a) Standard W-band 3-dB Lange coupler port layout and modified layout as required by PA design showing surface current amplitude distribution. (b) Comparison of full-wave simulated through and coupled parameters for the two cases. The current distribution in the standard results in more variation across the band than the optimized design.

In the final chain PA design from Fig. 7.1, low-dispersion loss for each section ($\sim 0.5\,\mathrm{dB}$) is found through careful EM modeling with optimization of feed structures and minimized current crowding in the Lange fingers. This loss corresponds to the highlighted coupling coefficients in Fig. 7.4, which are implemented in the final layout shown in Fig. 7.6 of the fabricated MMIC.

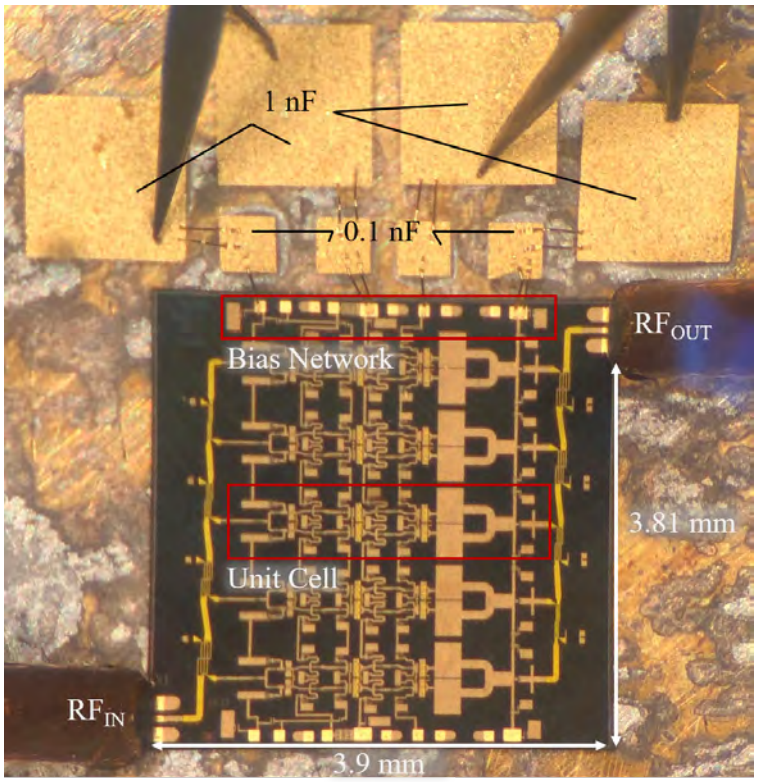

Figure 7.6: Photograph of a 5-way serially combined 3-stage MMIC power amplifier designed for full W-band coverage mounted on a CuMo carrier with bondable MIM capacitors. The left GSG pad is the RF input, connected to coupler C_1. The size of the die is 3.9 mm×3.81 mm.

The simulated and measured small-signal frequency response is shown in Fig. 7.7a. The measured performance of 2 out of the 83 chips shows that the nonlinear model over-estimates small signal gain. Fig. 7.7b shows the simulated large signal gain saturation across frequency. The simulated and measured large signal performances, on the 2 MMICs, as a function of input power at 81 and 94 GHz are shown in Fig. 7.8a and Fig. 7.8b respectively. The small-signal measurements are obtained with an HP8510C network analyzer with millimeter-wave extenders. SOLT calibration is performed at the GSG plane with an alumina W-band impedance standard substrate from Cascade Microtech. A power-calibrated scalar test setup is used for large-signal measurements. The signal is generated with a sweeper in Ka-band, followed by a Quinstar Ka-band amplifier, passive tripler, and W-band amplifier.

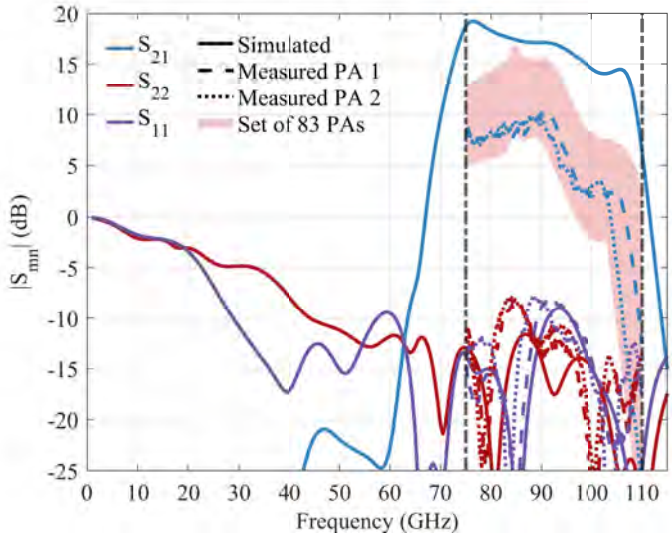

(a)

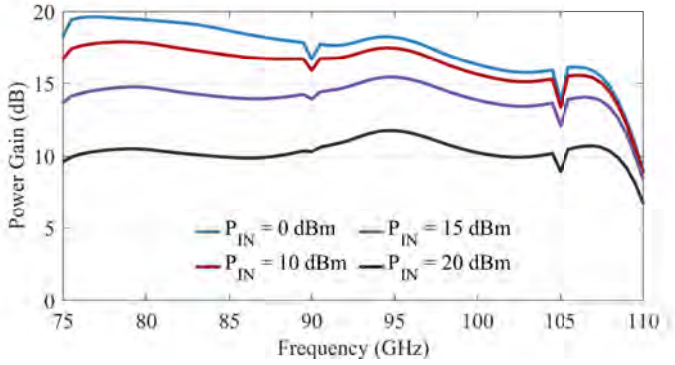

(b)

Figure 7.7: (a) Small-signal simulated and measured performance of the 5-section chain PA from 0.1 to 115 GHz with two representative mounted MMIC PAs. The red shaded area is the full range of the measured 83 MMICs. The dashed vertical bars represent the limitations of the measurement systems used. (b) Large-signal simulated gain shows similar compressive characteristics over frequency.

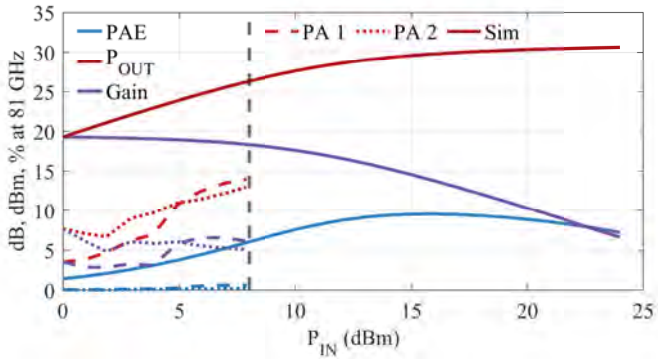

(a)

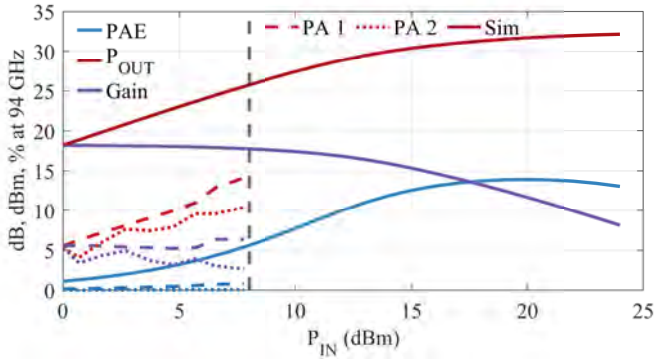

(b)

Figure 7.8: Simulated and measured large-signal characteristics over a power input sweep at (a) 81 and (b) 94 GHz with two representative MMIC PAs. The dashed vertical bars represent the limitations of the measurement systems used.

As shown in Fig. 7.6, 1 nF and 0.1 nF off-chip capacitors were mounted and are intended to suppress lower-frequency bias-line oscillations. With the chip and capacitors mounted and under bias, no oscillations are seen on a 50 GHz spectrum analyzer connected via a 100 μm GSG-to-2.4 mm coax probe. Although a W-band spectrum analyzer was not available, our experience is that usually even higher-frequency oscillations have down-converted frequency components that are observable with a spectrum analyzer, indicating that the PA is stable. Additionally, the measurements are repeatable over time, and no fluctuations in dc current are observed when biasing the device and with RF input power, which would provide another indication of instability.

Data across wafers was only available for small-signal parameters and therefore the remainder of the chapter uses small-signal data for the variation analysis. Nevertheless, this analysis can be easily extended to be statistically meaningful in large-signal operation given large-signal measurements of the entire data set.

After fabrication, 83 chips from three separate wafers and two wafer lots were measured on-wafer in small-signal with identical biasing conditions. The variation of S_{21} across the chips is shown in Fig. 7.9. The solid line is the mean value of the measurements and the shaded area encompasses two standard deviations. The two frequencies (81 and 94 GHz) are used in the remainder of this chapter for the statistical analysis.

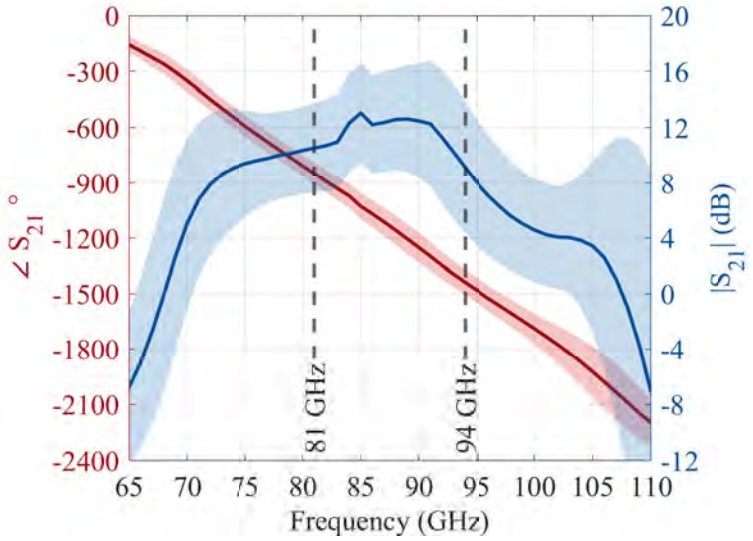

Figure 7.9: Measured $|S_{21}|$ and unwrapped $\angle S_{21}$ for 83 MMIC PAs. The solid line is the mean and the lightly shaded region is two standard deviations from the mean. The dashed lines are the frequencies with which the rest of the chapter uses in the analysis.

With the fabrication variation measured, each MMIC element has differing transmission amplitude and phase. If an array system designer is given 83 MMICs with an 4×4 array, there are $n!/(c!(n-c)!) = 83!/(16!(83-16)!) = 5 \times 10^{16}$ combinations without replacement. Now, it is of interest to quantify the boundaries and features of the MMIC variation to be able to estimate the

constraints the array system designer needs to place on certain design tolerances. However, the sources of the process variation are not contemporarily well-modeled.

7.2 GaN-on-SiC Process Variation Summary

The process variations for millimeter-wave MMICs with gates shorter than 100 nm are due to factors from epitaxial growth of GaN on SiC [147, 148] to gate definition [149, 150]. Substrate non-uniformities include warpage [151, 152], bowing [151, 153] and substrate and epilayer defects [148, 154–157]. Published knowledge on these defect effects on device performance is reviewed in [154], with increased leakage current, reduced blocking voltage, electric field crowding on surface pits, and local reduction of carrier lifetime being the most important contributors. One of the biggest sources of performance spread comes from poor process control in surface cleaning, which can cause variations in current collapse and in the depletion region. All of these mechanisms create large uncertainty of device performance from lot-to-lot, wafer-to-wafer and across a wafer. Devices vary radially across a wafer due to bowing, ohmic contact and gate growth is affected by wafer warpage, and epitaxial layer growth is sensitive to substrate defects. Table 7.1 summarizes qualitatively processing issues when transistors are scaled for millimeter-wave operation.

Table 7.1: Summary of mm-Wave Scaling Tradeoffs in GaN HEMTs

Scale/Optimization	Improvement	Degradation
↓ gate length	↑ f_T	↑ short channel effects
↓ barrier thickness	↓ short channel effects	↑ gate leakage ↑ surface dispersion ↓ electron sheet density
↓ channel width (Length of source to drain)	↓ drain-to-source delay ↑ electron velocity ↑ max drain current	↑ parasitic capacitances ↓ breakdown voltage ↑ short channel effects
↑ passivation thickness	↑ device reliability ↓ surface dispersion	↑ parasitic capacitances
asymmetric gate	↑ breakdown voltage ↓ short channel effect ↓ gate current leakage	↓ yield
more complex ohmic contact	↓ R_{on} ↑ electron supply	↑ non-uniformity across wafer
back barrier	↑ electron confinement ↓ short channel effects	↑ deep traps

* References used in compilation of this table are [147, 149, 150, 156]

There are limited published statistical analyses for millimeter-wave power amplifier performance related to processing variations. A recent simple study that displays RF measured wafer statistics for K-band PA MMICs is given in [158] for a mature foundry process. The results show that even optimized commercial foundry processes have significant variation in small and large-signal regimes

at lower millimeter-wave frequencies. For an analysis of device variations that can be applied to cascaded elements in a transmit array, the first step is to understand the pdf associated with measured MMIC data.

7.3 Probability Density Functions and Parametric vs. Non-Parametric Distributions

Density estimation is the problem of fitting a probability distribution of a random variable x given a finite set. Let us assume here that the data points are independent and identically distributed (iid). This problem is ill-posed as there are infinitely many distributions that could potentially generate this finite data set. Parametric distributions are pdfs generated by a limited number of parameters, such as a Gaussian with mean and variance, or a Rayleigh dsitribution with parameter σ. A procedure needs to be defined for determining values for the parameters of the observed data to apply these models for density estimation.

An inherent limitation of a parametric approach is the assumption that there is a specific distribution function form. Non-parametric density estimation methods form a distribution that only depends on the size of the data set, where the model parameters control model complexity and not the form of the distribution.

Now, taking into account the complex fabrication parameter dependence from Table 7.1, a joint distribution function of measured performance metrics can be perceived as a complex combination of dependent variables. In relation to RF electrical parameter statistics, methods for analyzing amplitude and phase excitation errors in arrays assume Gaussian pdfs of errors, based on antenna fabrication tolerances [159, 160]. In [161], the Gaussian errors are assumed to be correlated in amplitude and phase, which changes the array gain pattern. However, the antenna array analyses do not take into account statistics related to the devices in the system chain. Here we include a part of the transmit chain, including the MMIC PA and transitions from the MMIC to the antenna, which can then be combined with antenna element variations. But first, let us analyze

the estimation of the MMIC data set in both parametric (Gaussian) and non-parametric (Kernel Density) cases.

7.4 Gaussian Statistics

The following uni-variate Gaussian distribution is found from the mean, μ, and the variance, σ^2, of the measured data:

$$f(x|\mu,\sigma^2) = \frac{1}{\sigma\sqrt{2\pi}} e^{-\frac{1}{2}(\frac{x-\mu}{\sigma})^2} \tag{7.3}$$

In the multi-variate case, μ becomes a k-dimensional mean vector and σ^2 becomes Σ, a $k \times k$ co-variance matrix, which for the bi-variate case reduces to:

$$\mu = \begin{pmatrix} \mu_X \\ \mu_Y \end{pmatrix}, \qquad \Sigma = \begin{pmatrix} \sigma_X^2 & \rho\sigma_X\sigma_Y \\ \rho\sigma_X\sigma_Y & \sigma_Y^2 \end{pmatrix}$$

where ρ is the correlation between x and y. In the example case discussed here, x is the $|S_{21}|$, while y is $\angle S_{21}$, X and Y represent samples. The relevant bi-variate function that follows is then:

$$f(x,y\,|\,\mu,\Sigma) = \frac{1}{2\pi\sigma_X\sigma_Y\sqrt{1-\rho^2}} \exp\Bigg(-\frac{1}{2(1-\rho^2)} \left[\frac{(x-\mu_X)^2}{\sigma_X^2} + \frac{(y-\mu_Y)^2}{\sigma_Y^2} - \frac{2\rho(x-\mu_X)(y-\mu_Y)}{\sigma_X\sigma_Y} \right] \Bigg) \tag{7.4}$$

The bi-variate uncorrelated ($\rho = 0$) Gaussian for the sample data from Section 7.1 is visually represented in Fig. 7.10 at 81 and 94 GHz. There are large portions of the two-dimensional space that bi-variate Gaussian estimation fails to describe accurately, even if correlation is introduced. This in turn means that a statistical analysis of a transmit array will result in antenna complex coefficients with a skewed mean, and consequently, inaccurate predictions of main beam and sidelobe variations due to MMIC variations.

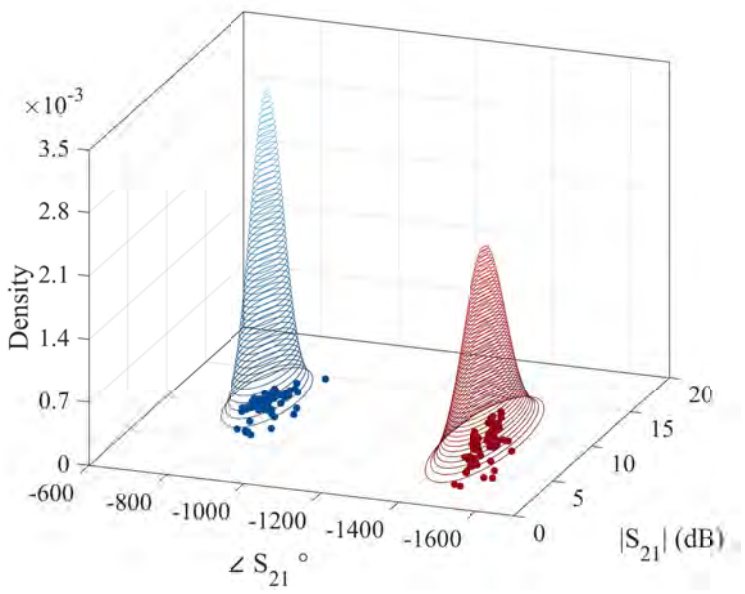

Figure 7.10: Bi-variate Gaussian distribution contours centered at the 1-D mean values with 1-D standard deviation values for both magnitude and phase of the measured MMICs at 81 (blue) and 94 GHz (red). The sample set at each frequency is scatter-plotted as well.

7.5 Kernel Density Estimation

To describe the measured data set better, we consider pdfs beyond simply Gaussians for an investigative description of measured MMIC data. Here we estimate the measured pdf using the kernel density estimator (KDE) [162]. To illustrate the difference from the Gaussian pdf, Fig. 7.11 compares a 1-D pdf for S_{21} at 81 and 94 GHz, showing that the Gaussian does not accurately capture uni-variate behavior. This exploratory data analysis reveals multi-modal, asymmetric distributions with frequency-dispersive behavior.

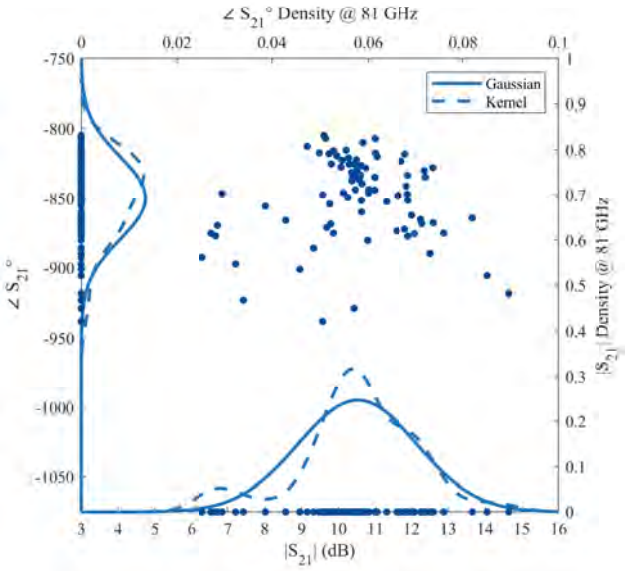

(a)

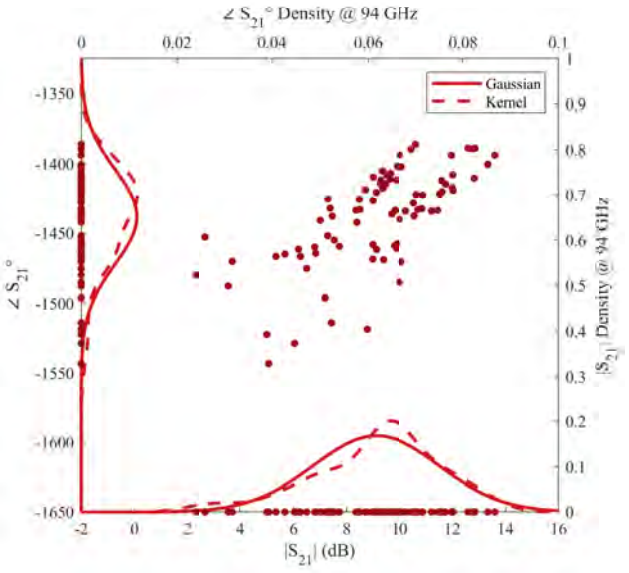

(b)

Figure 7.11: For both 81 and 94 GHz, the scatter plot shows the data set points. These are then shifted into a form of rug plot on each axis; where, both the Gaussian and the kernel density estimates are plotted in comparison. It is easy to see that the Gaussians do not accurately capture uni-variate densities.

When dimensionality is increased, correlation can be maintained as follows. Let $\{X_1, Y_1\}, ..., \{X_{83}, Y_{83}\}$

be a 2-D vector sample from the measured data at a single frequency, with a pdf $f_d(x)$, where x has a general dimensionality of value d. The true uni-variate and bi-variate densities can be estimated such that $\hat{f}_d(x)$ accurately approximates the marginal or joint distributions. The kernel density estimator is defined as

$$\hat{f}_d(x|H) = n^{-1} \sum_{i=1}^{n} K_H(x - X_i) \tag{7.5}$$

where K_H is a normalized continuous, uni-modal and symmetric kernel function. H is a symmetric, positive definite matrix of smoothing parameters, with dimension d, referred to as the bandwidth in this context. The kernel scales with H as follows:

$$K_H(x) = |H|^{-1/2} K(H^{-1/2}x) \tag{7.6}$$

where $|H|$ is applied to x and the kernel is normalized to this smoothing. The scaled kernels are then summed and normalized by the data set size n. For multi-variate data sets, the Gaussian kernel is a popular choice. The scaled and translated version becomes:

$$K_H(x - X_i) = (2\pi)^{-\frac{d}{2}} |H|^{-\frac{1}{2}} e^{-\frac{1}{2}(x-X_i)^T H^{-1}(x-X_i)} \tag{7.7}$$

which is centered at X_i and with variance matrix H, which needs to be determined when the pdf is unknown. One method to do this is unbiased cross validation (UCV), which is a 'leave-one-out' cross-validation method where the estimated pdf is evaluated against an estimate of the same data minus one sample [163, 164]. The extended method of smoothed cross-validation (SCV) has shown promise in reducing large variability in UCV by improving estimation of the integrated squared bias [165]. The multi-variate extension of SCV has been explored by Duong [162]. This work uses an unconstrained SCV in 1, 2, and 4 dimensions. Table 7.2 shows the values found for the uni-variate and bi-variate cases $\hat{\mathrm{H}}_{\mathrm{SCV}}$

Table 7.2: Unconstrained SCV Bandwidth Selection

	Magnitude (1-D)	Phase (1-D)	Both (2-D)
f_1	$H_M = \begin{bmatrix} 0.45 \end{bmatrix}$	$H_P = \begin{bmatrix} 10.17 \end{bmatrix}$	$H_2 = \begin{bmatrix} 0.35 & -2.24 \\ -2.24 & 155.76 \end{bmatrix}$
f_2	$H_M = \begin{bmatrix} 0.72 \end{bmatrix}$	$H_P = \begin{bmatrix} 11.76 \end{bmatrix}$	$H_2 = \begin{bmatrix} 0.77 & 4.47 \\ 4.47 & 176.06 \end{bmatrix}$

where f_1 is 81 GHz and f_2 is 94 GHz. Fig. 7.12 is the result of the kernel density estimation applied to the measured MMIC data set for 81 and 94 GHz. A scatter of the 83 sample points is plotted on top of filled contours of the 2-D joint density estimate. Shown in the sides of the image are the marginal density estimates. For an improved statistical analysis with an increased data set, standard sampling methods are applied, as described next for completeness.

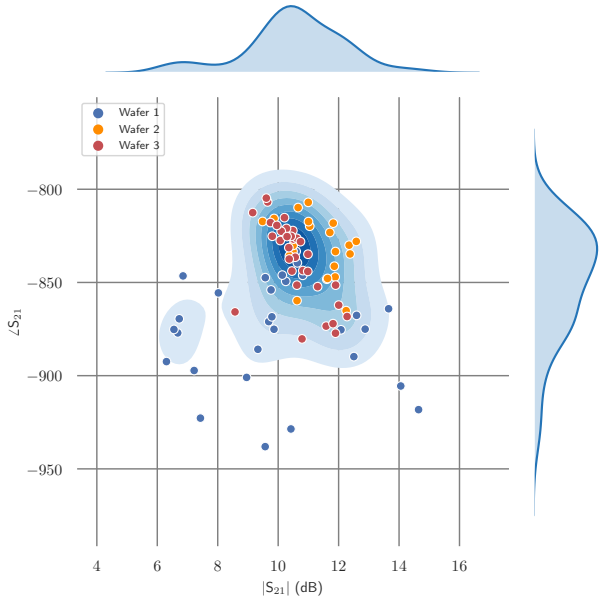

(a)

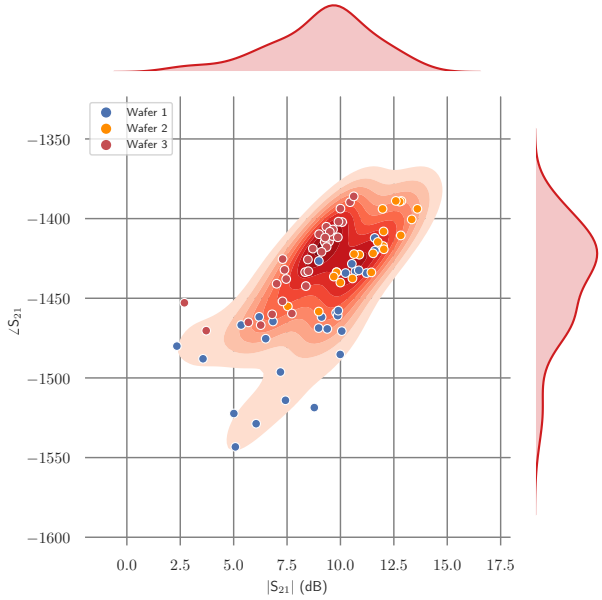

(b)

Figure 7.12: Uni-variate and bi-variate kernel pdf estimates for small-signal gain of 83 measured MMICs from three wafers at (a) 81 and (b) 94 GHz. A conclusion that can be drawn is that wafer-to-wafer data can differ significantly. In this case, wafer 1 shows a larger variance than the other two.

7.6 Conclusions

This chapter presents a novel statistical analysis for W-band MMICs designed in an experimental 90-nm GaN-on-SiC process. The analysis starts from measured on-wafer S-parameters for about 80 power-combined amplifier chips. Probability density functions, both parametric (Gaussian) and non-parametric (kernel density estimation), are generated from measured data. The analysis shows that the kernel estimation best desribes the data due to the unknown multitude of fabrication process variations. The results from this chapter are published in [53].

Chapter 8

Cascaded MMIC Statistics for Array Analysis

Contents

A cascaded matrix approach allows extension of the kernel estimation described in the previous chapter to additional components in the transmit chain that might contribute to variations, such as antenna element fabrication tolerances, driver amplifier gain variations, etc. Fig. 8.1 shows an example of a packaged MMIC in a waveguide which will be used to showcase the analysis. Markov chain Monte Carlo (MCMC) methods are applied and the aim of this KDE and MCMC combination is to create simulated data that can extend the analysis to include the MMIC package and antenna elements of a transmit array.

Another possible use of the presented analysis is in calibration of large phased array, especially

at millimeter-wave frequencies where MMIC process variations often require pre-testing of the die, e.g. [8, 166]. Most calibration techniques require a setup that provides high degree of phase and amplitude accuracy and necessary functionality in beamforming architectures to apply fine calibration resolution [167–169]. The analysis here can provide insight into the need for pre-testing of PAs, given a range and accuracy of available phase shift and variable gain required for correction in the calibration steps. Advance knowledge of the gain amplitude and phase can inform the decision related to costly pre-selection of MMICs, or the need for bias control across the transmit array, which will affect the EIRP.

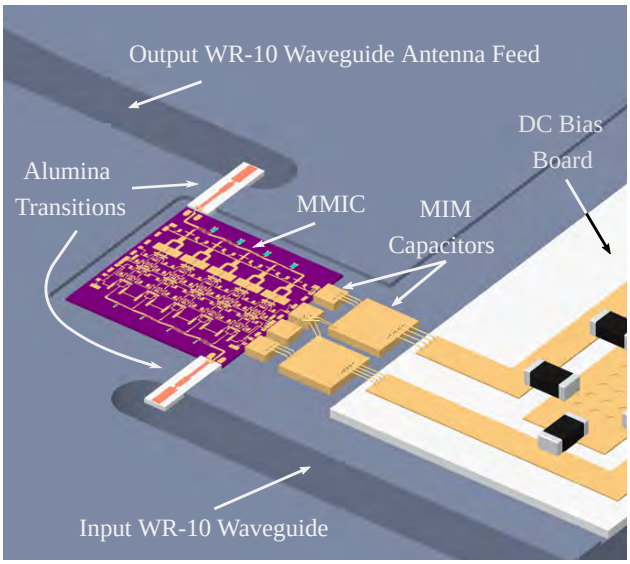

Figure 8.1: Image of W-band MMIC PAs with bias circuit, microstrip-to waveguide alumina transitions and input/output WR-10 waveguides. Fig. 4.2 is repeated here for clarity.

8.1 Markov Chain Monte Carlo

Markov chain Monte Carlo (MCMC) methods repeatedly sample a multi-dimensional continuous random variable from a target probability distribution $\pi(x)$. Ideally, these samples are independent and identically distributed (iid). Repeated MCMC iid sampling constructs a Markov chain with a distribution $\pi(x) = \hat{f}(x)$ determined by the kernel density estimates established in the previous

section. The Metropolis-Hastings MCMC algorithm is used here in context with KDE.

MCMC methods have a few disadvantages that are specifically important for this analysis: (1) the draws are locally correlated; and (2) the Markov chain needs significant simulation time to converge to the target distribution. The draws are correlated through the Markov process. Sets of nearby draws are correlated with each other and do not correctly reflect the target distribution, while over the long term the draws do. We choose a "jumping-width" of 5 draws with a single long chain to reduce auto-correlation and to reduce simulation time. Convergence means that the Markov chain has settled to the stationary distribution. The "burn-in" period of initial draws might follow a drastically different distribution and is typically discarded.

A result of this sampling algorithm for the one-dimensional cases with the first 1000 draws discarded can be seen in Fig. 8.2. The kernel density estimates of the original data set and the MCMC sample set show better agreement as the iterations of the MCMC are increased, allowing for a sufficient "tour" of the target density and tighter convergence.

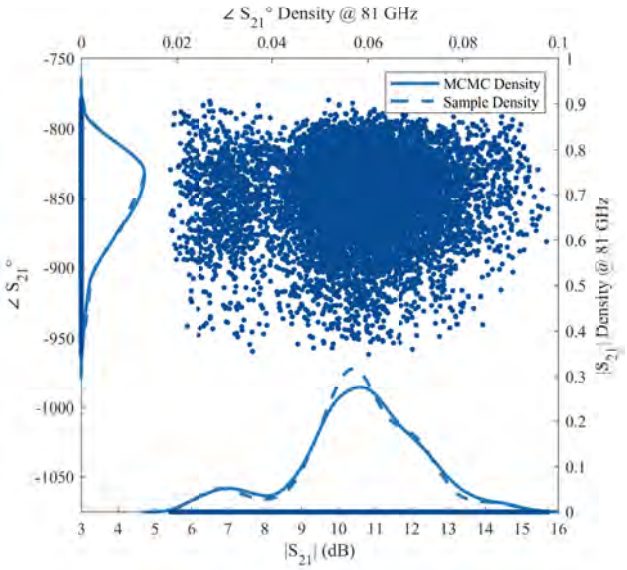

(a)

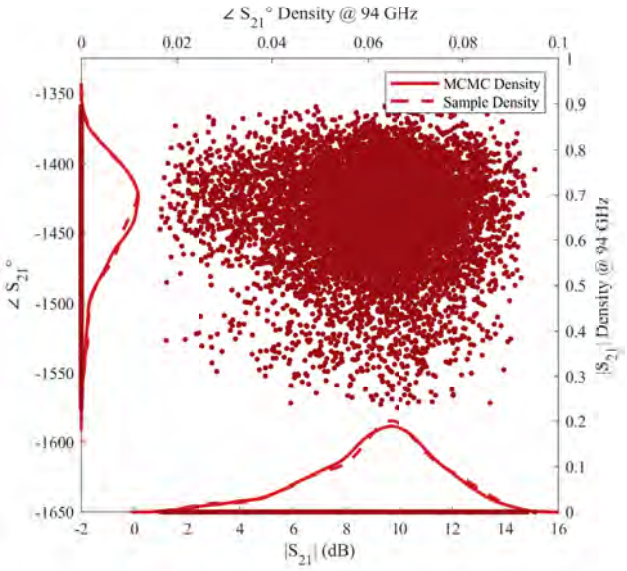

(b)

Figure 8.2: The uni-variate (magnitude and phase) MCMC draws are plotted in scatter, underneath are the uni-variate kernel density estimates. The dashed lines are the data set kernel density estimates as seen in Fig. 7.11 and the solid lines are the 1-D kernel density estimates of the MCMC results. Plotted are 10000 draws with the first 1000 draws discarded as a "burn-in" time.

Algorithm 1: Uni-variate Metropolis-Hastings

Data: A kernel-density estimated uni-variate density $\hat{f}(x)$
Result: Markov chain of unique independent and identically distributed draws as X

Initialize:
Choose proposal density $\sim q(x)$
Choose an arbitrary point x_0^i

for *iterations = 1,2...N* **do**
  Propose: $x^{\text{cand}} \sim q(x^i|x^{i-1})$
  Acceptance probability: $\alpha(x^{\text{cand}}|x^{i-1}) = min\{1, \frac{q(x^{i-1}|x^{\text{cand}})}{q(x^{\text{cand}}|x^{i-1})} \frac{\hat{f}(x^{\text{cand}})}{\hat{f}(x^{i-1})}\}$
  $u \sim Unif(0,1)$
  if $u < \alpha$ **then**
    Accept: $x^i = x^{\text{cand}}$
    Set: $X(i) = x^i$
  else
    Reject: $x^i = x^{i-1}$
  end
end

8.1.1 The Metropolis-Hastings Algorithm

The Metropolis-Hastings algorithm is used here for the estimation and sampling by creating a Markov chain though a series of accept-reject steps, as described in Algorithm 1 [170]. This algorithm randomly attempts movements in the parameter space, occasionally accepting moves or lingering in the same state. The acceptance ratio α demonstrates how probable the new proposed state is in relation to the current state, with respect to the target distribution. Movements that are more probable than the current state will consistently be accepted. However, if a movement is less probable, a rejection might occur, and as the relative drop in probability increases, the proposed state is rejected with a higher likelihood.

A common choice for the proposal distribution is a symmetric distribution $q(x^i|x^{i-1}) = q(x^{i-1}|x^i)$. Some standard symmetric proposals are Gaussian or uniform distributions centered at the chain's current state. The symmetry cancels out the effects of the proposal density, resulting in an acceptance ratio $\alpha(x^{cand}|x^{i-1})$ that is proportional to how likely the current state, x^{i-1}, and the proposed state x^{cand} are under the full joint density distribution. As the number of dimensions increases in the target density, the proposal acceptances need to be optimal for all dimensions simultaneously

to avoid excessively slow convergence.

The Metropolis-Hastings algorithm requires two initialization constraints: an arbitrary starting point and a proposal distribution. For simulations here, dependent symmetric uni-variate and bi-variate Gaussian proposal densities are used, with variance found from the data set statistics, as seen in Section 7.4. A proposal variance that is dependent on the original data set is found to have a positive effect on convergence time for individual dimensions as well as overall convergence.

With multi-variate distributions, the algorithm requires a multi-dimensional initial point and multi-variate joint proposal distribution of the same dimensions. The KDE is now evaluated across a N-dimensional (N-D) grid and the acceptance ratio for the proposed N-D candidate states is calculated using N-D interpolation between meshed vertices. The benefit of a bi-variate Metropolis-Hastings algorithm is apparent in Section 7.5. The bi-variate density maintains properties of dimensionality, such as parameter correlation, that would otherwise be removed by reducing to the uni-variate densities. This can be seen by a closer comparison of Fig. 8.2 and Fig. 8.3.

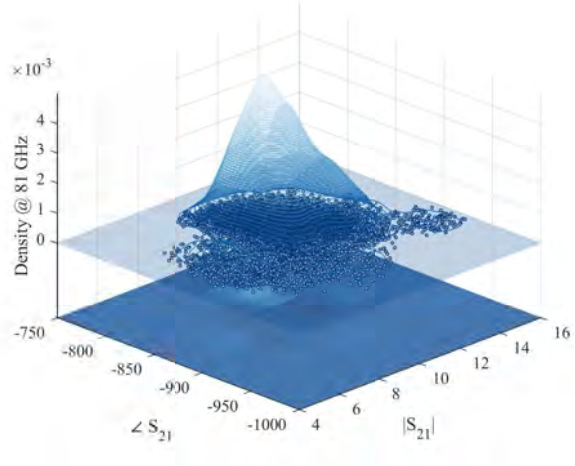

(a)

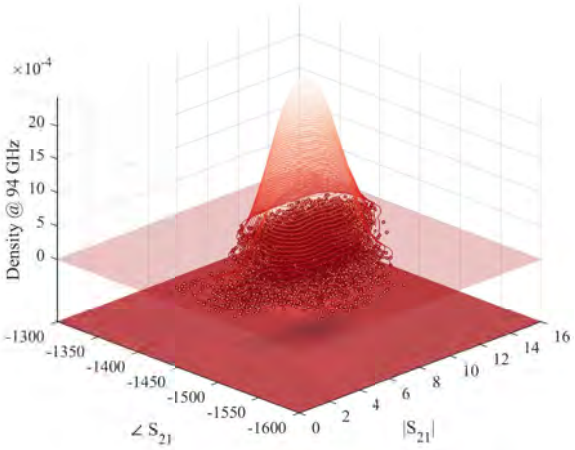

(b)

Figure 8.3: The bi-variate MCMC draws are plotted in scatter underneath 3-D contour plots of the bi-variate kernel density estimates. Underneath this 3-D plot is the relative error between bi-variate sample density estimate and the MCMC density estimate. The intensities of dark and light show spots where the MCMC either overestimated or underestimated respectively. Of the simulation, 10000 draws are plotted with the first 1000 draws discarded as a "burn-in" time.

Another interesting comparison seen in Fig. 8.2 and Fig. 8.3 is the difference between the original data and MCMC samples when plotting the kernel density estimates of both. It has been shown

that the MCMC rejection step introduces changes in the estimates of the bias and variance [171]. In the estimated pdf of the MCMC samples, regions can significantly deviate from the original data; and as such, this comparison does not necessarily show that the samples are drawn from the correct pdf. To identify that the MCMC has correctly drawn from the stationary distribution, Section 8.1.2 describes various metrics for convergence of the MCMC to the stationary distribution.

There are other Monte Carlo methods that have benefits for sampling with higher convergence efficiency and high-dimensionality but come with more implementation complexity; these however, are not explored further in this work. If readers would like to do such exploration, other current methods worth studying include the Gibbs Sampler [172], the Metropolis-adjusted Langevin Algorithm [173–175], the Multiple-try MCMC [176], Reversible-Jump [177], and the Hybrid ('Hamiltonian') Monte Carlo [178].

8.1.2 MCMC Convergence Metrics

There are different ways to test for MCMC convergence. Traceplots can show if the parameters are "mixing" well, defined as moving around the parameter space efficiently. Alternatively, autocorrelation on the Markov chains should display a drop in magnitude as the lag increases. These can show potential for convergence of a single chain, but do not produce rigorous criteria for determining convergence for an estimated pdf.

Gelman and Rubin created a convergence metric that looks at inferences from m simulated Markov chains and compares these to inferences made by combining n draws from all sequences [179]. To do this, the average of the m within-sequence variances is initially calculated as

$$W = \frac{1}{m(n-1)} \sum_{j=1}^{m} \sum_{t=1}^{n} (\theta_{jt} - \bar{\theta}_{j.})^2 \tag{8.1}$$

where θ_{jt} is the sample point, and $\bar{\theta}_{j.}$ is the average over the draws (t). The variance B/n between the m sequence means is calculated as

$$\frac{B}{n} = \frac{1}{m-1}\sum_{j=1}^{m}(\bar{\theta}_{j\cdot} - \bar{\theta}_{\cdot\cdot})^2 \tag{8.2}$$

where $\bar{\theta}_{\cdot\cdot}$ is the average over the entire set of chains. Then, an estimate of the variance of the stationary distribution as a weighted average of W and B is formed:

$$\hat{\sigma}^2 = \frac{n-1}{n}W + \frac{B}{n} \tag{8.3}$$

Lastly, the potential scale reduction factor ($\hat{R}$) is calculated as

$$\hat{R} = \sqrt{\frac{(m+1)}{m}\frac{\hat{\sigma}^2}{W} - \frac{n-1}{mn}} \tag{8.4}$$

which reduces to 1 as $n \to \infty$. A large $\hat{R}$ suggests that either the estimate of the variance $\hat{\sigma}^2$ can be further decreased by more simulations, or that further simulation will increase W, since the simulated chains have not made a full route of the target distribution. On the other hand, if $\hat{R}$ is close to 1, it can be concluded that each of the m sets of n simulated observations is close to the target distribution.

An extended metric for the multi-variate case can be found in [180]. W and B/n denote within- and between-sequence covariance estimate matrices in d dimensions, respectively. $\hat{V}$ becomes the estimate of the posterior variance-covariance matrix and $\hat{R}$, the multi-variate $\hat{R}$, is determined as a scalar measure of the distance between $\hat{V}$ and W. Fig. 8.4 shows $\hat{R}$ as function of the chain iteration for the the amplitude and phase of the MMIC gain at 81 and 94 GHz, as well as the uni-variate, bi-variate, and 4-dimensional cases (as needed in Section 8.2). $\hat{R}$ quickly drops to 1 for all parameters and it can be concluded that the m chains are each close to the target distribution. A burn-in time is set as a threshold; when $\hat{R}$ is below this threshold, the draws can be taken as independent and identically distributed.

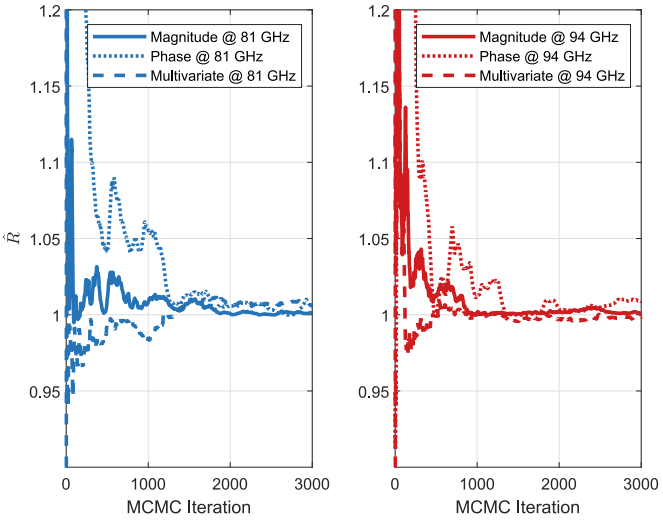

Figure 8.4: The Gelman and Rubin's diagnostic of potential scale reduction factor as it changes through the MCMC iterations. Ideally, the chains converge to 1; after reaching below a certain threshold for $\hat{R}$, typically it is said to be converged. This metric relays a solid value for "burn-in" time, approximately here would be 1000 draws.

Other metrics do exist for determining MCMC convergence; for the extent of this research, they are not explored further. Among these are the Geweke diagnostic [181], the Raferty and Lewis diagnostic [182], the Heidelberg and Welch diagnostic [183], and the Yu and Mykland diagnostic [184].

8.1.3 MMIC-Microstrip-Waveguide Transition

At this point, we have a good statistical representation of W-band MMIC PA gain variation across several wafers. The MMICs are next combined in a spatial power combining array of waveguide horn antennas. The transition from each MMIC to a WR-10 rectangular waveguide is then analyzed with its fabrication- and mounting-related parameter spread.

A review of millimeter-wave waveguide transitions with various techniques is shown in Section 4. The design used here, seen in Fig. 8.5, is presented in Section 4. One wave-port excites the microstrip

on the MMIC, while the other is the WR-10 waveguide in the split-block configuration seen in Fig. 8.1.

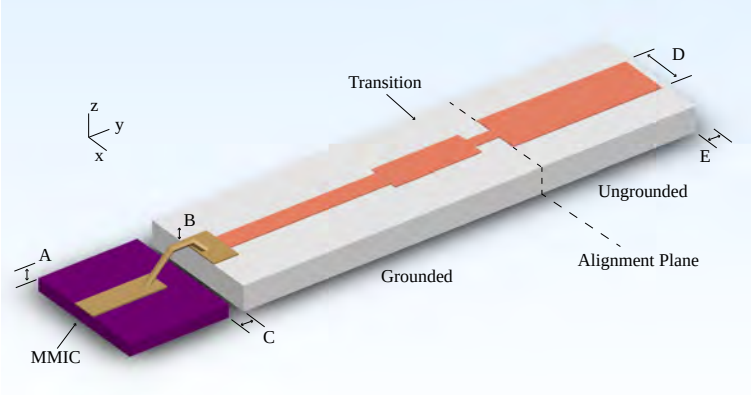

(a)

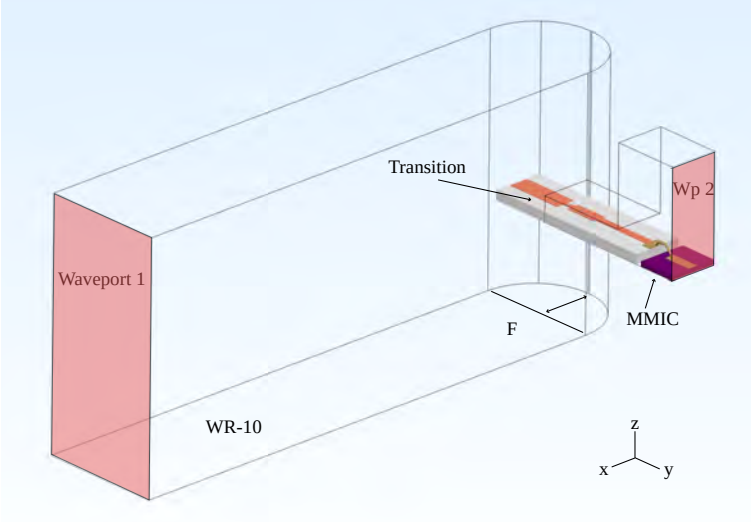

(b)

Figure 8.5: A W-band MMIC-to-waveguide transition, simulated in HFSS, consists of a copper-metallized alumina probe and a 25 μm gold bondwire. Six parameter sweeps are generated where in (a) A, B, C, D, E correspond to copper pedestal height underneath the MMIC, bondwire height, gap between MMIC and alumina, typical tolerance of metallization, and placement into the waveguide, respectively, and in (b) F is the backshort distance due to CNC machining tolerance.

As seen in Section 4, the nominal design shows less than 1 dB of insertion loss across W-band. However, a large amount of variability is introduced by fabrication and mounting. A linear param-

eter sweep covering 6 variable dimensions was performed; these are labeled in Fig. 8.5. In Fig. 8.5a, A, B, C, D, E correspond to the copper pedestal height underneath the MMIC, the bondwire height, the gap between MMIC and alumina, the typical tolerance of metallization ($\pm$ 5 μm), and the placement in the waveguide, respectively. In Fig. 8.5b, F is the back-short distance due to CNC machining tolerance. All of these parameters have units of μm and do not vary more than 0.5 mm.

The result of the large parameter sweep on the transmission coefficient is seen in Fig. 8.6. The worst-case transmission is up to -5 dB for the largest deviation in dimensions, with more sensitivity to C compared to other dimensions. The average value is centered around -3 dB with a standard deviation of about 1 dB. Lost in these Gaussian statistics, but seen in the regions of tightly spaced thin purple lines of Fig. 8.6, is that the transmission coefficient is not equally affected by the A-F dimension variations at all frequencies. This indicates that the transition analysis can also benefit from the density estimation and sampling presented in Sections 7.5 and 8.1.1.

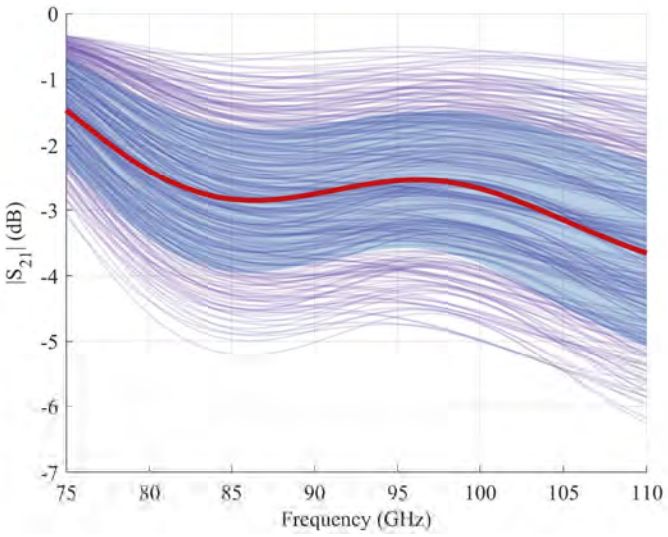

Figure 8.6: Simulated parametric sweep of $|S_{21}|$ of the W-band transition, for dimensions [A,B,C,D,E,F] varied between [5:60 μm, 25:65 μm, 10:110 μm, -5:5 μm, -10:10 μm, 876:926 μm]. Plotted is the mean value in red, one standard deviation in blue fill, and all sweeps in thin transparent purple lines.

8.2 Statistics of Cascaded RF Components

Now, we have two separate cascaded statistically-described networks: the amplifier S^a and the transition S^b. From [185], this cascaded network is a single 2-port block, S^c, given by:

$$\begin{bmatrix} S^c_{11} & S^c_{12} \\ S^c_{21} & S^c_{22} \end{bmatrix} = \begin{bmatrix} S^a_{11} + \kappa S^a_{12} S^a_{21} S^b_{11} & \kappa S^a_{12} S^b_{12} \\ \kappa S^a_{21} S^b_{21} & S^b_{22} + \kappa S^b_{12} S^b_{21} S^a_{22} \end{bmatrix}$$

where

$$\kappa = \frac{1}{1 - S^a_{22} S^b_{11}} \tag{8.5}$$

It should be noted that S^c_{21} is a combination of four complex parameters (eight variables), two from each network. The bi-variate S^a_{21} is estimated and sampled in Fig. 8.3 and Section 8.1.1. The other three complex parameters could be done in the same manner; however, separating these S-parameters would remove any within-network correlation structures.

The linear transition network, S^b, is physically symmetric and reciprocal; while creating the statistical data set, passivity under these assumptions is maintained. However, the amplifier matrix, S^a, has an unknown correlation between gain and output match, which affects the sampling. For each two-port network, the inter-dependence of the S-parameters implies a cross-correlation requiring a higher-order model, which is an expansion of the bi-variate to a multi-variate distribution, in this case to four dimensions. The estimation and sampling algorithm is run once for each network, while the correlation between $[S^a_{21},\ S^a_{22}]$ and $[S^b_{21},\ S^b_{11}]$ is maintained. Random variables X for S^a and Y for S^b can be estimated and sampled in 4-D.

A resulting final cascaded S^c_{21} equation containing the two random variables, X and Y, where each sample point consists of four dimensions and is given by

$$Z_{S^c_{21}} = \frac{(X_{R(S^a_{21})} + iX_{I(S^a_{21})})(Y_{R(S^b_{21})} + iY_{I(S^b_{21})})}{1 - (X_{R(S^a_{22})} + iX_{I(S^a_{22})})(Y_{R(S^b_{11})} + iY_{I(S^b_{11})})} \tag{8.6}$$

The resulting random variable Z is a complex parameter consisting of the same number of samples drawn from each MCMC chain. One such combination is presented in Fig. 8.7.

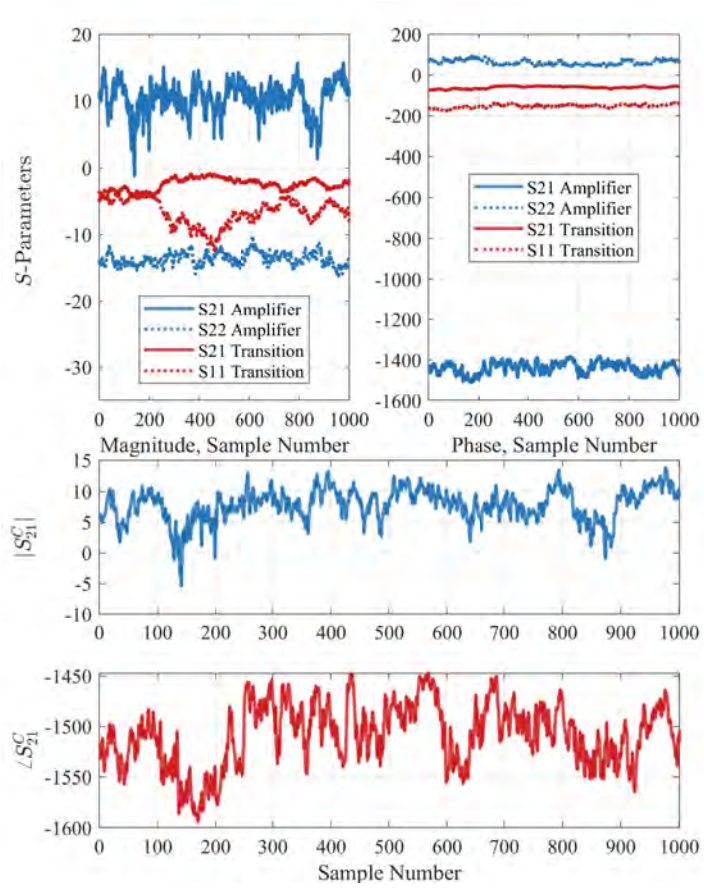

Figure 8.7: Two separate simulated 4-dimensional Markov chains for both the power amplifier and transition networks. Top-left plot is of the magnitude of the parameters, top-right plot is of the wrapped phase of the parameters, and the bottom plot is of the cascaded network S_{21}^c.

8.3 Example Case: Sub-Array Horn Antenna Application

A cascaded statistical description is next applied to a 16-element transmit antenna array. We use a 4×4 array as it is the smallest two-dimensional array that is used often as a sub-array to validate performance and indicate potential scaling to a larger array. The block diagram showing relevant components is given in Fig. 8.8. Classical antenna array tolerance analysis, e.g. [159,186], calculates

the array factor based on random variations in amplitude and phase with a normal probability density function and statistically independent errors. The array errors that are considered in these analyses are due to small variations in current excitations from the mechanical imprecision in the antenna elements. To extend to a multi-variable analysis in 2D arrays, Monte Carlo methods are proposed in [187]. Further, interval analysis which computes the bounds of a linear antenna array response by modeling bounds on the complex excitation is studied in [188, 189]. In these works, 20-element and larger arrays are analyzed using ideal sources and isotropic antenna elements. Here we extend the classical analysis to include measured PA variations.

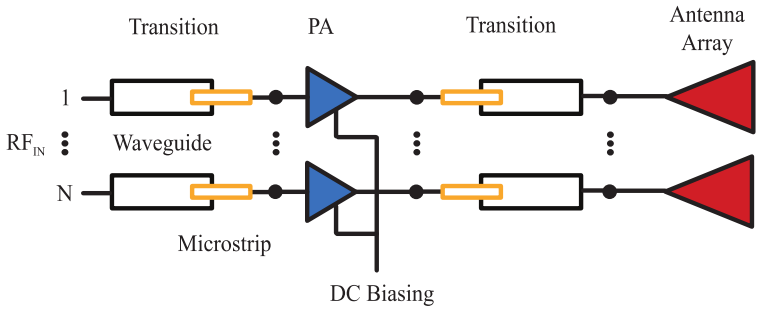

Figure 8.8: Block diagram of the final transmit stage analyzed in Section VII.

The antenna element used as an example in the simulations is an E-plane square-aperture W-band horn fed by WR-10 waveguide feeds. The array, shown in Fig. 8.9, is designed for fabrication with split-block machining in 5 parts stacked in the x direction. The antenna array is simulated in Ansys HFSS. The simulated VSWR over the band for the 4 elements in each quadrant is shown in Fig. 8.10 when all elements are fed in-phase with equal amplitudes.

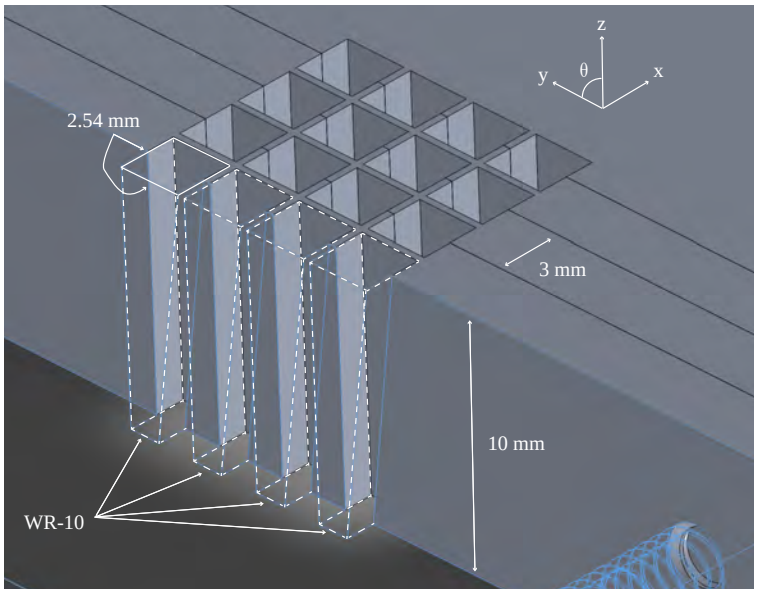

Figure 8.9: 16-element horn array with detail of E-plane horn element. The element spacing is roughly 0.5 mm.

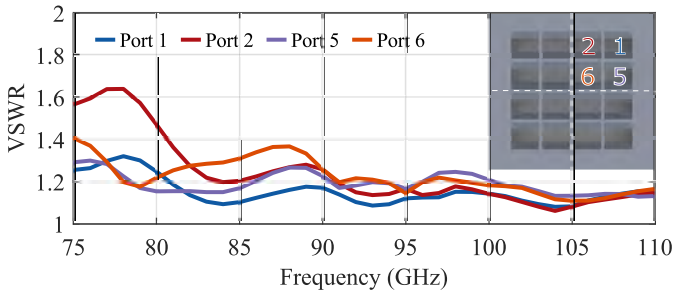

Figure 8.10: Simulated VSWR of the horn antenna plotted over frequency.

The array factor is classically given by

$$AF(u,v) = \sum_{m=1}^{M}\sum_{n=1}^{N} W_{mn} e^{j\phi_{mn}(u,v)} \tag{8.7}$$

but in this case, the complex excitation W_{mn} is a statistical quantity that has the joint distribution as estimated in the previous chapter with $\hat{f}_d(x)$. This means that the radiation pattern of the array will also be a statistical quantity made of the cascaded samples of the MMIC and transition to waveguide, assuming the antenna elements are ideal. It is computed by adding the independent far

field patterns from all 16 elements previously extracted from simulations. Using a 1000 sets of 16 samples of the S_{21}^{c} cascaded vector, the descriptive statistics of the broadside pattern is shown in Fig. 8.11 - 8.13. The ideal array gain pattern is plotted in dashed black line, while all of the 1000 Monte Carlo simulations are shown in thin purple lines with their mean shown in solid red. The shaded blue region represents one standard deviation away from the mean. Some conclusions from Fig. 8.11 a are: (1) the mean value of the sidelobe is about 1.5 dB higher than that of the ideal sidelobe level; (2) the increased value of the mean is not symmetrical; (3) the main beam is roughly at the same level as in the ideal case; and (4) the variance in the main lobe is smaller than in the sidelobes.

It is interesting to see the effects of different pdfs on the asymmetry in the sidelobe level for the broadside E-plane gain. Fig. 8.12 compares Gaussian, bi-variate and cascaded cases from Sections 7.4, 7.5, and 8.2. For the Gaussian and bi-variate cases, the nominal value of the alumina transition is used. In the Gaussian case, the mean performs close to ideal and affects the main beam and sidelobes equally. The bi-variate KDE samples show similar behavior, but with slightly higher values. However, the cascaded draws result in an asymmetry, where one sidelobe is around the same as the bi-variate case while the other is 1.5 dB higher.

Using the main beam deviations for a broadside E-plane cut, the 3dB beamwidth is investigated in Fig. 8.13 a. The median value of the cascaded is roughly 0.3 degrees smaller than the bi-variate and Gaussian cases. The cascaded set shows a large positive skew, with the majority of 3-dB beamwidths are smaller and below 14°. The bi-variate case shows a larger interquartile range (width of boxed region) than the Gaussian, with a slightly lower median and a slight positive skew towards the smaller beamwidth.

In Fig. 8.13 b, beam pointing error is calculated as the difference between the maximum values of the ideal case and the various pdfs. Interestingly, the cascaded case shows a preference for a specific direction and the median is centered around 0.1°. This positive skew can be seen as well in the colored violin plots. In the bi-variate case, the median is centered at 0°, however, the interquartile range is larger than for the Gaussian and appears to have more outliers that extend

beyond 3° of beam pointing error. For both boxplot images Fig. 8.13 a and b, the whisker maximum and minimum are set to a default of 1.5 interquartile range.

The analysis shows that an accurate prediction of antenna radiation pattern characteristics requires taking into account the statistical dispersion of the amplifiers and transitions, especially at W-band where process-related variations can be high. For a 16-element spatial power combining array, the first sidelobe level can vary ±6 dB and the EIRP by ±3 dB when random amplifier chips from the measured batch are chosen to populate the array.

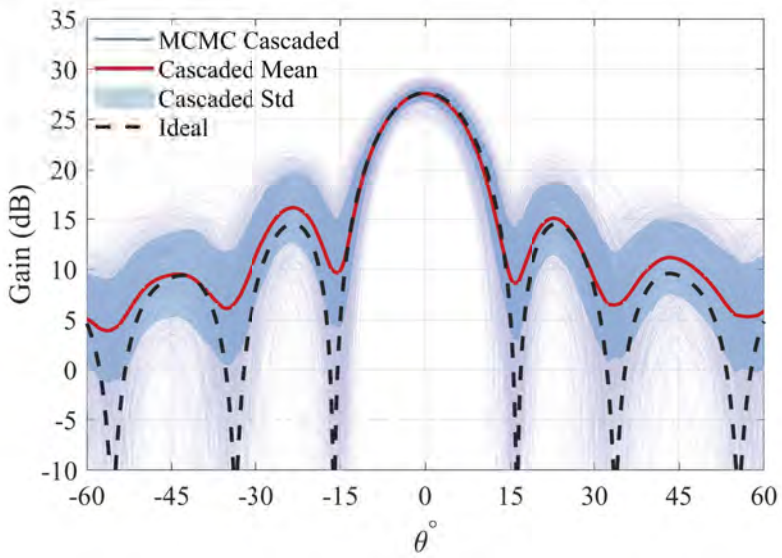

Figure 8.11: Ideal radiation pattern of the array (dashed line), with cascaded statistical mean and standard deviation shown for comparison for broadside.

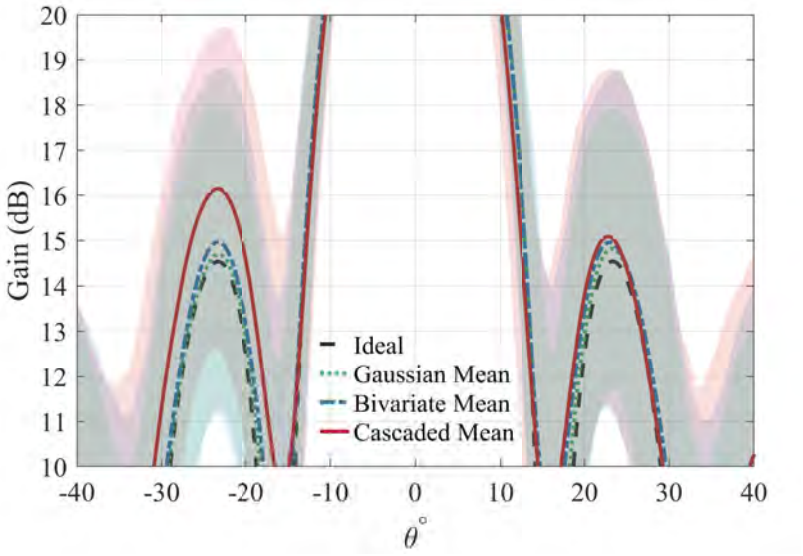

Figure 8.12: Broadside gain comparison for an ideal ideal antenna array excitation and the means of the various statistics. The overlapping shaded areas are the corresponding regions of one standard deviation.

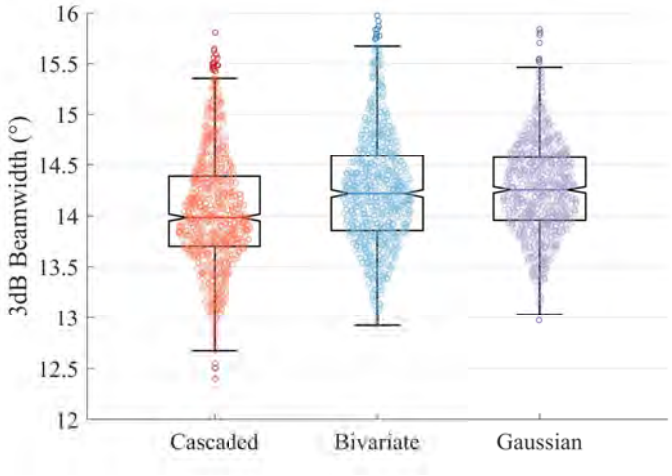

(a)

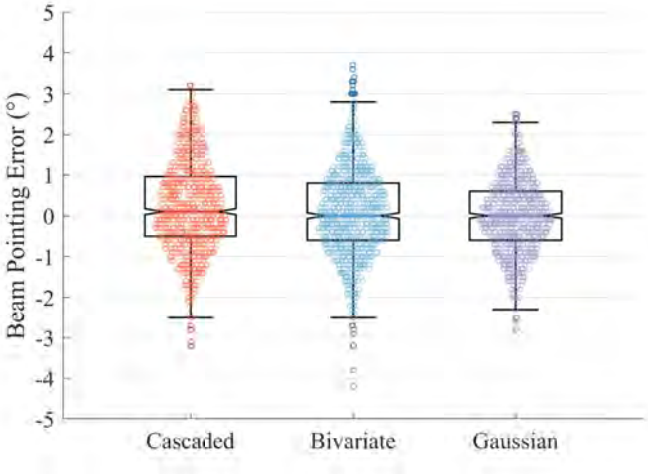

(b)

Figure 8.13: For a comparison of the various statistics, boxplots with overlaid violin-plots are shown for (a) 3-dB beamwidth and (b) pointing error variation for broadside.

8.4 Conclusions

Starting from the pdfs estimated in the previous chapter, a Markov chain Monte-Carlo method is applied to cascaded statistics of a transmit chain. The connection from the MMIC PAs to alumina microstrip-to-waveguide transitions are analyzed with full-wave simulations in conjunction with the same statistical approach. The analysis is given on cases of small-signal MMIC gain cascaded with

passive transitions with a simple Gaussian model, a bi-variate kernel density estimated model, and a model developed by using multi-variate S-parameters as complex random variables in a cascaded network. The waveguides feed a 16-element square horn array and the effect of cascaded statistics on EIRP is quantified. An extension to cascaded antenna fabrication tolerances is straightforward and follows the same methodology.

Furthermore, the knowledge of process variations and their correlated statistics can give an insight into the ability to calibrate a phased array without pre-testing and choosing MMICs, as has been done in many millimeter-wave transmit arrays. Calibration techniques require a high degree of phase and amplitude accuracy in the beamformer for acceptable calibration resolution, as can be seen in examples of narrowband arrays at Ku band (17.3–17.8 GHz) [190], relatively broadband Ka-band arrays (37–42 GHz) [191] and a 90.7 GHz 384-element array [192]. Advance knowledge of the gain amplitude and phase can inform the decision related to costly pre-selection of MMICs or the need for bias control across the transmit array. Improving the error on gain amplitude is especially important for narrowband transmit arrays, where bias control affects the efficiency and contributes to reduction in EIRP and increase in thermal stress. In broadband arrays, the phase variations in calibration become more critical, as does element-to-element coupling and active scan coefficient that takes into account variations in large-signal PA parameters. The results from this chapter are published in [53].

Chapter 9

Conclusions and Future Work

Contents

9.1 Thesis Summary

The focus of this thesis is to address design and packaging of high power W-band GaN-on-SiC MMIC PAs. First, passive rectangular waveguide 3D printed components are investigated.

In Chapter 2, a series of waveguide components are designed to test various capabilities of metallic additive manufacturing over different alloys, in particular of surface roughness and internal printing resolution of complex features, and between two techniques, metal-coated plastic and direct metal laser sintering. Waveguide designs for both V- and W-bands with straight waveguides, 20-dB couplers, and corrugated filters were made using HFSS. In Chapter 3, the designed waveguide structures from Chapter 2 were fabricated, measured, and analyzed for surface finish and feature resolution with respect to electrical performance and between two main alloys, AlMgSi10 and

maraging steel. Following this characterization, a waveguide-to-MMIC 3D circuit is designed using a GaAs MMIC process with backside processing to provide a broadband transition from waveguide to GaN MMIC PAs, described in Chapter 4. Due to the low available power densities at high frequencies, multiple levels of power-combining in W-band PAs are investigated in Chapters 5 and 6. Specifically, the design and analysis of two 3-stage W-band MMIC PAs with simulated output powers over 25 dBm is presented. These 'unit' amplifiers have device-level combining in the staging of the devices. Two and three of these 'unit' amplifiers are then combined at the circuit-level using different circuit combining techniques. All of the MMICs are measured and it was found that the output power is lower than simulated due to a processing issue that resulted in high current collapse [143], lower g_m and lower $I_{\max}$. Nevertheless, power levels up to 27, 24, and 18 dBm at 75, 92, and 110 GHz respectively were measured. In these advanced experimental processes, considerable variations across a wafer and between-wafers can occur. In Chapter 7, a statistical analysis for W-band MMICs designed in an experimental 90-nm GaN-on-SiC process is presented. The analysis starts from measured on-wafer S-parameters for about 80 power-combined amplifier chips. The analysis is extended to cascaded statistics of an array of transmit chains with spatial output power-combining upon radiation.

9.2 Future Work

Extending the work contained within this thesis, there are opportunities for additional improvements to existing analysis and setups as well as ongoing work that requires significant time for fabrication. These continuations are detailed in the following sections.

9.2.1 DMLS Printing Updates

In the time after the publication of [90], various metal alloys have been added to the list of materials for commercial machine printing. From the EOS materials website, there are few alloys that could potentially be promising to study for RF components in addition to AlSiMg10, MS1, IN625, and

GRCop-84 that were analyzed in Chapters 2 and 3. A deeper tradeoff between high conductivity and feature resolution with newer powders could be presented. A list of the alloys that might fit in this category are coppers CuCP or CuCrZr, tungsten W1, aluminum AlF357, titanium Ti64, and various steel alloys.

An analysis for a tighter correlation of component feature resolution to RF performance could be designed and presented with specific print tolerances in mind. Fig. 9.1 shows an FDM printed component for the sole function of evaluating printer quality. A similar one could be designed for DMLS alloy processes with respect to standard rectangular waveguide needs. Such an evaluation could provide insight in tolerance tradeoffs so that a designer can tailor components to avoid RF sensitive features with a higher probability of poor printing.

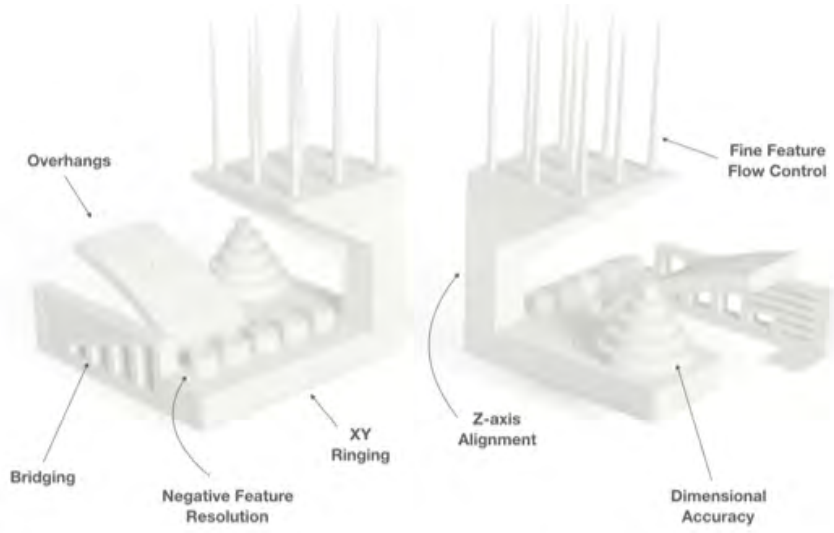

Figure 9.1: An image of a printed component to evaluate various issues with 3D printers [193].

9.2.2 3D Surface Roughness Profiling for Waveguide Loss Modeling

In previous work [90] and shown in Chapter 3, the correlation function for 3D surface roughness in direct metal laser sintered V- and W- band waveguide is found and root mean square height and autocorrelation lengths established for various metallic powders. [104–108] begin dealing with random surface roughness in 2D and 3D cases (as seen in Fig. 2.4) for dielectric and conductive

medium by using a second-order small perturbation method. The power spectral density (PSD) of a rough surface is equivalent to the fourier transform of the correlation function and this PSD is used to determine power loss.

Combining both this small perturbation method applied to rectangular waveguide and the measured surface characteristics could allow a direct correlation from measurements to waveguide power loss.

9.2.3 N-Device and Staging Combining Efficiency Study

An interesting avenue for future work is a more careful study of device size and staging ratio considering performance of different single device peripheries in comparison to power-combining in a stage. Fig. 5.2 shows that the power increases linearly with periphery when each device is presented with impedances and input powers that optimize its performance. This figure cannot be used for a straight-forward comparison because the saturation levels are different. An interesting study would be to fix the available input power, and present the optimal impedance to different device peripheries for e.g. PAE. In that case, for a fixed output power and known passive combiner loss, it is then possible to determine whether a small number of large devices or vice versa is optimal for overall efficiency. For example, referring to Fig. 5.3 where the input power is fixed at 17 dBm, the smaller device (4x25) has a maximum PAE of 27% at 92.5 GHz while the larger device (4x37.5) has a maximum PAE of 25% at the same frequency. To obtain the same output power over 31 dBm, one would need four devices of size 4x37.5 or eight devices of size 4x25. In this case, it would be more efficient to use the large devices due to less loss overall in the combining networks. This analysis could be extended to multiple stages in order to find optimal staging efficiency for a given set of device peripheries.

9.2.4 Six-stage W-Band Power Amplifiers

As a culmination of the PA design knowledge contained in this thesis, a 6-stage power amplifier was designed in the HRL T3 40-nm GaN HEMT (as detailed in Chapters 5 and 6) with the intent

of full W-band operation with an output power above 1 W. The design takes into consideration the ability to reach this performance with input power limitations of the driving stages as typical in W-band and probe station limitations for dc biasing. Fig. 9.2 show the layout of this power amplifier. Without the bond pads, the total area is $4150 \times 1350\,\mu$m. This PA consists of seven RF matching networks and eleven transistors with a total periphery of $4050\,\mu$m. The staging ratio is 1:2:4:4:8:8 where the first three stages were designed to be operated at +6 Vdd and the second three stages at +12 Vdd for more efficient operation. For increased power output, the device functions at +12 Vdd on all the stages.

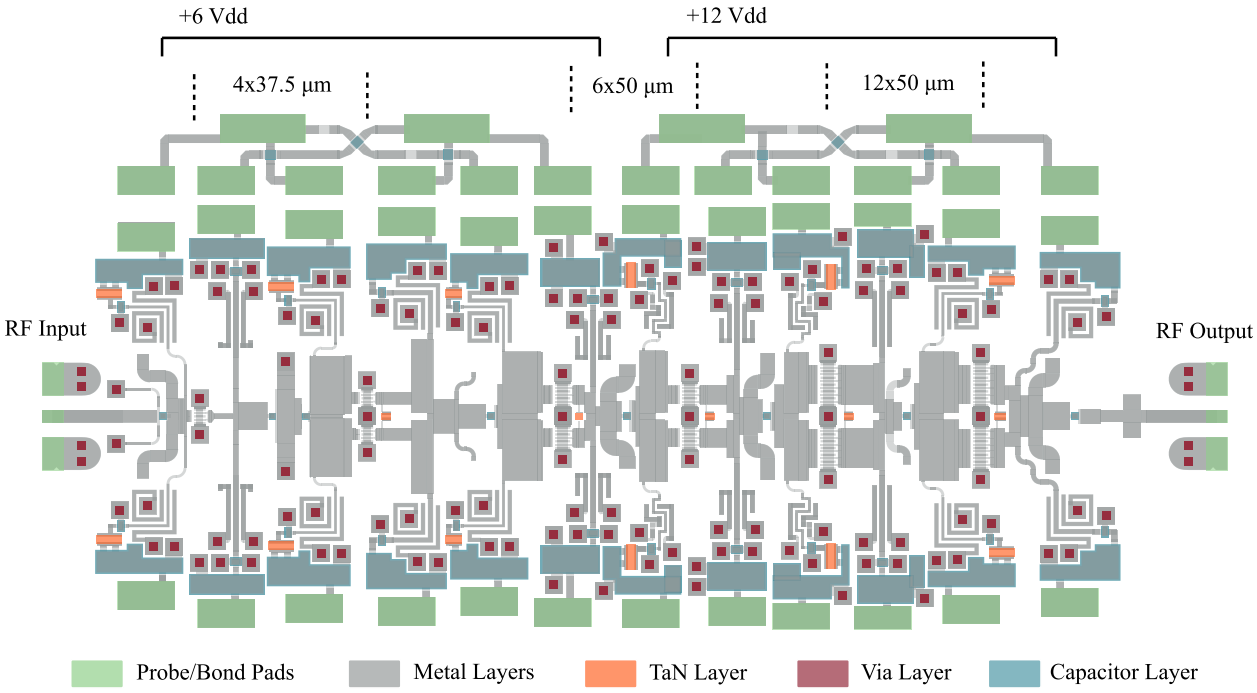

Figure 9.2: Layout of the 6-stage power amplifier with designations to the transistor sizing and drain bias.

Fig. 9.3 shows the relevant S-parameters ($|S_{11}|$,$|S_{22}|$, and $|S_{21}|$) and the P_{OUT}, PAE, and large-signal gain at P_{IN}=11 dBm. There is a slight 1 dB dip below 30 dBm (1 W) at roughly 95 GHz in the image, however, 30 dBm is reached with more input drive. The input and output matches show roughly better than 8 dB across most of the band. Saturated gain is roughly around 19 dB with small-signal gain up to 32 dB in the lower regions of W-band. PAE shows up to 17% at around

75 GHz and is above 5% across the entire band. Fig. 9.4 shows that the device begins to compress fairly evenly across the band around 8 to 11 dBm of input power.

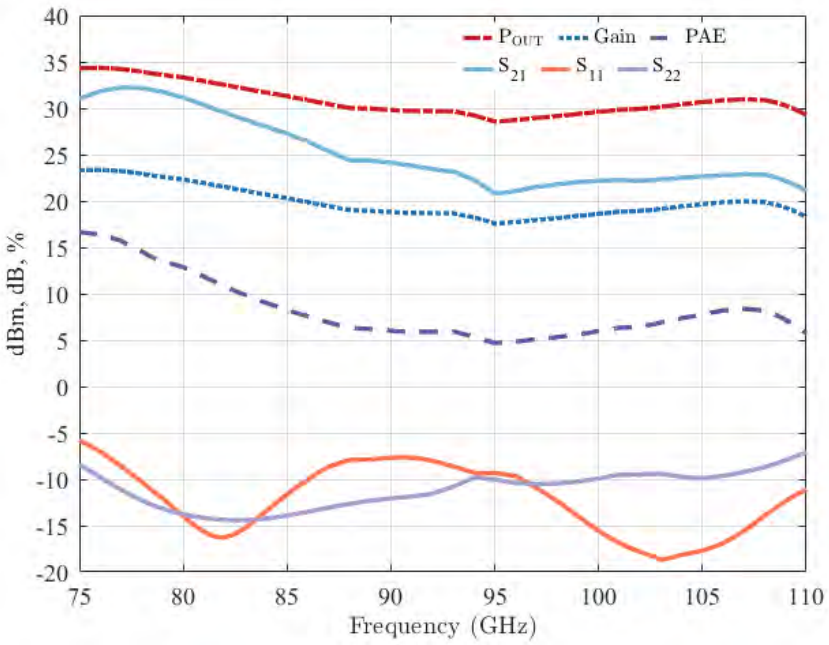

Figure 9.3: Small- and large-signal performance of the 6-stage PA over the W-band range with P_{IN}=11 dBm.

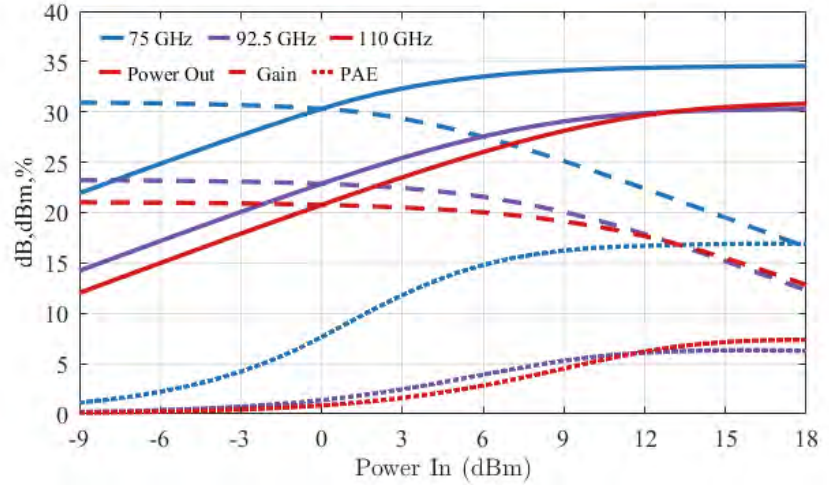

Figure 9.4: Drive-up characteristics of the 6-stage PA from -9 dBm to 18 dBm at the lower, middle, and upper regions of W-band.

Multiple stability analyses where also performed on this PA design as generally a device with high saturated gain has significant potential for positive feedback. The gain suppression of this device out-of-band is below 20 dB so lower frequency instabilities where not particularly concerning. Fig. 9.5a shows that linear Nyquist does not have an instability and Fig. 9.5b shows a large phase margin for the even-mode loop gain. Both Nyquist and even-mode loop gain show stability over source and load variation from 20 to 100 Ω. Odd-mode loop gain was not performed as the RF networks are too complicated to be effectively cut along the plane of symmetry. Instead, pre-emptive odd-mode resistors are placed on the drain side of each power-combined stage. As well, roughly 5 Ω resistors are placed in the gate biasing paths.

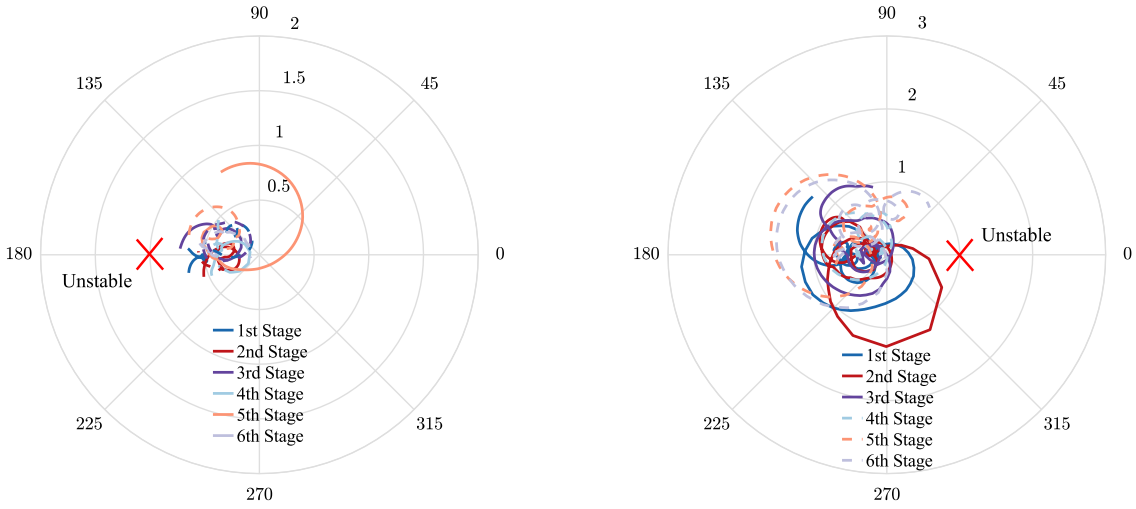

(a) (b)

Figure 9.5: Polar plots of two stability metrics (a) linear Nyquist and (b) even-mode loop gain with frequency sweeps from 0.1 to 120 GHz. The Nyquist plot contains 12 traces for both gate and drain reflections on each stage. The unstable regions are marked in red X's and the phase margin for even-mode loop gain is greater than 40°.

The dc bias connections to this amplifier are of significant importance to the design. In the previous work presented in Chapters 5-8, the MMIC PAs contain shunt capacitor ladders on-chip

and off-chip. Essentially, this is a series of low pass networks, where the first on-chip shunt capacitor hopefully manages to short any RF below the self-resonance of the structure. This functionality decouples the power supplies from the RF path. A significant problem with these networks is that in the operation band they can siphon energy from the main RF path increasing network loss. In [131], dual radial stubs for broadband band-stop in W-band are placed before a capacitor ladder. The radial stubs decouple the networks well; however, two downsides may be present in widespread usage of these networks. First is the form factor of the stubs. For a scaled dual radial stub at W-band, the area is roughly $400 \times 400\,\mu\text{m}^2$ without extra capacitor networks or bond pads. In power-combined power amplifiers, this size effectively reduces the amount of active channels a single die can have. Second, the networks are radial stubs which have potential to radiate. With these elements, there is increased potential for coupling between biasing paths and into cavity-modes (if packaged).

This design uses low-pass coupled line filters, seen in Fig. 9.6, to improve on these factors. The theory behind these coupled line filters is found in [194]. These networks have below 15 dB of return loss from 65 GHz up past 120 GHz with 50 Ω ports. Another benefit of these networks is that the input impedance at the RF path connection is over 100 Ω for all of W-band. The RF networks try to present wideband low impedance values (roughly 3 to 5 Ω) to the gates of the transistors and relatively low impedances $< 50\,\Omega$ on the drain which decreases as the transistors are scaled in size. The high impedance ports of these bias networks attach to the low impedance areas of the RF networks, effectively presenting a large mismatch in W-band thus decreasing W-band RF energy in the bias path. The 12 bias networks, seen in Fig. 9.2, are all tailored to reduce total form factor, however, all perform identical functions. Fig. 9.7 shows the magnitude in the current at two different frequencies: in the lower-band at 41 GHz and in the operation band at 102 GHz. The current magnitude at 102 GHz shows the low-pass functionality in the coupled line filter and stops at the small capacitor. At 41 GHz, current magnitude is near the via on the larger capacitor, showing shorting of the lower-band through that capacitor. Fig. 9.8 shows the magnitude of the current in the entire RF input network with the bias networks at 41 GHz. The network shows

highest current intensity in the first symmetric vias after port 1 with nearly no current at port 2.

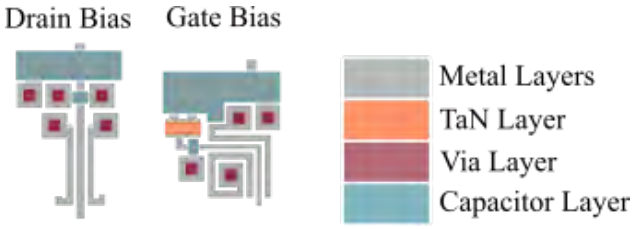

Figure 9.6: Layout diagram of the coupled line filter bias networks that perform low-pass functionality and high mismatch at the RF plane in order to reduce in-band RF losses from absorption in said dc bias networks.

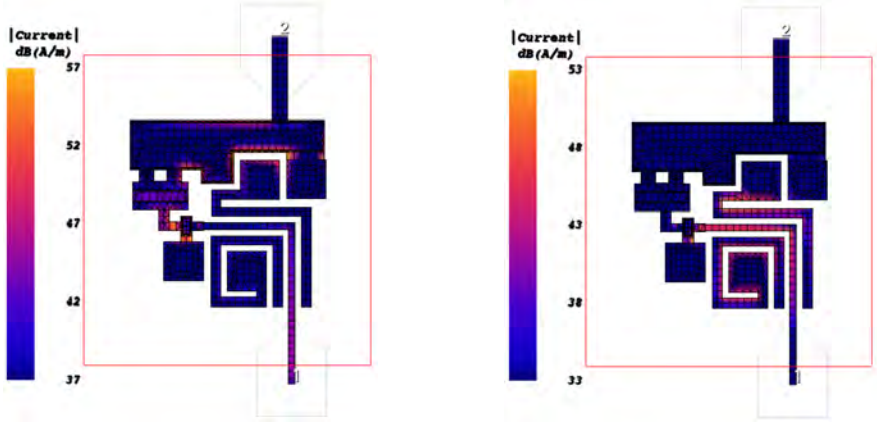

(a) (b)

Figure 9.7: Current magnitude in a gate bias network at (a) 41 GHz and (b) 102 GHz.

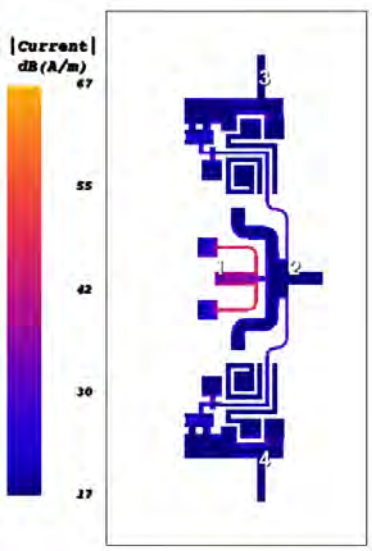

Figure 9.8: Current magnitude in the input RF network at 41 GHz.

Further out from the bias filter structures described, a bond pad network, as seen in Fig. 9.9 is created for the purpose of easy on-chip biasing. With the on-chip network, bond-wires can be chosen to reconfigure specific ties so that the each stage might be separately tested. This functionality reduces the number of probes need to bias the circuit.

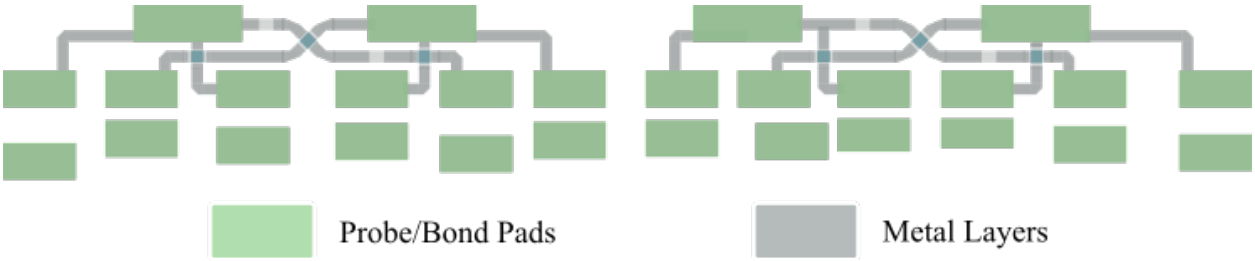

Figure 9.9: Layout diagram of the bond pad arrangement for on-chip bonding reconfigurability for ease of testing within the CU RF laboratory.

This 6-stage PA is to be taped-out on May 14th, 2021 and this design is DRC-clean and fully EM-simulated. Using this PA as a 'unit', a balanced topology similar to that in Chapter 6 is generated as seen in Fig. 9.10. The balanced topology inherently makes the design more reflection coefficient-invariant [85] and, as well, using two 6-stage PA as a units allows for a total periphery of

8050 μm. This layout also shows a Schottky-diode power detector on the isolated port of the output lange combiner. This power detector can detect load mismatches at the output port, effectively notifying of RF connection issues or significant coupling in antennas over scan (if in a phased array front-end). Without the specialty bond pad network, this circuit fits into a 5x3 mm die size (the same size die as the HRL circuits from Chapters 5 and 6).

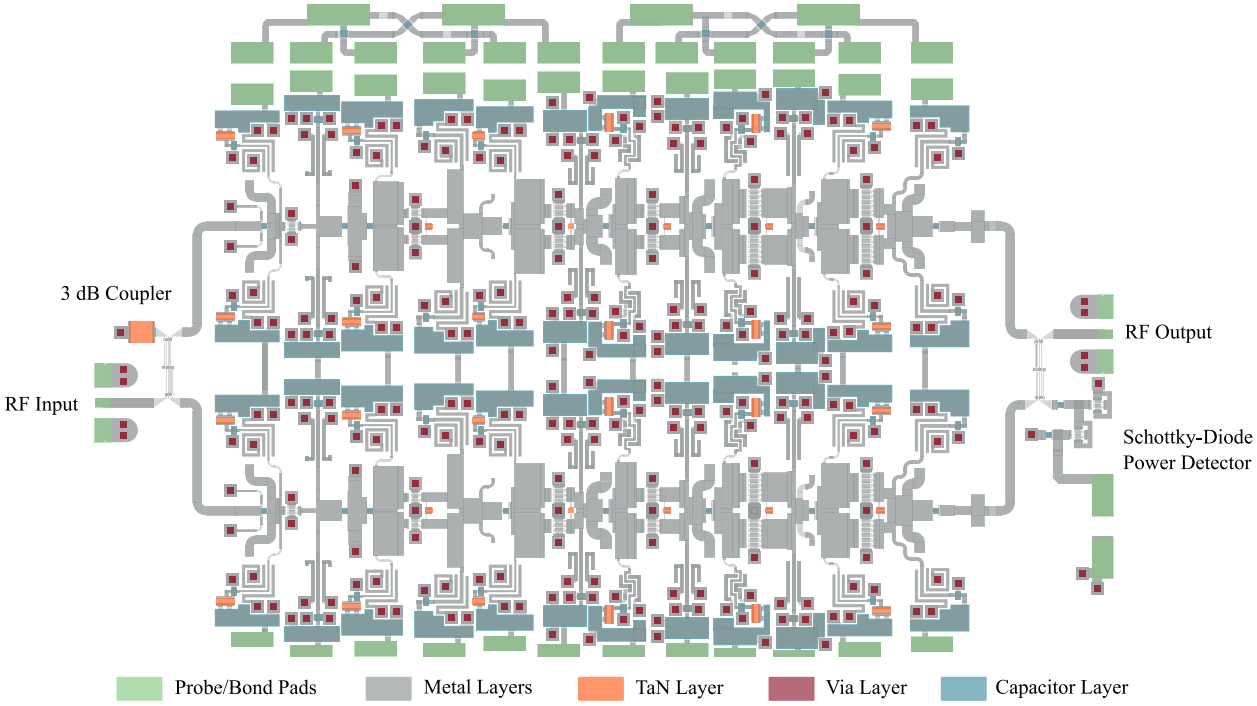

Figure 9.10: Layout of the 6-stage power amplifier in a balanced configuration. A Schottky-diode power detector is included on the isolated port of the output lange network.

Fig. 9.11 shows the relevant S-parameters ($|S_{11}|$,$|S_{22}|$, and $|S_{21}|$) and the P_{OUT}, PAE, and large-signal gain at P_{IN}=20 dBm. This PA has close to 2 W output power with above 4% PAE across the entire W-band, however, there is a slight 1 GHz band at 95 GHz that dips to 1.8 W. At around 75 GHz, this PA outputs above 5 W. If this device is to be made and works as simulated, this would be state-of-the-art for broadband power output at W-band.

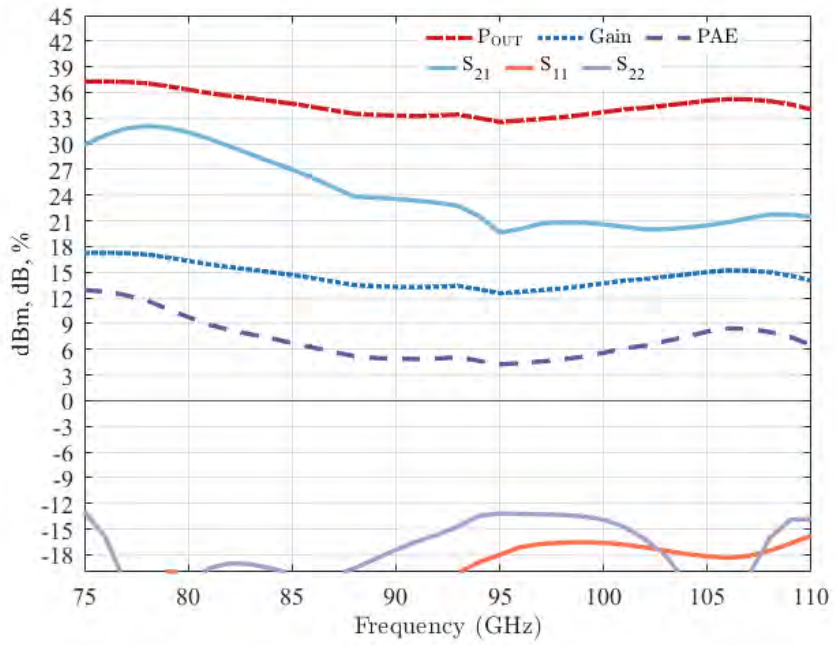

Figure 9.11: Small- and large-signal performance of the 6-stage PA over the W-band range with P_{IN}=20 dBm.

9.2.5 W-band Modulated Signal Bench

Another improvement to the work contained in this thesis is expanding the W-band large-signal characterization bench to include modulated signal testing and accurate power vector measurement. A diagram of the proposed setup is shown in Fig. 9.12. Three mixers are needed to achieve this capability: two high linearity mixers 25-36.6 GHz for upper and lower sideband mixing and one mixer with RF in W-band and local oscillator (LO) in V-band. The other components are available in the CU RF laboratory. The W-band upconversion chain is currently used and is shown in detail in Chapters 5 through 8. The V-band upconversion chain consists of a x4 multiplier. Multiple K-band amplifiers could be used here. A vector signal transceiver (VST) is capable of generating and analyzing multiple modulated signals up to 6 GHz with 1 GHz of instantaneous RF bandwidth. Multiple sources in the CU RF laboratory are capable of the LO needed for mixing.

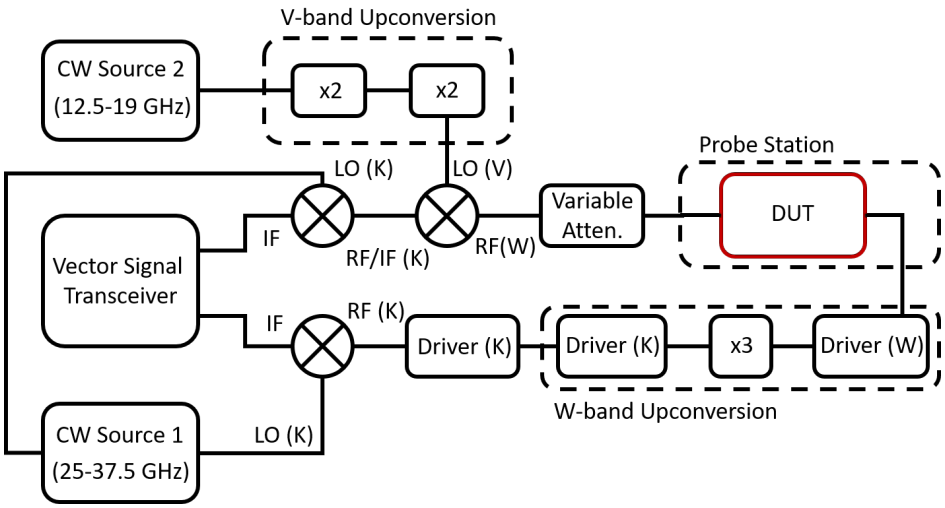

Figure 9.12: Diagram of a W-band large-signal vector characterization setup with VST from DC-4.5 GHz as a signal source. The diagram details mostly the upconversion paths and critical components to the function.

9.2.6 Three-network Cascaded Statistics for Waveguide Power Combining

There are numerous RF applications for using the general statistical analysis described in Chapters 7 and 8; one potential application of waveguide power-combing, shown in Fig. 9.13, expands upon two specific points by: increasing the amount of cascaded networks and including nonlinearity/power dependence. The goal of this analysis is to determine what the bounds of the power output are based solely on the RF variance from fabrication toleranaces and mounting/packaging of the waveguide, transitions, and MMIC PAs. The analysis could be performed either from simulated data-sets such as is the transistion from Chapter 8 or from a large number of measured large-signal and small-signal characterization of the components.

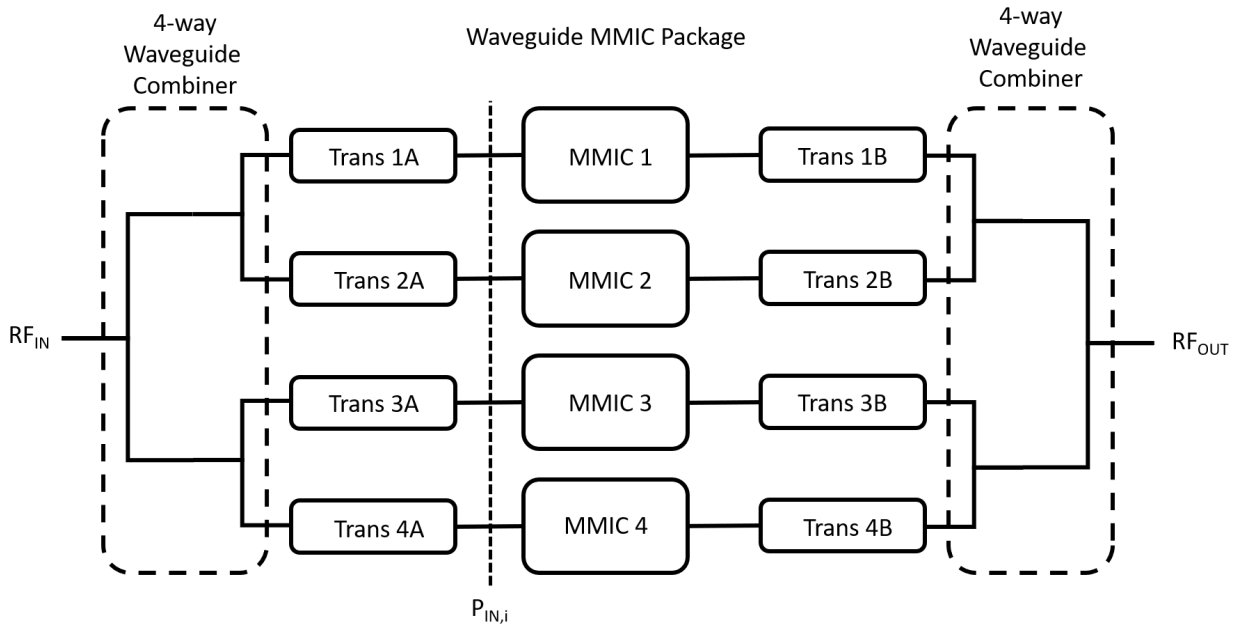

Figure 9.13: A labeled diagram of a waveguide-MMIC PA power combiner with four combining paths.

The algorithm for performing Monte Carlo analysis on the power combining affect is as follows given estimated densities of the data-sets:

(1) Simulate values for transistions 1A through 4B (output of small-signal S-parameters)

(2) Solve for the $P_{IN,i}$ at each MMIC based on the available gain through the A transistions

(3) Simulate a MMIC PA dependent on the $P_{IN,i}$ calculated (output of large-signal S-parameters)

(4) Solve for the cascaded S-parameters through the three networks

(5) Solve for the available gain from the power at RF_{IN}

(6) Calculate the combined power output through the output combiner

(7) Iterate the same procedure until number of P_{OUT} values are simulated

9.2.7 Millimeter-Wave Discrete Lens Arrays

At high millimeter-wave frequencies, phase shifters are extremely lossy [140]. A phase shifterless beam steering technique can be implemented with a 2D discrete lens array [195]. These arrays perform spatial discrete fourier transform such that beams pointing in different directions correspond to spatial distributed feed points on a focal surface. These have advantages over standard quasi-optical lenses because they are planar, can be manufactured using photolithography, and could include gain.

A series of lens arrays were designed in 100 μm thick fused silica with the goal of interfacing with cold atom system to perform angle-of-arrival estimation. A labeled diagram of the lenses can be seen in Fig. 9.14 and the complete set with desired frequency operation in Fig. 9.15. These lenses are in a process of fabrication on two 4-inch thin fused silica wafers. These arrays can be easily cascaded with the components presented in this thesis, namely waveguide feeds with integrated power amplifiers.

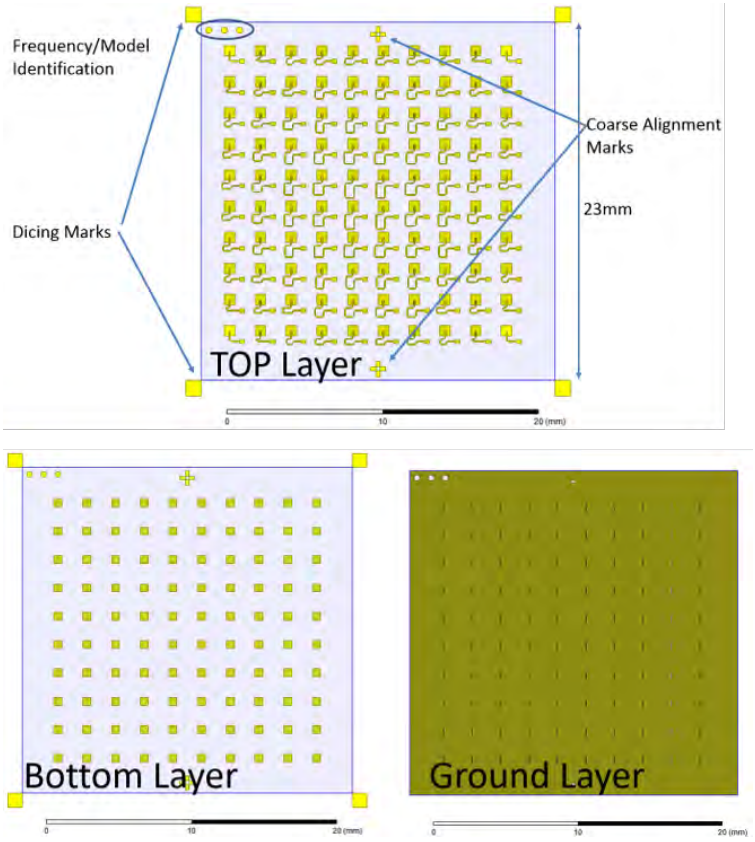

Figure 9.14: A labeled diagram of a single lens with a top layer of rectangular patch antennas, a coupled slot layer, and a bottom layer of square patches.

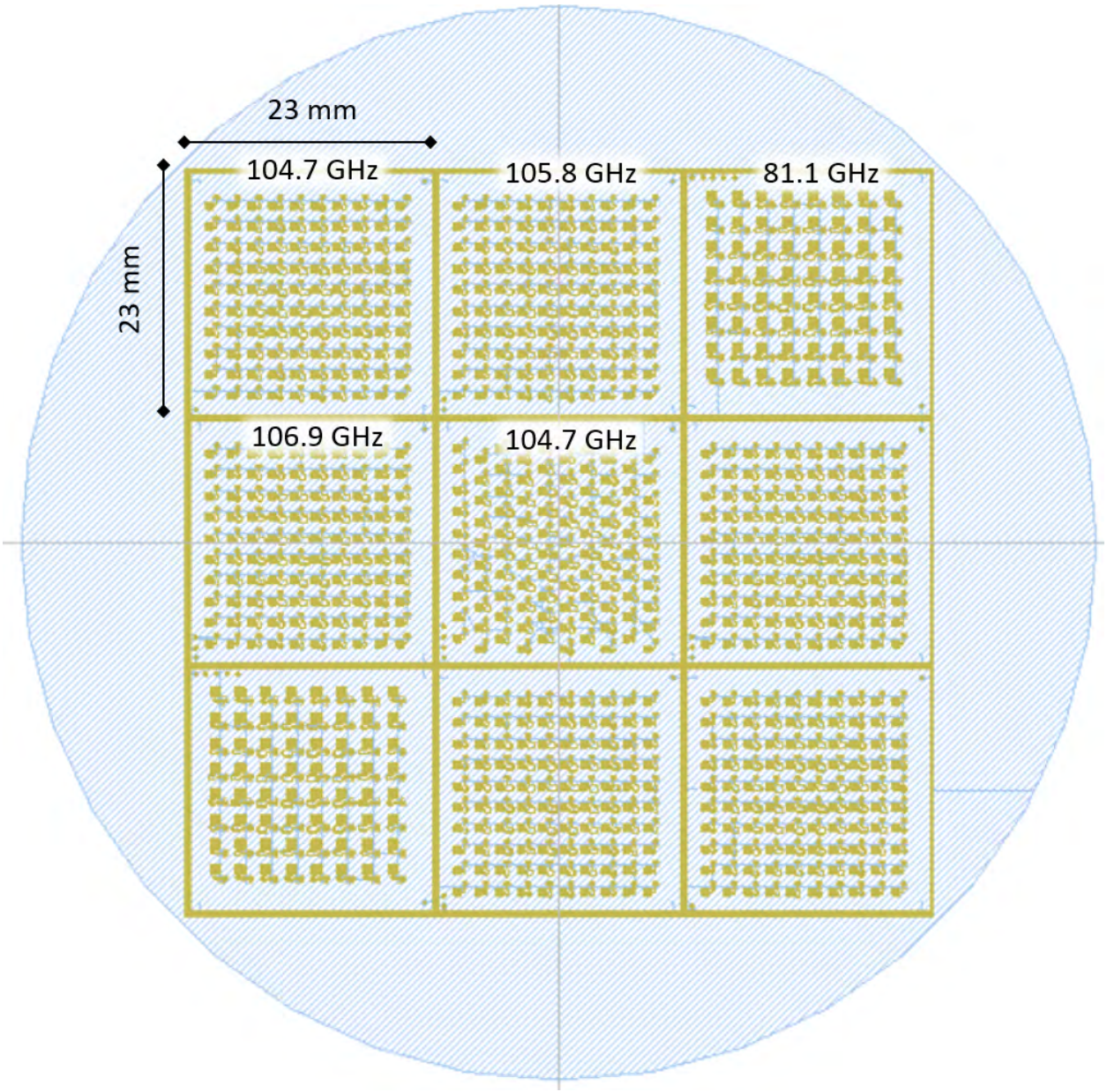

Figure 9.15: A layout of the wafer in fabrication currently with labels for the five repeated designs at specific operation frequencies.

9.3 Summary of Contributions

Contributions in areas of 3D printed millimeter-wave waveguides, MMIC PA design, and advanced process variation modeling are summarized as follows.

- In Chapter 2: A new type of power splitter that has a geometry well suited to 3D-printing is designed as a test structure that cannot be made using standard techniques. Both V- and W-band splitters are demonstrated experimentally in Chapter 3. These results are reported in [115].

- In Chapter 3: In metal 3D printing, is determined that there is a tradeoff between measured electrical conductivity and feature resolution, where maraging steel performs better with less surface roughness and higher printing repeatability at the cost of decreased conductivity. An analysis of the printed surfaces is performed and the 3-dimensional RMS and autocorrelation values of the unprocessed surface roughness is determined. It is also determined that the highly used surface roughness models such as the Hammerstad model fails to accurately capture loss from surface roughness as waveguide frequency increases. These results are reported in [90] and [115].

- In Chapters 5 and 6: A number of unique MMIC PA designs with large-scale power combining are demonstrated with operation across W-band in a 40-nm GaN-on-SiC process. The designs provide insight into useful methods for power-combining and a meaningful way to analyze combining efficiency. In particular, the power-combining efficiencies track simulated values and are above 85% in all cases and are as high as 95%. The design and measurement results are reported in [146]. New designs with even higher power levels with some innovative bias and matching structures are currently being submitted for fabrication.

- In Chapters 7 and 8: A new cascaded statistical analysis provides insight into effects of MMIC and passive structure fabrication variations on a 4x4 transmit antenna array performance. Probability density functions, both parametric (Gaussian) and non-parametric (kernel density estimation), are generated from measured MMIC data. The analysis shows that the kernel estimation best describes the data due to the unknown multitude of fabrication process variations. A Markov chain Monte-Carlo method is applied to cascaded statistics of multiple transmit chain components.The connection from the MMIC PAs to alumina microstrip-to-

waveguide transitions are analyzed with full-wave simulations in conjunction with the same statistical approach. The analysis is given on cases of small-signal MMIC gain cascaded with passive transitions with a simple Gaussian model, a bi-variate kernel density estimated model, and a model developed by using multi-variate S-parameters as complex random variables in a cascaded network. The waveguides feed a 16-element square horn array and the effect of cascaded statistics on EIRP is quantified. An extension to cascaded antenna fabrication tolerances is straightforward and follows the same methodology. Furthermore, the knowledge of process variations and their correlated statistics can give an insight into the ability to calibrate a phased array without pre-testing and choosing MMICs, as has been done in many millimeter-wave transmit arrays. The results from this work are published in [53].

Bibliography

[1] C. Riva, C. Capsoni, L. Luini, M. Luccini, R. Nebuloni, and A. Martellucci, "The challenge of using the w band in satellite communication," *International Journal of Satellite Communications and Networking*, vol. 32, no. 3, pp. 187–200, 2014. [Online]. Available: https://onlinelibrary.wiley.com/doi/abs/10.1002/sat.1050 1

[2] H. J. Liebe, T. Manabe, and G. A. Hufford, "Millimeter-wave attenuation and delay rates due to fog/cloud conditions," *IEEE Transactions on Antennas and Propagation*, vol. 37, no. 12, pp. 1617–1612, 1989. 1

[3] "United states frequency allocation chart." [Online]. Available: https://www.ntia.doc.gov/page/2011/united-states-frequency-allocation-chart x, 2

[4] S. Sun, T. S. Rappaport, M. Shafi, P. Tang, J. Zhang, and P. J. Smith, "Propagation models and performance evaluation for 5g millimeter-wave bands," *IEEE Transactions on Vehicular Technology*, vol. 67, no. 9, pp. 8422–8439, Sep. 2018. 2

[5] P. M. Asbeck, N. Rostomyan, M. Özen, B. Rabet, and J. A. Jayamon, "Power amplifiers for mm-wave 5g applications: Technology comparisons and cmos-soi demonstration circuits," *IEEE Transactions on Microwave Theory and Techniques*, vol. 67, no. 7, pp. 3099–3109, July 2019. 2

[6] "Ieee standard for information technology–telecommunications and information exchange between systems–local and metropolitan area networks–specific requirements-part 11: Wire-

less lan medium access control (mac) and physical layer (phy) specifications amendment 3: Enhancements for very high throughput in the 60 ghz band," *IEEE Std 802.11ad-2012 (Amendment to IEEE Std 802.11-2012, as amended by IEEE Std 802.11ae-2012 and IEEE Std 802.11aa-2012)*, pp. 1–628, 2012. 2

[7] F. C. Commision, *FCC 03-248*, 2003. 2

[8] K. Brown, A. Brown, T. Feenstra, D. Gritters, E. Ko, S. O'Connor, A. Pierce, A. Sanders, and M. Sotelo, "Ultra-compact high speed mmw transceiver using gan power amplifier technology," in *2015 IEEE MTT-S International Microwave Symposium*, May 2015, pp. 1–3. 3, 121

[9] F. Boes, J. Antes, T. Messinger, D. Meier, R. Henneberger, A. Tessmann, and I. Kallfass, "Multi-gigabit e-band wireless data transmission," in *2015 IEEE MTT-S International Microwave Symposium*, May 2015, pp. 1–4. 3

[10] C. Riva, C. Capsoni, L. Luini, M. Luccini, R. Nebuloni, and A. Martellucci, "The challenge of using the w band in satellite communication," *International Journal of Satellite Communications and Networking*, vol. 32, no. 3, pp. 187–200, 2014. [Online]. Available: https://onlinelibrary.wiley.com/doi/abs/10.1002/sat.1050 3, 11

[11] O. Kodheli, E. Lagunas, N. Maturo, S. K. Sharma, B. Shankar, J. F. M. Montoya, J. C. M. Duncan, D. Spano, S. Chatzinotas, S. Kisseleff, J. Querol, L. Lei, T. X. Vu, and G. Goussetis, "Satellite communications in the new space era: A survey and future challenges," *IEEE Communications Surveys Tutorials*, vol. 23, no. 1, pp. 70–109, 2021. 3

[12] X. Gu, A. Valdes-Garcia, A. Natarajan, B. Sadhu, D. Liu, and S. K. Reynolds, "W-band scalable phased arrays for imaging and communications," *IEEE Communications Magazine*, vol. 53, no. 4, pp. 196–204, 2015. 3

[13] D. Bleh, M. Rösch, M. Kuri, A. Dyck, A. Tessmann, A. Leuther, S. Wagner, B. Weismann-Thaden, H. . P. Stulz, M. Zink, M. Rießle, R. Sommer, J. Wilcke, M. Schlechtweg, B. Yang,

and O. Ambacher, "W-band time-domain multiplexing fmcw mimo radar for far-field 3-d imaging," *IEEE Transactions on Microwave Theory and Techniques*, vol. 65, no. 9, pp. 3474–3484, 2017. x, 3, 12, 13

[14] C. Rhoads and D. S. Goshi, "A scalable w-band imaging radar development platform," in *2018 IEEE Radar Conference (RadarConf18)*, 2018, pp. 0344–0348. 3

[15] D. M. Sheen, D. L. McMakin, and T. E. Hall, "Three-dimensional millimeter-wave imaging for concealed weapon detection," *IEEE Transactions on Microwave Theory and Techniques*, vol. 49, no. 9, pp. 1581–1592, 2001. 3

[16] N. H. Farhat and W. R. Guard, "Millimeter wave holographic imaging of concealed weapons," *Proceedings of the IEEE*, vol. 59, no. 9, pp. 1383–1384, 1971. 3

[17] H. Cheng, S. Li, H. Zheng, H. Jing, and H. Sun, "A w-band auto-focus holographic imaging system for security screening," *IEICE Electronics Express*, vol. 14, no. 11, pp. 20 170 347–20 170 347, 2017. 3

[18] I. Nasr, R. Jungmaier, A. Baheti, D. Noppeney, J. S. Bal, M. Wojnowski, E. Karagozler, H. Raja, J. Lien, I. Poupyrev, and S. Trotta, "A highly integrated 60 ghz 6-channel transceiver with antenna in package for smart sensing and short-range communications," *IEEE Journal of Solid-State Circuits*, vol. 51, no. 9, pp. 2066–2076, 2016. 3

[19] J. Lien, N. Gillian, M. E. Karagozler, P. Amihood, C. Schwesig, E. Olson, H. Raja, and I. Poupyrev, "Soli: Ubiquitous gesture sensing with millimeter wave radar," *ACM Trans. Graph.*, vol. 35, no. 4, Jul. 2016. [Online]. Available: https://doi.org/10.1145/2897824.2925953 3

[20] A. Arbabian, S. Callender, S. Kang, M. Rangwala, and A. M. Niknejad, "A 94 ghz mm-wave-to-baseband pulsed-radar transceiver with applications in imaging and gesture recognition," *IEEE Journal of Solid-State Circuits*, vol. 48, no. 4, pp. 1055–1071, 2013. 3

[21] D. Bleh, M. Rösch, M. Kuri, A. Dyck, A. Tessmann, A. Leuther, S. Wagner, and O. Ambacher, "A 100 ghz fmcw mimo radar system for 3d image reconstruction," in *2016 European Radar Conference (EuRAD)*, Oct 2016, pp. 37–40. 3

[22] S. Y. Jeon, M. H. Ka, S. Shin, M. Kim, S. Kim, S. Kim, J. Kim, A. Dewantari, J. Kim, and H. Chung, "W-band mimo fmcw radar system with simultaneous transmission of orthogonal waveforms for high-resolution imaging," *IEEE Transactions on Microwave Theory and Techniques*, vol. 66, no. 11, pp. 5051–5064, 2018. 3

[23] U. Alkus, A. B. Sahin, and H. Altan, "Stand-off through-the-wall w-band millimeter-wave imaging using compressive sensing," *IEEE Geoscience and Remote Sensing Letters*, vol. 15, no. 7, pp. 1025–1029, 2018. 3

[24] R. H. Geschke, O. Arpe, R. Brauns, and C. Krebs, "Enhanced hidden object detection with a circularly polarized w-band imaging radar system," in *2018 15th European Radar Conference (EuRAD)*, 2018, pp. 237–240. 3

[25] F. Nsengiyumva, C. Migliaccio, L. Brochier, J. Dauvignac, I. Aliferis, and C. Pichot, "New w -band scattering measurement system: Proof of concept and results for 2-d objects," *IEEE Transactions on Antennas and Propagation*, vol. 66, no. 12, pp. 7224–7236, 2018. 3

[26] M. Kishida, K. Ohguchi, and M. Shono, "79 ghz-band high-resolution millimeter-wave radar," *Fujitsu scientific and technical journal*, vol. 51, pp. 55–59, 10 2015. 3

[27] B. Ku, P. Schmalenberg, O. Inac, O. D. Gurbuz, J. S. Lee, K. Shiozaki, and G. M. Rebeiz, "A 77-81 ghz 16-element phased-array receiver with $\pm 50^\circ$ beam scanning for advanced automotive radars," *IEEE Transactions on Microwave Theory and Techniques*, vol. 62, no. 11, pp. 2823–2832, Nov 2014. 3

[28] P. Schmalenberg, J. S. Lee, and K. Shiozaki, "A sige-based 16-channel phased array radar system at w-band for automotive applications," in *2013 European Radar Conference*, Oct 2013, pp. 299–302. 3

[29] F. Engels, P. Heidenreich, A. M. Zoubir, F. K. Jondral, and M. Wintermantel, "Advances in automotive radar: A framework on computationally efficient high-resolution frequency estimation," *IEEE Signal Processing Magazine*, vol. 34, no. 2, pp. 36–46, 2017. 3

[30] B. P. Ginsburg, K. Subburaj, S. Samala, K. Ramasubramanian, J. Singh, S. Bhatara, S. Murali, D. Breen, M. Moallem, K. Dandu, S. Jalan, N. Nayak, R. Sachdev, I. Prathapan, K. Bhatia, T. Davis, E. Seok, H. Parthasarathy, R. Chatterjee, V. Srinivasan, V. Giannini, A. Kumar, R. Kulak, S. Ram, P. Gupta, Z. Parkar, S. Bhardwaj, Y. C. Rakesh, K. A. Rajagopal, A. Shrimali, and V. Rentala, "A multimode 76-to-81ghz automotive radar transceiver with autonomous monitoring," in *2018 IEEE International Solid - State Circuits Conference - (ISSCC)*, 2018, pp. 158–160. 3

[31] J. Hasch, E. Topak, R. Schnabel, T. Zwick, R. Weigel, and C. Waldschmidt, "Millimeter-wave technology for automotive radar sensors in the 77 ghz frequency band," *IEEE Transactions on Microwave Theory and Techniques*, vol. 60, no. 3, pp. 845–860, 2012. 3

[32] T. Lee, V. Skvortsov, M. Kim, S. Han, and M. Ka, "Application of w -band fmcw radar for road curvature estimation in poor visibility conditions," *IEEE Sensors Journal*, vol. 18, no. 13, pp. 5300–5312, 2018. 3

[33] Yexian Qin, P. Ingram, X. Wang, Tao Qin, H. Xin, and R. S. Witte, "Non-contact thermoacoustic imaging based on laser and microwave vibrometry," in *2014 IEEE International Ultrasonics Symposium*, 2014, pp. 1033–1036. 3

[34] A. Hati and C. W. Nelson, "w -band vibrometer for noncontact thermoacoustic imaging," *IEEE Transactions on Ultrasonics, Ferroelectrics, and Frequency Control*, vol. 66, no. 9, pp. 1536–1539, 2019. 3

[35] H. Kim and J. Jeong, "Non-contact measurement of human respiration and heartbeat using w-band doppler radar sensor," *Sensors*, vol. 20, no. 18, 2020. [Online]. Available: https://www.mdpi.com/1424-8220/20/18/5209 3

[36] K. Komoshvili, T. Becker, J. Levitan, A. Yahalom, A. Barbora, and S. Liberman-Aronov, "Morphological changes in h1299 human lung cancer cells following w-band millimeter-wave irradiation," *Applied Sciences*, vol. 10, no. 9, 2020. [Online]. Available: https://www.mdpi.com/2076-3417/10/9/3187 3

[37] R. Wang, C. Hu, X. Fu, and et al., "Micro-doppler measurement of insect wing-beat frequencies with w-band coherent radar," *Sci Rep*, 2017. 3

[38] D. Meier, C. Zech, B. Baumann, T. Link, M. Rösch, M. Schlechtweg, J. Kühn, and L. Reindl, "Classification of epoxy wedges in glass-fiber reinforced plastics using a millimeter-wave imaging system in w-band," in *2019 IEEE Topical Conference on Wireless Sensors and Sensor Networks (WiSNet)*, 2019, pp. 1–4. 4

[39] M. Božanić and S. Sinha, "Emerging transistor technologies capable of terahertz amplification: A way to re-engineer terahertz radar sensors," *Sensors*, vol. 19, no. 11, 2019. [Online]. Available: https://www.mdpi.com/1424-8220/19/11/2454 x, 4, 5

[40] K. Shinohara et. al, "Scaling of gan hemts and schottky diodes for submillimeter-wave mmic applications," *IEEE Transactions on Electron Devices*, vol. 60, no. 10, pp. 2982–2996, 2013. x, 4, 5, 7, 70

[41] R. York, Z. Popovic, and Z. Popović, *Active and Quasi-Optical Arrays for Solid-State Power Combining*, ser. A Wiley-Interscience publication. Wiley, 1997. [Online]. Available: https://books.google.com/books?id=_RtTAAAAMAAJ 6

[42] M. Pinto, "Millimeter-wave gan solid-state arrays," Ph.D. dissertation, 2019. x, 7, 61, 74, 101

[43] Y. Cao, V. Kumar, S. Chen, Y. Cui, S. Yoon, E. Beam, A. Xie, J. Jimenez, A. Ketterson, C. Lee, D. Linkhart, and A. Geiler, "Qorvo's emerging gan technologies for mmwave applications," in *2020 IEEE/MTT-S International Microwave Symposium (IMS)*, 2020, pp. 570–572. x, 7

[44] A. M. et.al, "70–105 ghz wideband gan power amplifiers," in *2012 7th European Microwave Integrated Circuit Conference*, 2012, pp. 199–202. 7, 69, 70

[45] M. Micovic, A. Kurdoghlian, H. P. Moyer, P. Hashimoto, M. Hu, M. Antcliffe, P. J. Willadsen, W. S. Wong, R. Bowen, I. Milosavljevic, Y. Yoon, A. Schmitz, M. Wetzel, C. McGuire, B. Hughes, and D. H. Chow, "Gan mmic pas for e-band (71 ghz - 95 ghz) radio," in *2008 IEEE Compound Semiconductor Integrated Circuits Symposium*, 2008, pp. 1–4. 7, 70

[46] Y. Tang, K. Shinohara, D. Regan, A. Corrion, D. Brown, J. Wong, A. Schmitz, H. Fung, S. Kim, and M. Micovic, "Ultrahigh-speed gan high-electron-mobility transistors with $f_T/f_{\max}$ of 454/444 ghz," *IEEE Electron Device Letters*, vol. 36, no. 6, pp. 549–551, 2015. 7, 70

[47] K. Shinohara, D. Regan, A. Corrion, D. Brown, Y. Tang, J. Wong, G. Candia, A. Schmitz, H. Fung, S. Kim, and M. Micovic, "Self-aligned-gate gan-hemts with heavily-doped n+-gan ohmic contacts to 2deg," in *2012 International Electron Devices Meeting*, 2012, pp. 27.2.1–27.2.4. 7, 70

[48] D. F. Brown, A. Kurdoghlian, R. Grabar, D. Santos, J. Magadia, H. Fung, J. Tai, I. Khalaf, and M. Micovic, "Broadband gan dhfet traveling wave amplifiers with up to 120 ghz bandwidth," in *2016 IEEE Compound Semiconductor Integrated Circuit Symposium (CSICS)*, 2016, pp. 1–4. 7, 70

[49] A. Margomenos, A. Kurdoghlian, M. Micovic, K. Shinohara, D. F. Brown, R. Bowen, I. Milosavljevic, R. Grabar, C. Butler, A. Schmitz, P. J. Willadsen, M. Madhav, and D. H. Chow, "70–105 ghz wideband gan power amplifiers," in *2012 7th European Microwave Integrated Circuit Conference*, 2012, pp. 199–202. 7, 70

[50] D. F. Brown, A. Williams, K. Shinohara, A. Kurdoghlian, I. Milosavljevic, P. Hashimoto, R. Grabar, S. Burnham, C. Butler, P. Willadsen, and M. Micovic, "W-band power perfor-

mance of algan/gan dhfets with regrown n+ gan ohmic contacts by mbe," in *2011 International Electron Devices Meeting*, 2011, pp. 19.3.1–19.3.4. 7, 70

[51] A. Margomenos, A. Kurdoghlian, M. Micovic, K. Shinohara, D. F. Brown, A. L. Corrion, H. P. Moyer, S. Burnham, D. C. Regan, R. M. Grabar, C. McGuire, M. D. Wetzel, R. Bowen, P. S. Chen, H. Y. Tai, A. Schmitz, H. Fung, A. Fung, and D. H. Chow, "Gan technology for e, w and g-band applications," in *2014 IEEE Compound Semiconductor Integrated Circuit Symposium (CSICS)*, 2014, pp. 1–4. 7, 70

[52] M. Micovic, A. Kurdoghlian, A. Margomenos, D. F. Brown, K. Shinohara, S. Burnham, I. Milosavljevic, R. Bowen, A. J. Williams, P. Hashimoto, R. Grabar, C. Butler, A. Schmitz, P. J. Willadsen, and D. H. Chow, "92–96 ghz gan power amplifiers," in *2012 IEEE/MTT-S International Microwave Symposium Digest*, 2012, pp. 1–3. 7, 70

[53] S. Verploegh, M. Pinto, L. Marzall, D. Martin, G. Lasser, and Z. Popović, "Analysis of process variations in w-band gan mmic pas using nonparametric statistics," *IEEE Transactions on Microwave Theory and Techniques*, pp. 1–1, 2021. 7, 68, 119, 140, 159

[54] J. E. Penn and K. Kingkeo, "V-band power amplifiers in 90 nm gallium nitride (gan)," CDCC Report No. AD1083245, CCDC Army Research Laboratory Aberdeen Proving Ground United States, 2019. [Online]. Available: https://apps.dtic.mil/sti/pdfs/AD1083245.pdf 7

[55] "(invited) critical recent advancement of GaN technology and MMICs for millimeter-wave applications," *ECS Meeting Abstracts*, 2017. [Online]. Available: https://doi.org/10.1149/ma2017-02/29/1227 7

[56] M. Kelley, "Ionosphere," in *Encyclopedia of Atmospheric Sciences*, J. R. Holton, Ed. Oxford: Academic Press, 2003, pp. 1022–1030. [Online]. Available: https://www.sciencedirect.com/science/article/pii/B0122270908001846 x, 9

[57] H. Liebe, T. Manabe, and G. Hufford, "Millimeter-wave attenuation and delay rates due to fog/cloud conditions," *IEEE Transactions on Antennas and Propagation*, vol. 37, no. 12, pp. 1617–1612, 1989. 9

[58] C. Townes and A. Schawlow, *Microwave Spectroscopy*, ser. Dover books on physics. Dover Publications, 2013. [Online]. Available: https://books.google.com/books?id=f33CAgAAQBAJ 9

[59] M. Marcus and B. Pattan, "Millimeter wave propagation: spectrum management implications," *IEEE Microwave Magazine*, vol. 6, no. 2, pp. 54–62, 2005. 9, 10

[60] S. J. Dudzinsky, *Atmospheric Effects on Terrestrial Millimeter-Wave Communications*. Santa Monica, CA: RAND Corporation, 1974. x, 10

[61] M. A. Samad, F. D. Diba, and D.-Y. Choi, "A survey of rain attenuation prediction models for terrestrial links—current research challenges and state-of-the-art," *Sensors*, vol. 21, no. 4, 2021. [Online]. Available: https://www.mdpi.com/1424-8220/21/4/1207 10

[62] P. Nagaraj, "Impact of atmospheric impairments on mmwave based outdoor communication," 2018. x, 11

[63] M. Van De Kamp, C. Riva, J. Tervonen, and E. Salonen, "Frequency dependence of amplitude scintillation," *IEEE Transactions on Antennas and Propagation*, vol. 47, no. 1, pp. 77–85, 1999. 11

[64] P. Garcia-del Pino, J. M. Riera, and A. Benarroch, "Tropospheric scintillation with concurrent rain attenuation at 50 ghz in madrid," *IEEE Transactions on Antennas and Propagation*, vol. 60, no. 3, pp. 1578–1583, 2012. 11

[65] A. M. Marziani, C. Riva, F. Consalvi, E. R. Restuccia, and F. S. Marzano, "Clear-air scintillation analysis of q-band alphasat link at spino d'adda using radiosounding data," in *2017 11th European Conference on Antennas and Propagation (EUCAP)*, 2017, pp. 15–19. 11

[66] B. Arbesser-Rastburg and A. Paraboni, "European research on ka-band slant path propagation," *Proceedings of the IEEE*, vol. 85, no. 6, pp. 843–852, 1997. 11

[67] K. Brown, A. Brown, T. Feenstra, D. Gritters, S. O'Connor, M. Sotelo, N. Kolias, K. C. Hwang, J. Kotce, and E. Robinson, "7kw gan w-band transmitter," in *2016 IEEE MTT-S International Microwave Symposium (IMS)*, 2016, pp. 1–3. x, 12, 13

[68] M. Rösch, A. Tessmann, A. Leuther, M. Kuri, S. Wagner, O. Ambacher, and H. Gulan, "Compact w-band receiver module on hybrid liquid crystal polymer board," in *2016 46th European Microwave Conference (EuMC)*, 2016, pp. 1517–1520. x, 12

[69] J. R. Montejo-Garai, I. O. Saracho-Pantoja, C. A. Leal-Sevillano, J. A. Ruiz-Cruz, and J. M. Rebollar, "Design of microwave waveguide devices for space and ground application implemented by additive manufacturing," in *2015 International Conference on Electromagnetics in Advanced Applications (ICEAA)*. IEEE, 2015, pp. 325–328. 16

[70] W. E. Frazier, "Metal additive manufacturing: a review," *Journal of Materials Engineering and performance*, vol. 23, no. 6, pp. 1917–1928, 2014. 19

[71] "How to design parts for metal 3d printing." [Online]. Available: https://www.3dhubs.com/knowledge-base/how-design-parts-metal-3d-printing/ xi, 20

[72] J. Thornton, B. Dalay, and D. Smith, "Additive manufacturing of waveguide for ku-band satellite communications antenna," in *2016 10th European Conference on Antennas and Propagation (EuCAP)*. IEEE, 2016, pp. 1–4. 20

[73] A. I. Dimitriadis, M. Favre, M. Billod, J.-P. Ansermet, and E. de Rijk, "Design and fabrication of a lightweight additive-manufactured ka-band horn antenna array," in *2016 10th European Conference on Antennas and Propagation (EuCAP)*. IEEE, 2016, pp. 1–4. 20

[74] M. D'Auria, W. J. Otter, J. Hazell, B. T. Gillatt, C. Long-Collins, N. M. Ridler, and S. Lucyszyn, "3-d printed metal-pipe rectangular waveguides," *IEEE Transactions on Com-*

ponents, Packaging and Manufacturing Technology, vol. 5, no. 9, pp. 1339–1349, 2015. 20, 41

[75] A. Tamayo-Domínguez, J.-M. Fernández-González, and M. Sierra-Pérez, "Groove gap waveguide in 3-d printed technology for low loss, weight, and cost distribution networks," *IEEE Transactions on Microwave Theory and Techniques*, vol. 65, no. 11, pp. 4138–4147, 2017. 20

[76] Y. Arbaoui, V. Laur, A. Maalouf, P. Queffelec, D. Passerieux, A. Delias, and P. Blondy, "Full 3-d printed microwave termination: A simple and low-cost solution," *IEEE Transactions on Microwave Theory and Techniques*, vol. 64, no. 1, pp. 271–278, 2015. 20

[77] X. Shang, P. Penchev, C. Guo, M. J. Lancaster, S. Dimov, Y. Dong, M. Favre, M. Billod, and E. De Rijk, "w-band waveguide filters fabricated by laser micromachining and 3-d printing," *IEEE Transactions on Microwave Theory and Techniques*, vol. 64, no. 8, pp. 2572–2580, 2016. 21

[78] B. Zhang and H. Zirath, "3d printed iris bandpass filters for millimetre-wave applications," *Electronics Letters*, vol. 51, no. 22, pp. 1791–1793, 2015. 21

[79] ——, "Metallic 3-d printed rectangular waveguides for millimeter-wave applications," *IEEE Transactions on Components, Packaging and Manufacturing Technology*, vol. 6, no. 5, pp. 796–804, 2016. 21

[80] J. Shen, M. W. Aiken, M. Abbasi, D. P. Parekh, X. Zhao, M. D. Dickey, and D. S. Ricketts, "Rapid prototyping of low loss 3d printed waveguides for millimeter-wave applications," in *2017 IEEE MTT-S International Microwave Symposium (IMS)*. IEEE, 2017, pp. 41–44. 21

[81] W. Otter, N. Ridler, H. Yasukochi, K. Soeda, K. Konishi, J. Yumoto, M. Kuwata-Gonokami, and S. Lucyszyn, "3d printed 1.1 thz waveguides," *Electronics Letters*, vol. 53, no. 7, pp. 471–473, 2017. 21

[82] O. A. Peverini, M. Lumia, F. Calignano, G. Addamo, M. Lorusso, E. P. Ambrosio, D. Manfredi, and G. Virone, "Selective laser melting manufacturing of microwave waveguide devices," *Proceedings of the IEEE*, vol. 105, no. 4, pp. 620–631, 2017. 21

[83] R. Collin, *Field Theory of Guided Waves*, ser. IEEE Press Series on Electromagnetic Wave Theory. Wiley, 1990. [Online]. Available: https://books.google.com/books?id=RQHpDwAAQBAJ 21, 22

[84] R. Harrington, *Time-Harmonic Electromagnetic Fields*, ser. IEEE Press Series on Electromagnetic Wave Theory. Wiley, 2001. [Online]. Available: https://books.google.com/books?id=4-6kNAEACAAJ 21, 22, 23

[85] D. Pozar, *Microwave Engineering, 4th Edition*. Wiley, 2011. [Online]. Available: https://books.google.com/books?id=JegbAAAAQBAJ 23, 150

[86] F. Benson, "Waveguide attenuation and its correlation with surface roughness," *Proceedings of the IEE - Part III: Radio and Communication Engineering*, vol. 100, pp. 85–90(5), March 1953. [Online]. Available: https://digital-library.theiet.org/content/journals/10.1049/pi-3.1953.0017 23

[87] J. W. Strutt, *The Theory of Sound*, ser. Cambridge Library Collection - Physical Sciences. Cambridge University Press, 2011, vol. 1. 23, 25

[88] J. Morgan, Samuel P., "Effect of Surface Roughness on Eddy Current Losses at Microwave Frequencies," *Journal of Applied Physics*, vol. 20, no. 4, pp. 352–362, Apr. 1949. 23

[89] E. Hammerstad and F. Bekkadal, *Microstrip Handbook*, ser. ELAB report. Norwegian Institute of Technology, 1975. [Online]. Available: https://books.google.com/books?id=igw6PQAACAAJ 24, 52

[90] S. Verploegh, M. Coffey, E. Grossman, and Z. Popović, "Properties of 50–110-ghz waveguide components fabricated by metal additive manufacturing," *IEEE Transactions on Microwave*

Theory and Techniques, vol. 65, no. 12, pp. 5144–5153, 2017. xii, xiii, 24, 26, 29, 31, 34, 42, 43, 55, 142, 143, 158

[91] C. L. Holloway and E. F. Kuester, "Impedance-type boundary conditions for a periodic interface between a dielectric and a highly conducting medium," *IEEE Transactions on Antennas and Propagation*, vol. 48, no. 10, pp. 1660–1672, 2000. 24

[92] ——, "Power loss associated with conducting and superconducting rough interfaces," *IEEE Transactions on Microwave Theory and Techniques*, vol. 48, no. 10, pp. 1601–1610, 2000. 24

[93] Z. Wu and L. E. Davis, "Surface roughness effect on surface impedance of superconductors," *Journal of Applied Physics*, vol. 76, no. 6, pp. 3669–3672, 1994. [Online]. Available: https://doi.org/10.1063/1.357430 24

[94] A. Matsushima and K. Nakata, "Power loss and local surface impedance associated with conducting rough interfaces," *Electronics and Communications in Japan (Part II: Electronics)*, vol. 89, no. 1, pp. 1–10, 2006. [Online]. Available: https://onlinelibrary.wiley.com/doi/abs/10.1002/ecjb.20218 24

[95] M. V. Lukic and D. S. Filipovic, "Modeling of 3-d surface roughness effects with application to μ-coaxial lines," *IEEE Transactions on Microwave Theory and Techniques*, vol. 55, no. 3, pp. 518–525, 2007. xi, 24, 25

[96] S. Hall, S. G. Pytel, P. G. Huray, D. Hua, A. Moonshiram, G. A. Brist, and E. Sijercic, "Multigigahertz causal transmission line modeling methodology using a 3-d hemispherical surface roughness approach," *IEEE Transactions on Microwave Theory and Techniques*, vol. 55, no. 12, pp. 2614–2624, 2007. 24

[97] M. Yi, S. Li, H. Yu, W. Khan, C. Ulusoy, A. Vera-Lopez, J. Papapolymerou, and M. Swaminathan, "Surface roughness modeling of substrate integrated waveguide in d-band," *IEEE Transactions on Microwave Theory and Techniques*, vol. 64, no. 4, pp. 1209–1216, 2016. 24

[98] A. Sanderson, "Effect of surface roughness on propagation of the tem mode," ser. Advances in Microwaves, L. YOUNG, Ed. Elsevier, 1971, vol. 7, pp. 1 – 57. [Online]. Available: http://www.sciencedirect.com/science/article/pii/B9780120279074500073 25

[99] S. O. Rice, "Reflection of electromagnetic waves from slightly rough surfaces," *Communications on Pure and Applied Mathematics*, vol. 4, no. 2-3, pp. 351–378, 1951. [Online]. Available: https://onlinelibrary.wiley.com/doi/abs/10.1002/cpa.3160040206 25

[100] U. Fano, "The theory of anomalous diffraction gratings and of quasi-stationary waves on metallic surfaces (sommerfeld's waves)," *J. Opt. Soc. Am.*, vol. 31, no. 3, pp. 213–222, Mar 1941. [Online]. Available: http://www.osapublishing.org/abstract.cfm?URI=josa-31-3-213 25

[101] L. Proekt and A. C. Cangellaris, "Investigation of the impact of conductor surface roughness on interconnect frequency-dependent ohmic loss," in *53rd Electronic Components and Technology Conference, 2003. Proceedings.*, 2003, pp. 1004–1010. 25

[102] J. Wait, "Guiding of electromagnetic waves by uniformly rough surfaces : Part i," *IRE Transactions on Antennas and Propagation*, vol. 7, no. 5, pp. 154–162, 1959. 25

[103] M. A. Biot, "Some new aspects of the reflection of electromagnetic waves on a rough surface," *Journal of Applied Physics*, vol. 28, no. 12, pp. 1455–1463, 1957. [Online]. Available: https://doi.org/10.1063/1.1722676 25

[104] Leung Tsang, Xiaoxiong Gu, and H. Braunisch, "Effects of random rough surface on absorption by conductors at microwave frequencies," *IEEE Microwave and Wireless Components Letters*, vol. 16, no. 4, pp. 221–223, 2006. 25, 143

[105] X. Gu, L. Tsang, and H. Braunisch, "Modeling effects of random rough interface on power absorption between dielectric and conductive medium in 3-d problem," *IEEE Transactions on Microwave Theory and Techniques*, vol. 55, no. 3, pp. 511–517, 2007. 25, 143

[106] ——, "Estimation of roughness-induced power absorption from measured surface profile data," *IEEE Microwave and Wireless Components Letters*, vol. 17, no. 7, pp. 486–488, 2007. 25, 143

[107] R. Ding, L. Tsang, and H. Braunisch, "Wave propagation in a randomly rough parallel-plate waveguide," *IEEE Transactions on Microwave Theory and Techniques*, vol. 57, no. 5, pp. 1216–1223, 2009. 25, 143

[108] R. Ding, L. Tsang, H. Braunisch, and W. Chang, "Wave propagation in parallel plate metallic waveguide with finite conductivity and three dimensional roughness," *IEEE Transactions on Antennas and Propagation*, vol. 60, no. 12, pp. 5867–5880, 2012. xi, 25, 26, 143

[109] R. Mansour and J. Dude, "Analysis of microstrip t-junction and its application to the design of transfer switches," in *1992 IEEE MTT-S Microwave Symposium Digest*. IEEE, 1992, pp. 889–892. 29

[110] L. W. Epp, D. J. Hoppe, A. R. Khan, and S. L. Stride, "A high-power *ka*-band (31–36 ghz) solid-state amplifier based on low-loss corporate waveguide combining," *IEEE Transactions on Microwave Theory and Techniques*, vol. 56, no. 8, pp. 1899–1908, 2008. 29

[111] F. Takeda, Y. Isoda *et al.*, "Waveguide power divider using metallic septum with resistive coupling slot," in *1982 IEEE MTT-S International Microwave Symposium Digest*. IEEE, 1982, pp. 527–528. 29

[112] P. Uliasz, T. Knych, M. Piwowarska, and J. Wiecheć, "The influence of heat treatment parameters on the electrical conductivity of alsi7mg and alsi10mg aluminum cast alloys," in *ICAA13 Pittsburgh*. Springer, 2012, pp. 129–135. 33

[113] D. L. Ellis, D. J. Keller, and M. Nathal, "Thermophysical properties of grcop-84," *NASA/CR*, vol. 210055, 2000. 33

[114] Midwest composite. Accessed: 2018-06-30. [Online]. Available: https://www.midwestcomposite.com 33

[115] S. Verploegh and Z. Popović, "V- and w-band two-way waveguide splitters fabricated by metal additive manufacturing," in *2018 IEEE MTT-S Latin America Microwave Conference (LAMC 2018)*, 2018, pp. 1–4. 34, 55, 158

[116] X. He, J. Norris, P. Fuerschbach, and T. DebRoy, "Liquid metal expulsion during laser spot welding of 304 stainless steel," *Journal of Physics D: Applied Physics*, vol. 39, no. 3, p. 525, 2006. 37

[117] C. A. Basca, M. Talos, and R. Brad, "Randomized hough transform for ellipse detection with result clustering," in *EUROCON 2005-The International Conference on" Computer as a Tool"*, vol. 2. IEEE, 2005, pp. 1397–1400. 43

[118] Y. Xie and Q. Ji, "A new efficient ellipse detection method," in *Object recognition supported by user interaction for service robots*, vol. 2. IEEE, 2002, pp. 957–960. 43

[119] P. Hanzl, M. Zetek, T. Bakša, and T. Kroupa, "The influence of processing parameters on the mechanical properties of slm parts," *Procedia Engineering*, vol. 100, pp. 1405–1413, 2015. 47

[120] B. Zhang, Z. Zhan, Y. Cao, H. Gulan, P. Linner, J. Sun, T. Zwick, and H. Zirath, "Metallic 3-d printed antennas for millimeter-and submillimeter wave applications," *IEEE transactions on terahertz science and technology*, vol. 6, no. 4, pp. 592–600, 2016. 48

[121] A. Townsend, N. Senin, L. Blunt, R. Leach, and J. Taylor, "Surface texture metrology for metal additive manufacturing: a review," *Precision Engineering*, vol. 46, pp. 34–47, 2016. 48

[122] E. N. Grossman, M. Gould, and N. P. Mujica-Schwann, "Robust evaluation of statistical surface topography parameters using focus-variation microscopy," *Surface Topography:*

Metrology and Properties, vol. 4, no. 3, p. 035003, sep 2016. [Online]. Available: https://doi.org/10.1088/2051-672x/4/3/035003 48

[123] E. S. Li, G. Tong, and D. C. Niu, "Full w -band waveguide-to-microstrip transition with new e-plane probe," *IEEE Microwave and Wireless Components Letters*, vol. 23, no. 1, pp. 4–6, Jan 2013. 57, 63

[124] J. Doo, W. Park, W. Choe, and J. Jeong, "Design of broadband w-band waveguide package and application to low noise amplifier module," *Electronics*, vol. 8, no. 5, 2019. 57

[125] A. U. Zaman, V. Vassilev, P. Kildal, and H. Zirath, "Millimeter wave e-plane transition from waveguide to microstrip line with large substrate size related to mmic integration," *IEEE Microwave and Wireless Components Letters*, vol. 26, no. 7, pp. 481–483, July 2016. 57

[126] C. Wu, Y. Zhang, Y. Xu, B. Yan, and R. Xu, "Millimeter-wave waveguide-to-microstrip transition with a built-in dc/if return path," *IEEE Transactions on Microwave Theory and Techniques*, vol. 69, no. 2, pp. 1295–1304, 2021. xiv, 57, 58

[127] Y.-C. Shih, T.-N. Ton, and L. Bui, "Waveguide-to-microstrip transitions for millimeter-wave applications," in *1988., IEEE MTT-S International Microwave Symposium Digest*, 1988, pp. 473–475 vol.1. 57

[128] F. Villegas, D. Stones, and H. Hung, "A novel waveguide-to-microstrip transition for millimeter-wave module applications," *IEEE Transactions on Microwave Theory and Techniques*, vol. 47, no. 1, pp. 48–55, 1999. xiv, 57, 58

[129] J. M. Pérez-Escudero, A. E. Torres-García, R. Gonzalo, and I. Ederra, "A simplified design inline microstrip-to-waveguide transition," *Electronics*, vol. 7, no. 10, 2018. [Online]. Available: https://www.mdpi.com/2079-9292/7/10/215 xiv, 57, 58

[130] W. Wang, F. Guo, T. Chen, and K. Wang, "24.8 a w-band power amplifier with distributed common-source gan hemt and 4-way wilkinson-lange combiner achieving 6w output power and

18% pae at 95ghz," in *2020 IEEE International Solid- State Circuits Conference - (ISSCC)*, 2020, pp. 376–378. 67, 69

[131] M. Cwiklinski et. al, "Full w-band gan power amplifier mmics using a novel type of broadband radial stub," *IEEE Transactions on Microwave Theory and Techniques*, vol. 66, no. 12, pp. 5664–5675, 2018. 67, 69, 148

[132] J. Schellenberg, B. Kim, and T. Phan, "W-band, broadband 2w gan mmic," pp. 1–4, June 2013. 68, 101, 104

[133] M. Micovic et. al, "W-band gan mmic with 842 mw output power at 88 ghz," in *2010 IEEE MTT-S International Microwave Symposium*, 2010, pp. 237–239. 69

[134] A. Brown et. al, "W-band gan power amplifier mmics," in *2011 IEEE MTT-S International Microwave Symposium*, 2011, pp. 1–4. 69

[135] J. Schellenberg, B. Kim, and T. Phan, "W-band, broadband 2w gan mmic," in *2013 IEEE MTT-S International Microwave Symposium Digest (MTT)*, 2013, pp. 1–4. 69

[136] Y. Niida et. al, "3.6 w/mm high power density w-band inalgan/gan hemt mmic power amplifier," in *2016 IEEE Topical Conference on Power Amplifiers for Wireless and Radio Applications (PAWR)*, 2016, pp. 24–26. 69

[137] J. Schellenberg et. al, "37 w, 75–100 ghz gan power amplifier," in *2016 IEEE MTT-S International Microwave Symposium (IMS)*, 2016, pp. 1–4. 69

[138] E. Ture et. al, "First demonstration of w-band tri-gate gan-hemt power amplifier mmic with 30 dbm output power," in *2017 IEEE MTT-S International Microwave Symposium (IMS)*, 2017, pp. 35–37. 69

[139] W. Shaobing et. al, "W-band algan/gan mmic pa with 3.1w output power," in *2017 14th China International Forum on Solid State Lighting: International Forum on Wide Bandgap Semiconductors China (SSLChina: IFWS)*, 2017, pp. 219–223. 69

[140] A. Margomenos, A. Kurdoghlian, M. Micovic, K. Shinohara, H. Moyer, D. C. Regan, R. M. Grabar, C. McGuire, M. D. Wetzel, and D. H. Chow, "W-band gan receiver components utilizing highly scaled, next generation gan device technology," in *2014 IEEE Compound Semiconductor Integrated Circuit Symposium (CSICS)*, 2014, pp. 1–4. 70, 155

[141] A. Kurdoghlian, H. Moyer, H. Sharifi, D. F. Brown, R. Nagele, J. Tai, R. Bowen, M. Wetzel, R. Grabar, D. Santos, and M. Micovic, "First demonstration of broadband w-band and d-band gan mmics for next generation communication systems," in *2017 IEEE MTT-S International Microwave Symposium (IMS)*, 2017, pp. 1126–1128. 70

[142] F. Herrault, J. C. Wong, Y. Tang, H. Y. Tai, and I. Ramos, "Heterogeneously integrated rf circuits using highly scaled off-the-shelf gan hemt chiplets," *IEEE Microwave and Wireless Components Letters*, vol. 30, no. 11, pp. 1061–1064, 2020. 70

[143] J. Joh, J. A. del Alamo, and J. Jimenez, "A simple current collapse measurement technique for gan high-electron mobility transistors," *IEEE Electron Device Letters*, vol. 29, no. 7, pp. 665–667, 2008. 70, 85, 142

[144] C. Campbell, *Microwave Monolithic Power Amplifier Design.* American Cancer Society, 2013, pp. 0–00. 74, 102

[145] A. Suarez, "Check the stability: Stability analysis methods for microwave circuits," *IEEE Microwave Magazine*, vol. 16, no. 5, pp. 69–90, 2015. 74, 102

[146] S. Verploegh, T. Sonnenberg, M. Pinto, A. Babenko, and Z. Popović, "On-chip power combining architectures with 3-stage w-band gan mmic power amplifiers," *IEEE Transactions on Microwave Theory and Techniques*, pp. 1–1, submitted May 5, 2021. 86, 99, 158

[147] Q. Rudiger, *GaN electronics.* Springer, 2007. 110, 111

[148] H. Tsuchida, I. Kamata, T. Miyazawa, M. Ito, X. Zhang, and M. Nagano, "Recent advances in 4h-sic epitaxy for high-voltage power devices," *Materials Science in Semiconductor Process-*

ing, vol. 78, pp. 2 – 12, 2018, wide band gap semiconductors technology for next generation of energy efficient power electronics. 110

[149] P. Waltereit, W. Bronner, R. Quay, M. Dammann, R. Kiefer, S. Müller, M. Musser, J. Kühn, F. v. Raay, M. Seelmann, M. Mikulla, O. Ambacher, F. v. Rijs, T. Rödle, and K. Riepe, "Gan hemt and mmic development at fraunhofer iaf: performance and reliability," *physica status solidi (a)*, vol. 206, no. 6, pp. 1215–1220, 2009. 110, 111

[150] K. Shinohara, D. C. Regan, Y. Tang, A. L. Corrion, D. F. Brown, J. C. Wong, J. F. Robinson, H. H. Fung, A. Schmitz, T. C. Oh, S. J. Kim, P. S. Chen, R. G. Nagele, A. D. Margomenos, and M. Micovic, "Scaling of gan hemts and schottky diodes for submillimeter-wave mmic applications," *IEEE Transactions on Electron Devices*, vol. 60, no. 10, pp. 2982–2996, Oct 2013. 110, 111

[151] A. Ellison, H. Radamson, M. Tuominen, S. Milita, C. Hallin, A. Henry, O. Kordina, T. Tuomi, R. Yakimova, R. Madar, and E. Janzén, "Wafer warpage, crystal bending and interface properties of 4h-sic epi-wafers," *Diamond and Related Materials*, vol. 6, no. 10, pp. 1369 – 1373, 1997. 110

[152] Y. Ohno and M. Kuzuhara, "Application of gan-based heterojunction fets for advanced wireless communication," *IEEE Transactions on Electron Devices*, vol. 48, no. 3, pp. 517–523, March 2001. 110

[153] M. Treu, R. Rupp, P. Blaschitz, and J. Hilsenbeck, "Commercial sic device processing: Status and requirements with respect to sic based power devices," *Superlattices and Microstructures*, vol. 40, no. 4, pp. 380 – 387, 2006. 110

[154] T. Kimoto, "Material science and device physics in SiC technology for high-voltage power devices," *Japanese Journal of Applied Physics*, vol. 54, no. 4, p. 040103, mar 2015. 110

[155] H. Jacobson, J. Birch, R. Yakimova, M. Syväjärvi, J. Bergman, A. Ellison, T. Tuomi, and E. Janzén, "Dislocation evolution in 4h-sic epitaxial layers," *Journal of Applied Physics*, vol. 91, no. 10, pp. 6354–6360, 2002. 110

[156] T. Ohno, H. Yamaguchi, S. Kuroda, K. Kojima, T. Suzuki, and K. Arai, "Direct observation of dislocations propagated from 4h–sic substrate to epitaxial layer by x-ray topography," *Journal of Crystal Growth*, vol. 260, no. 1, pp. 209 – 216, 2004. 110, 111

[157] A. C. Lang, J. L. Hart, J. G. Wen, D. J. Miller, D. J. Meyer, and M. L. Taheri, "I2 basal stacking fault as a degradation mechanism in reverse gate-biased algan/gan hemts," *Applied Physics Letters*, vol. 109, no. 13, p. 133509, 2016. 110

[158] M. R. Duffy, G. Lasser, G. Nevett, M. Roberg, and Z. Popović, "A three-stage 18.5–24-ghz gan-on-sic 4 w 40% efficient mmic pa," *IEEE Journal of Solid-State Circuits*, vol. 54, no. 9, pp. 2402–2410, Sep. 2019. 111

[159] J. Ruze, "Antenna tolerance theory | a review," *Proceedings of the IEEE*, vol. 54, no. 4, pp. 633–640, April 1966. 112, 133

[160] J. Howard, "Statistical patterns of a general array," *IEEE Transactions on Antennas and Propagation*, vol. 15, no. 1, pp. 60–65, January 1967. 112

[161] A. J. van den Biggelaar, U. Johannsen, P. Mattheijssen, and A. B. Smolders, "Improved statistical model on the effect of random errors in the phase and amplitude of element excitations on the array radiation pattern," *IEEE Transactions on Antennas and Propagation*, vol. 66, no. 5, pp. 2309–2317, May 2018. 112

[162] J. E. Chacon and T. Duong, *Multivariate Kernel Smoothing and Its Applications.*, ser. Chapman & Hall/CRC Monographs on Statistics & Applied Probability. Chapman and Hall/CRC, 2018. 114, 116

[163] M. Rudemo, "Empirical choice of histograms and kernel density estimators," *Scandinavian Journal of Statistics*, vol. 9, no. 2, pp. 65–78, 1982. 116

[164] A. Bowman and A. Azzalini, *Applied Smoothing Techniques for Data Analysis: The Kernel Approach with S-Plus Illustrations*, ser. Oxford Statistical Science Series. OUP Oxford, 1997. 116

[165] P. Hall, J. Marron, and B. Park, "Smoothed cross-validation," *Probability Theory and Related Fields*, vol. 92, no. 1, pp. 1–20, Mar 1992. 116

[166] J. J. Sowers, D. J. Pritchard, A. E. White, W. Kong, O. S. A. Tang, D. R. Tanner, and K. Jablinskey, "A 36 w, v-band, solid state source," in *1999 IEEE MTT-S International Microwave Symposium Digest*, vol. 1, 1999, pp. 235–238. 121

[167] A. Agrawal and A. Jablon, "A calibration technique for active phased array antennas," in *IEEE International Symposium on Phased Array Systems and Technology, 2003.*, 2003, pp. 223–228. 121

[168] C. Fulton, J. Salazar, D. Zrnic, D. Mirkovic, I. Ivic, and D. Doviak, "Polarimetrie phased array calibration for large-scale multi-mission radar applications," in *2018 IEEE Radar Conference (RadarConf18)*, 2018, pp. 1272–1277. 121

[169] S. D. Silverstein, "Application of orthogonal codes to the calibration of active phased array antennas for communication satellites," *IEEE Transactions on Signal Processing*, vol. 45, no. 1, pp. 206–218, 1997. 121

[170] W. K. Hastings, "Monte carlo sampling methods using markov chains and their applications," *Biometrika*, vol. 57, no. 1, pp. 97–109, 1970. 124

[171] M. Sköld and G. O. Roberts, "Density estimation for the metropolis hastings algorithm," *Scandinavian Journal of Statistics*, vol. 30, no. 4, pp. 699–718, 2003. 127

[172] S. Geman and D. Geman, "Stochastic relaxation, gibbs distributions, and the bayesian restoration of images," *IEEE Transactions on Pattern Analysis and Machine Intelligence*, vol. PAMI-6, no. 6, pp. 721–741, Nov 1984. 127

[173] J. Besag, "Comments on "representations of knowledge in complex system" by u. grenander and mi miller," *J. Roy. Statist. Soc. Ser. B*, vol. 56, pp. 591–592, 1994. 127

[174] G. O. Roberts and R. L. Tweedie, "Exponential convergence of langevin distributions and their discrete approximations," *Bernoulli*, vol. 2, no. 4, pp. 341–363, 12 1996. 127

[175] G. Roberts and J. Rosenthal, "Optimal scaling of discrete approximations to langevin diffusions," *Journal of the Royal Statistical Society: Series B (Statistical Methodology)*, vol. 60, no. 1, pp. 255–268, 1998. 127

[176] J. S. Liu, F. Liang, and W. Wong, "The multiple-try method and local optimization in metropolis sampling," *Journal of the American Statistical Association*, vol. 95, no. 449, pp. 121–134, 2000. 127

[177] P. J. Green, "Reversible jump markov chain monte carlo computation and bayesian model determination," *Biometrika*, vol. 82, no. 4, pp. 711–732, 12 1995. 127

[178] S. Duane, A. Kennedy, B. Pendleton, and D. Roweth, "Hybrid monte carlo," *Physics Letters B*, vol. 195, no. 2, pp. 216–222, 1987. 127

[179] A. Gelman and D. Rubin, "Inference from iterative simulation using multiple sequences," *Statist. Sci.*, vol. 7, no. 4, pp. 457–472, 11 1992. 127

[180] S. P. Brooks and A. Gelman, "General methods for monitoring convergence of iterative simulations," *Journal of Computational and Graphical Statistics*, vol. 7, no. 4, pp. 434–455, 1998. 128

[181] J. Geweke, "Evaluating the accuracy of sampling-based approaches to the calculation of posterior moments," Federal Reserve Bank of Minneapolis, Staff Report 148, 1991. 129

[182] A. Raftery and S. Lewis, "Practical markov chain monte carlo: Comment: One long run with diagnostics: Implementation strategies for markov chain monte carlo," *Statist. Sci.*, vol. 7, no. 4, pp. 493–497, 11 1992. 129

[183] P. Heidelberger and P. Welch, "A spectral method for confidence interval generation and run length control in simulations," *Commun. ACM*, vol. 24, no. 4, pp. 233–245, Apr. 1981. 129

[184] B. Yu and P. Mykland, "Looking at markov samplers through cusum path plots: a simple diagnostic idea," *Statistics and Computing*, vol. 8, no. 3, pp. 275–286, Aug 1998. 129

[185] F. Gardiol, *Microstrip Circuits*, ser. Wiley Series in Microwave and Optical Engineering. Wiley, 1994. 132

[186] J. K. Hsiao, "Design of error tolerance of a phased array," *Electronics Letters*, vol. 21, no. 19, pp. 834–836, 1985. 133

[187] Jeongheum Lee, Yongbeum Lee, and Hyeongdong Kim, "Decision of error tolerance in array element by the monte carlo method," *IEEE Transactions on Antennas and Propagation*, vol. 53, no. 4, pp. 1325–1331, 2005. 134

[188] L. Poli, P. Rocca, N. Anselmi, and A. Massa, "Dealing with uncertainties on phase weighting of linear antenna arrays by means of interval-based tolerance analysis," *IEEE Transactions on Antennas and Propagation*, vol. 63, no. 7, pp. 3229–3234, 2015. 134

[189] N. Anselmi, L. Manica, P. Rocca, and A. Massa, "Tolerance analysis of antenna arrays through interval arithmetic," *IEEE Transactions on Antennas and Propagation*, vol. 61, no. 11, pp. 5496–5507, 2013. 134

[190] E. Lier, M. Zemlyansky, D. Purdy, and D. Farina, "Phased array calibration and characterization based on orthogonal coding: Theory and experimental validation," in *2010 IEEE International Symposium on Phased Array Systems and Technology*, 2010, pp. 271–278. 140

[191] Y. Yin, S. Zihir, T. Kanar, Q. Ma, H. Chung, L. Gao, and G. M. Rebeiz, "A 37–42-ghz 8 × 8 phased-array with 48–51-dbm eirp, 64–qam 30-gb/s data rates, and evm analysis versus channel rms errors," *IEEE Transactions on Microwave Theory and Techniques*, vol. 68, no. 11, pp. 4753–4764, 2020. 140

[192] S. Shahramian, M. J. Holyoak, A. Singh, and Y. Baeyens, "A fully integrated 384-element, 16-tile, w -band phased array with self-alignment and self-test," *IEEE Journal of Solid-State Circuits*, vol. 54, no. 9, pp. 2419–2434, 2019. 140

[193] "3d printer evaluation." [Online]. Available: https://github.com/kickstarter/kickstarter-autodesk-3d xxii, 143

[194] E. Jones, "Coupled-strip-transmission-line filters and directional couplers," *IRE Transactions on Microwave Theory and Techniques*, vol. 4, no. 2, pp. 75–81, 1956. 148

[195] D. Popovic, "Constrained lens arrays for communications systems with polarization and angle diversity," Ph.D. dissertation, 2002. 155